STUDIES OF BIO WASTE MATERIALS FROM SAGO HAMPAS AND OIL PALM
LEAVES FOR CELL IMAGING APPLICATIONS

SHORIYA ARUNI BINTI ABDUL MANAF

MASTER OF SCIENCE

UNIVERSITI MALAYSIA PAHANG

STUDIES OF BIO WASTE MATERIALS FROM SAGO HAMPAS AND OIL PALM
LEAVES FOR CELL IMAGING APPLICATIONS

SHORIYA ARUNI BINTI ABDUL MANAF

Thesis submitted in fulfillment of the requirements for the award of the degree of Master of
Science

Faculty of Industrial Sciences and Technology
UNIVERSITI MALAYSIA PAHANG

AUGUST 2015

SUPERVISOR'S DECLARATION

We hereby declare that we have checked this thesis and in our opinion, this thesis is adequate in terms of scope and the quality for the award of the degree of Master of Science.

Signature:

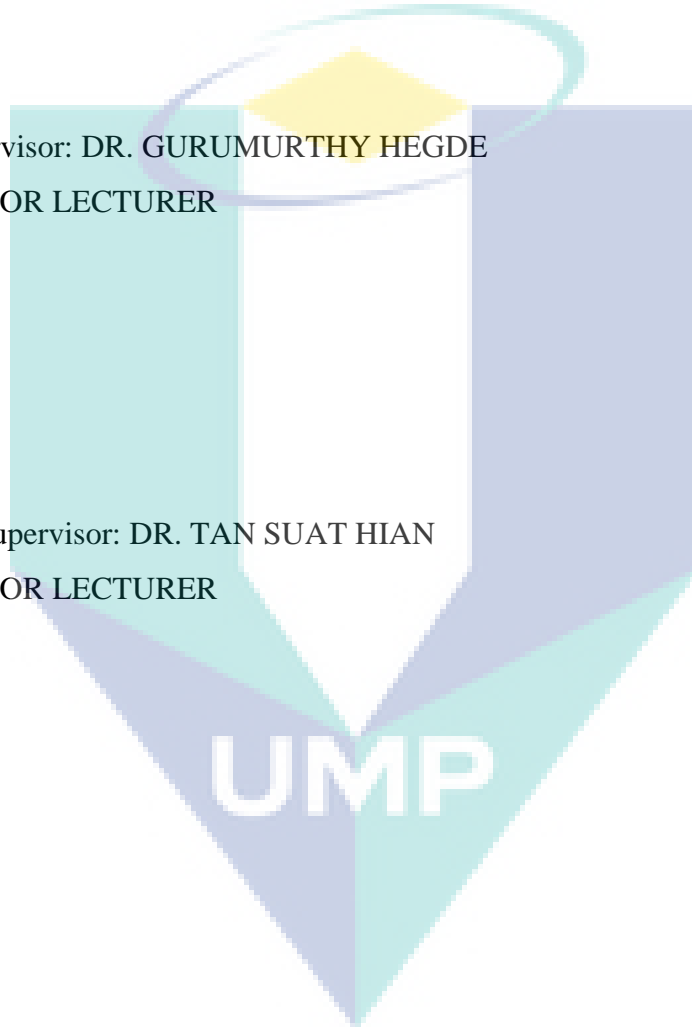Name of Supervisor: DR. GURUMURTHY HEGDE

Position: SENIOR LECTURER

Date:

Signature:

Name of Co-Supervisor: DR. TAN SUAT HIAN

Position: SENIOR LECTURER
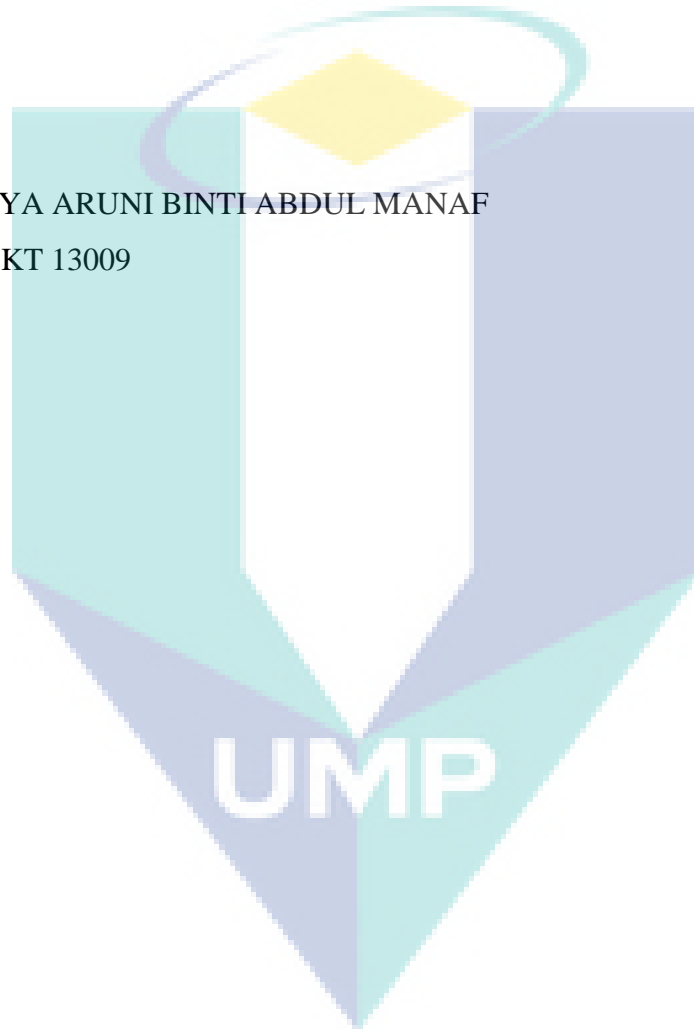
Date:

STUDENT'S DECLARATION

I hereby declare that the work in this thesis is my own except for quotations and summaries which have been duly acknowledged. The thesis has not been accepted for any degree and is not concurrently submitted for award of other degree.

Signature:

Name: SHORIYA ARUNI BINTI ABDUL MANAF

ID Number: MKT 13009

Date:

ACKNOWLEDGEMENTS

I am grateful and would like to express my sincere gratitude to my supervisor, Dr. Gurumurthy Hegde for his germinal ideas, invaluable guidance, continuous encouragement and constant support in making this research possible. He has always impressed me with his outstanding professional conduct and his strong conviction for science. I appreciate his consistent support from the first day I applied to graduate program to these concluding moments. I am truly grateful for his progressive vision about my training in science, his tolerance of my naïve mistakes and his commitment to my future career. I also would like to express very special thanks to my co supervisor Dr. Tan Suat Hian for her suggestion and cooperation throughout the study.

My sincere thanks to my group members especially Gan Siew Mei, Yuvaraj A.R., Mehdi Qasim for their help in conducting several experiments related to this project. Not to forget, my special thanks to post doctorate fellow, Anuj Kumar for his guidance and commitment to help me to conduct the experiment also teaches me to learn more about the subject. I also like to thank them for being good with me all the time and motivated me throughout my work.

My sincere thanks go to all my lab mates and staff members of Faculty of Industrial Sciences and Technology, UMP, who helped me in many ways and made my stay at UMP pleasant and unforgettable. Special thanks also to the lab assistant that helped and cooperated with me throughout the study.

I acknowledge my sincere indebtedness and gratitude to my parents and brothers for their love, dream and sacrifice throughout my life. I cannot find the appropriate words that could properly describe my appreciation for their devotion, support and faith in my ability to attain my goals. Special thanks should be given to my dear friends. I would like to acknowledge their comments and suggestions, which was crucial for the successful completion of this study.

ABSTRACT

Synthesizing of carbon nanospheres (CNSs) from bio waste is a good approach due to its availability, environmental friendly and low cost. On the other hand, utilization of bio waste to the high added value products attracts much attention where it can prevent the environmental problems due to its overload. Although there are many types of bio wastes available, very limited studies were attempted to use oil palm leaves (OPL) and sago hampas as the precursor for synthesizing carbon nanospheres. The CNSs were obtained by using a single step pyrolysis method in nitrogen atmosphere at different temperature in tube furnace without any catalysts support. For the OPL precursor, the pyrolysis temperatures are 500 °C, 600 °C and 700 °C and for sago hampas, its temperatures are 400 °C and 600 °C, which has been identified using TGA analysis. The key approach is the natural silica bodies found in the precursor that plays important template role in the formation of CNSs. In addition, the lignocellulosic content in the bio waste also plays the role as a carbon source for the CNSs synthesis. Different pyrolysis temperature gives different effect on the pyrolyzed materials. The obtained CNSs were characterized by TGA, XRD, Raman, FTIR, FESEM-EDX, TEM and Zeta potential. The optimum temperature for the CNSs obtained from OPL is 600 °C. At this temperature, CNSs exhibit small sizes of particle, which is ~20 nm with uniform distribution of spherical shape particles under FESEM analysis. In addition, TEM with a high magnification view shows the particle size of 30 nm. The carbon content of CNSs at 600 °C gives highest value, which is 87.90 % compared to the other pyrolysis temperature. On the other hand, the CNSs obtained from sago hampas show that the higher temperature gives better performance. The FESEM images show that the particle size is in the range of 60-70 nm whereas the TEM images exhibit the 50 nm of particle size with spherical shape observed. The carbon content at higher temperature gives 83.90 %, which is higher than the lower pyrolysis temperature. It shows that the different precursor gives different carbonizations effect depending on the pyrolysis temperature. The obtained CNSs were used for biotechnology applications which are cell imaging. The CNSs was tagged with fluorescent dye of Coumarin 6 (C-6). Few cell lines including UMR 106, A375, N2A and MDCK were used as biological model to observe CNSs ability as a nano carriers for drug delivery. The cellular uptake study observed under fluorescence microscope shows that the CNSs were efficiently taken up by the cell lines and cytotoxicity was determined by MTT assay method. From the results it shows that the CNSs can inhibit the cell proliferation of MDCK and N2A at low percentages whereas for A375 it can be clearly observed the apoptosis with dose dependent. This finding shows the alternative way to produce low cost and high value carbon nanospheres with spherical shape and porous structure by utilization of bio waste as a precursor. The CNSs can be applied in many other applications such as drug delivery, water purification and energy storage device.

ABSTRAK

Sintesis karbon nanosfera (CNSs) daripada sisa bio adalah pendekatan yang baik kerana ianya tersedia, mesra alam dan melibatkan kos yang rendah. Sebaliknya, penggunaan sisa bio untuk menghasilkan produk-produk bernilai tambah tinggi menarik perhatian ramai di mana ia boleh mencegah masalah-masalah alam sekitar akibat penghasilan sisa bio yang terlampau banyak. Terdapat banyak jenis bahan buangan bio, tetapi daun pokok kelapa sawit (OPL) dan hampas sagu dijadikan sebagai pelopor dalam kajian ini. CNSs yang diperolehi dengan menggunakan kaedah satu langkah ringkas pirolisis di dalam atmosfera nitrogen pada suhu yang berbeza dalam tiub relau tanpa menggunakan sokongan pemangkin. Bagi bahan utama OPL, pirolisis dijalankan pada suhu 500 °C, 600 °C dan 700 °C dan bagi hampas sagu, pirolisis dijalankan pada suhu 400 °C dan 600 °C. Pendekatan utama adalah silika semulajadi yang terdapat di dalam OPL yang memainkan peranan penting dalam pembentukan CNSs. Di samping itu, kandungan lignoselulosa dalam sisa bio juga memainkan peranan sebagai sumber karbon untuk mensintesis CNSs. Suhu pirolisis yang berbeza telah memberi kesan yang berbeza terhadap bahan-bahan yang digunakan. CNSs yang diperolehi telah dicirikan menggunakan peralatan TGA, XRD, Raman, FTIR, FESEM-EDX, TEM dan 'Zeta potential'. Suhu optimum untuk menghasilkan CNSs daripada OPL adalah pada 600 °C. Pada suhu ini, CNSs telah mempamerkan saiz zarah yang kecil iaitu ~ 20-nm dengan taburan seragam oleh zarah berbentuk sfera di bawah analisis FESEM. Di samping itu, TEM yang mempunyai magnifikasi yang tinggi menunjukkan saiz zarah ialah 30 nm. Kandungan karbon CNSs pada 600 °C memberikan nilai tertinggi iaitu 87.90 % berbanding suhu pirolisis yang lain. Selain daripada itu, CNSs yang diperolehi daripada sagu hampas menunjukkan bahawa suhu yang lebih tinggi memberikan prestasi yang lebih baik. Imej-imej daripada FESEM menunjukkan bahawa saiz zarah adalah dalam lingkungan 60-70 nm sementara imej daripada TEM menunjukkan saiz zarah ialah 50 nm yang berbentuk sfera dapat dilihat. Kandungan karbon pada bahan yang dihasilkan pada suhu tinggi memberi 83.90 % iaitu lebih tinggi daripada bahan yang diperoleh daripada suhu pirolisis yang lebih rendah. Ini menunjukkan bahawa bahan pelopor yang berbeza memberikan kesan karbonisasi yang berbeza bergantung kepada suhu pirolisis. CNSs yang diperolehi dapat digunakan untuk aplikasi bioteknologi iaitu pengimejan sel. Di dalam kajian untuk pengimejan sel, CNSs yang ditandakan dengan pewarna 'flourescence' iaitu 'Coumarin 6'(C-6). Beberapa sel termasuk UMR 106, A375, N2A dan MDCK telah digunakan untuk melihat keupayaan CNSs sebagai pembawa nano untuk penghantaran ubat. Kajian penyerapan selular yang diperhatikan di bawah mikroskop 'flourescence' telah menunjukkan bahawa CNSs telah cekap diserap oleh sel dan ujian sitotoksisiti ditentukan melalui ujuran MTT. Daripada data yang diperolehi, ia menunjukkan bahawa CNSs boleh menghalang proliferasi sel MDCK dan N2A pada peratus yang rendah manakala untuk A375 ianya boleh dilihat dengan jelas apoptosis yang berlaku dengan kebergantungan pada dos yang digunakan. Penemuan ini menunjukkan satu cara alternatif untuk menghasilkan CNSs yang bernilai tinggi pada kos yang rendah, yang mempunyai bentuk sfera dan struktur berliang dengan penggunaan sisa bio sebagai bahan asas. CNSs boleh digunakan dalam banyak aplikasi lain seperti penghantaran ubat, penulenan air, alat penyimpan tenaga.

TABLE OF CONTENTS

CHAPTER 4   **RESULTS AND DISCUSSION**

CHAPTER 5   **CONCLUSION**

1.   Publications

        (a) Included in this thesis

        (b) Not Included in this thesis

2.   Patents

3.   Awards and Medals

4.   Conference/s

APPENDICES

LIST OF TABLES

LIST OF FIGURES

LIST OF SYMBOLS

θ — Diffraction angle (degree)

°C — Degree Celcius

% — Percentage
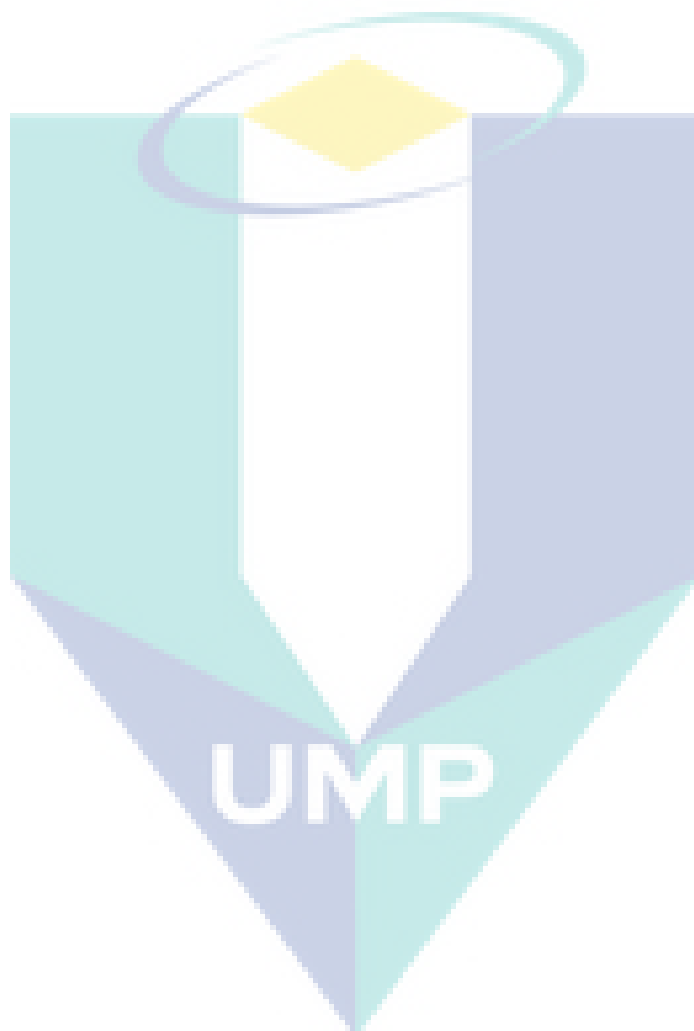
LIST OF ABBREVIATIONS

CNSs	Carbon nanospheres
C-6	Coumarin-6
OPL	Oil palm leaves
SH	Sago hampas
TGA	Thermogravimetric analysis
TEM	Transmission electron microscopy
FESEM	Field emission scanning electron microscopy
EDX	Energy dispersive X-ray
XRD	X-ray diffraction
FTIR	Fourier transforms infrared
BET	Brunauer, Emmett and Teller
EFB	Empty fruit bunch
CNS	Central nervous system
KBr	Potassium bromide
DMSO	Dimethyl sulfoxide
DMEM	Dulbecco's modified eagle medium
FBS	Fetal bovine serum
EDTA	Ethylenediaminetetraacetic acid
FFR	Fast electric field reversal
SFR	Slow field reversal

CHAPTER 1

INTRODUCTION

1.1   BACKGROUND STUDY

Today nanostructured carbon material draws great attraction among scientists and researchers from entire world as it can be used in wide spectrum of applications. Carbon structure nanomaterial such as carbon nanoparticles, carbon nanotubes, carbon nanofibers and carbon nanospheres are in high demand due to the flexible and unique properties where it can be applied in many fields.

Of all, carbon nanospheres (CNSs) are one of the nanomaterials that have high demand for the industrial applications due to their spherical shape and porous nature. CNSs give interesting morphologies and have potential to be used as nano-additives, super-capacitors, and energy storage and separation technology as well as in medical field (Im et al., 2014 and Mohammed et al., 2013). The production of CNSs using chemical vapor deposition (Poinern et al., 2012) and laser ablation has many limitations since it requires complicated procedures and contributes to high production cost. Besides, the frequently used petroleum based precursor gives negative environmental impact and thus it is better to have environmental friendly and natural carbon source precursor (Triphati et al., 2012). In short, there is a need to find out a simple method that is cost effective and does not affect the environment and at the same time, produce high quality nanomaterial.

On the other hand, oil palm industry is developing very well as it gives to the Malaysian economy by becoming the world major production of palm oil based products (Sukiran et al., 2011). As the industry develops, the production also increases and it produces enormous amount of waste annually (Hashim et al., 2011). The bio waste from oil palm industry especially the plantation waste such as oil palm trunks, fronds and leaves are normally burned, which creates pollution to the environment (Abdullah and Sulaiman, 2013). It is advisable to create waste to wealth approach in which instead of burning the bio waste, it can be utilized it to make valuable products as it can give benefits to human kind (Yuliansyah and Hirajima, 2012).

Besides that, sago palm that is easily available in Sarawak, Malaysia also produces bio waste from the sago starch processing industry (Pushpamalar et al., 2006). Annually, there are large amounts of waste produced from the sago starch industry, which creates the environmental problems where the waste from the industry flows into the nearby rivers and streams (Awg-Adeni et al., 2010 and Tan et al., 2014). This phenomenon increases the water pollution rates and also makes it worst (Kuroda et al., 2001) hence the usage of the bio waste from the industry should be optimized (Awg-Adeni et al., 2010).

The conversion of bio waste, particularly oil palm leaves and sago hampas into valuable products where it can be used as the precursor for carbon nanomaterial production is an attractive way to reduce the environmental pollution. This kind of precursor is low in cost, readily available, environmental friendly, free of catalyst and more importantly it is highly suitable for bulk production. These carbon nanomaterials are having promising application in biotechnology such as cell imaging.

Bio waste materials are subject of interest ever since waste materials started accumulating in the environment. South East Asia especially, where oil palm is the major crop, the waste produced by them is enormous and it cannot be neglected. So here, in this thesis a detail investigation of using bio waste oil palm leaves into valuable carbon nanoparticles were explained using several characterizations. Oil palm leaves have been

used as the precursor and several characterizations were done using TGA, FESEM-EDX, XRD and FTIR. These measurements play important roles in order to optimize the pyrolysis condition for the precursor to obtain carbon nanospheres.

1.2   PROBLEM STATEMENT

Oil palm is the well-known crops especially in Malaysia, which boost the country economic status through the production of palm oil based product. As the industry is growing rapidly, the production also increases and contributes to large amounts of bio waste annually. This large amount of bio waste creates environmental issues where it causes pollution such as air pollution due to the open burning of bio waste (Abdullah and Sulaiman, 2013). The burning of bio waste is the easiest method to decompose the oil palm waste from plantations but this method leads to environmental problems. Along with oil palm, there is another major crop named sago palm, which is the major supply for sago starch processing industry where it produces large amounts of waste that can contributes to environmental problems especially water pollution (Awg-Adeni et al., 2010). Hence, we should overcome these problems by utilizing the bio waste into valuable products.

It is a well-known fact that the production of carbon nanomaterials such as carbon nanotubes and carbon nanofibers require complicated procedures, therefore, it gives high production cost (Qian et al., 2014). Furthermore, the commonly used method involves the non-environmental friendly precursor. To overcome this, the approach here is to produce the carbon nanomaterials from bio waste, which are oil palm leaves and sago hampas. This bio waste precursor will act as a template for carbon nanomaterials production. This method of producing carbon nanomaterial is not only cost effective and environmental friendly, but also does not involve complicated procedures that need the addition of catalyst.

Apart from that, significant efforts have been done on nanotechnology such as carbon nanomaterial for drug delivery applications since it offers suitable means for delivering drugs for specific target due to the nanoscale size of particles (Kim et al., 2008).

Carbon nanomaterials can enhance the delivering activity of the drugs since the smaller particle size can penetrate deep into cell or tissue and generally can be taken up efficiently by cells (Varghese et al., 2013). Earlier report also mentioned that carbon nanomaterial have high toxicity to the biological system thus, the carbon nanomaterial obtained was used to observe its capability of cellular uptake and also the cytotoxicity of carbon nanomaterial in the cell.

1.3   OBJECTIVES

1) To select suitable bio waste and conduct initial characterization using TGA, XRD and FTIR.

2) To synthesize and characterize carbon nanomaterial from bio waste using XRD, FTIR, TGA and Raman spectroscopy, FESEM-EDX, TEM, BET and Zeta Potential.

3) To synthesize and characterize carbon nanospheres tagged fluorescent dye.

4) To study the application of carbon nanospheres in biomedical field.

1.4   SCOPE OF STUDY

The scope of study is to utilize the bio waste in producing valuable products. The selected bio wastes are oil palm leaves and sago hampas that will be used as precursor to produce carbon nanomaterial where it can be applied in wide area of applications. The bio waste undergoes thermal treatment, which is a single step pyrolysis to produce carbon nanomaterial. The obtained carbon nanomaterial will be analyzed using Fourier Transform Infrared (FTIR), X-ray Diffraction (XRD), Brunauer, Emmett and Teller (BET), and Thermogravimetric Analysis (TGA). Besides that, the measurement of size and morphology of carbon nanomaterials will be done using Field Emission Scanning Electron Microscopy (FESEM)–Energy Dispersive X-Ray (EDX), Transmission Electron

Microscopy (TEM), Raman and Zeta potential. This carbon nanomaterial will be used for biotechnology applications in the cell imaging study.
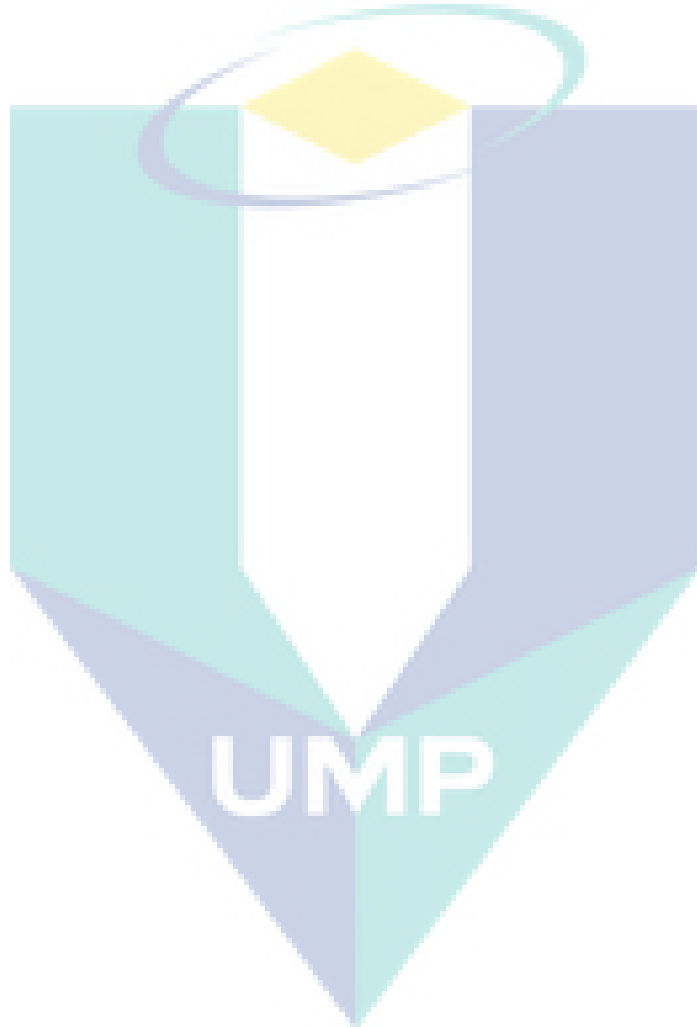
CHAPTER 2

LITERATURE REVIEW

2.1   BIO WASTE

2.1.1   Oil palm trees

Oil palm tree (Figure 2.1) is a well-known and an important crop that contributes in many industrial sectors. About 80 % of world's oil palm is produced from Southeast Asia region (Yuliansyah and Hirajima, 2012) and Malaysia is the largest contributor of all after Indonesia (Sukiran et al., 2011).

Figure 2.1: Oil palm plantation in Malaysia.

Source: Malaysia Palm Oil Council (MPO

Oil palm industry is one of the most important assets for Malaysia as it has high productivity in producing palm oil for household and commercial consumption. As a result, it boosts Malaysian economy and agricultural sectors with the increase of production rate year by year (Sukiran et al., 2011 and Varghese et al., 2013). In spite of its contribution to the economy, this industry also generates large amount of biomass waste, which can be divided into two: plantation waste and milling process waste (Im et al., 2014).

Oil palm industry committed large amount of biomass each year that includes leaves, shell, fronds, trunks, Empty Fruit Bunch (EFB) and Palm Oil Mill Effluent (Sukiran et al., 2011 and Mohammed et al., 2013). In Malaysia, more than 7 million tons of the wastes are EFB, 4.5 million tons contributed by fiber and around 1.9 million tons by shell. To make matter worse, this amount is increasing annually (Yuliansyah and Hirajima, 2012), which subsequently creates the disposal problems and environmental issues (Sukiran et al., 2011 and Das and Saha, 2012).

It cannot be denied that oil palm wastes are one of the common biomass (Figure 2.2) that produces many byproducts wastes and hence, the usage need to be optimized and can be used for creating valuable products. The alternative way of recycling the oil palm waste should be implemented in order to avoid the waste dumping since it may lead to high cost disposal of that particular residues (Sukiran et al., 2011 and Das and Saha, 2012). Research must be conducted to transform the biomass waste into the value added products (Yuliansyah and Hirajima, 2012 and Mohammed et al., 2013).
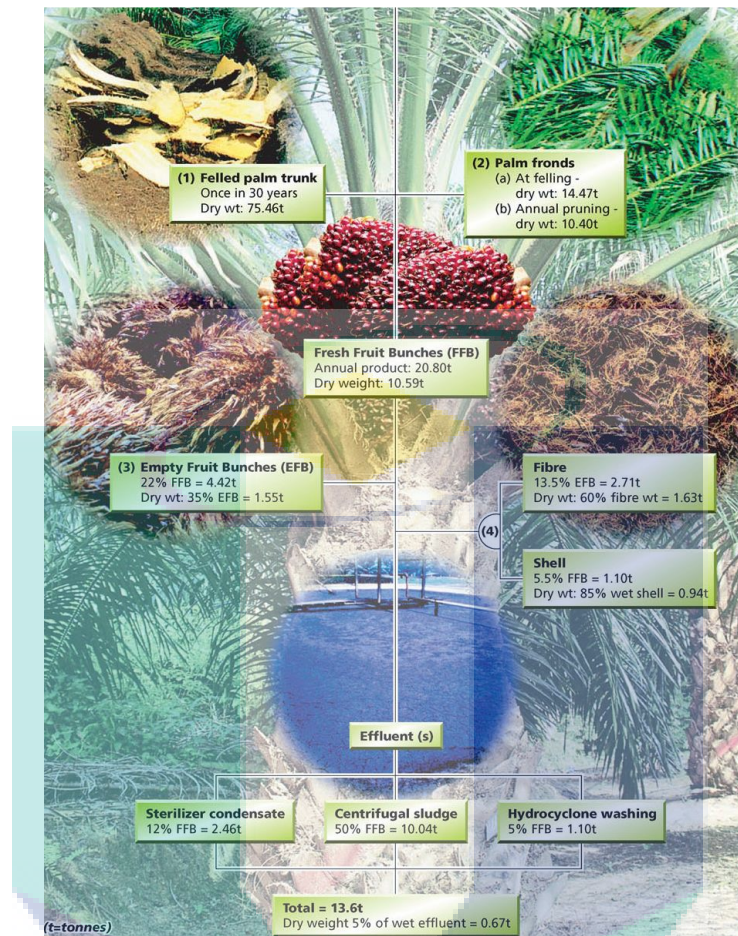
Figure 2.2: Oil palm biomass.

Source: Malaysia Palm Oil Council

The utilization of oil palm waste should be considered since most parts of raw materials from the oil palm tree contribute to 90 % of dumping while only 10 % of it is used for oil making. The mill residues of EFB, shell and fiber have already been employed to other products whereas palm fronds and stems are still underutilized hence making it as the major disposal problems, which can lead to environmental effects (Sukiran et al., 2011). The fronds, also regarded as lignocellulosic biomass from the oil palm industries contribute to around 46,000 kilotons of wastes, the highest compared to other kind of wastes (Sukiran et al., 2011).

2.1.2 Sago hampas

Sago palm is another well-known crop in Sarawak, Malaysia. It has been used for the production of primary starch source. Sago palm plays its roles as raw material for production of sago flour that has the importance in food industries and cosmetics (Mustapa et al., 2007). Having high content of starch, sago palm, as shown in Figure 2.3, is a hard plant which also grows in swampy and peat soils (Awg-Adeni et al., 2010 and Kuroda et al., 2001). The production of sago products annually contributes to tons of agro residues from each sago starch processing mill. Presently, this bio waste from the processing mill is washed away directly into nearby rivers that soon create serious environmental problems especially water pollution (Awg-Adeni et al., 2010 and Tan et al., 2014). So far, the solution applied to the wastewater problems required high cost and thus the exploitation of the residues from sago starch processing is a great approach to preserve the environment. The main parts of the sago waste residues are sago bark and sago hampas that are also known as solid residues.

Figure 2.3: Sago palm tree.

Source: Retrieved from http://www.inriodulce.com/links/sagopalm.html

Sago hampas is one of the fibrous solid residues from the sago starch processing industry but the high fiber content gives problems to the industry. Sago hampas is a lignocellulosic product as it is mostly composed of cellulose and lignins that contains 66 % of starch and 14 % fiber in which 25 % is made up of lignin. Sago hampas residues are difficult to handle since it is problematic for drying process due to the high moisture content and starch especially when it comes to huge amount. Therefore, the solid residues of sago hampas have to be categorized as waste and also pollutant (Awg-Adeni et al., 2010).

2.1.3   Lignocellulosic biomass material

Lignocellulosic biomass materials such as agricultural waste and woody materials are commonly used as starting materials since it is easily available, cheap and environmental friendly. These materials are usually generated from the agricultural based industry as it comes in large amounts and becoming waste products. So, converting the lignocellulosic biomass into the high value added products is a good approach.

Oil palm tree waste such as fronds, leaves, trunks and shells and sago hampas can be considered as lignocellulosic biomass materials. As illustrated in Figure 2.4, the main components in the lignocellulosic biomass material are cellulose, hemicellulose and also lignin. The lignocellulosic materials normally contain 40-60 wt% of cellulose, 20-40 wt% hemicelluloses and 10-25 wt% lignin.

With the highest overall weight percentage, cellulose is a major part that has responsibility for mechanical strength in the cell wall of plant. Cellulose has long polymer of glucose units with no branches and having crystalline, strong and hydrolysis resistant properties. Hemicellulose is a random, amorphous structure that can easily be hydrolyzed by diluted acid or base. Lignin comes in cross-links where larger lignin molecules fill the three dimensions with even more heavy cross linked. It acts as a polymer gap filler between and around the cellulose and hemicellulose. It is also composed of aromatic alcohols, which are conifery, sinapyl and p-coumary alcohol that plays the role of protection seal for the

other two components. Among these three components, hemicellulose is easy to degrade by thermal treatment followed by cellulose and lignin (Yang et al., 2004 and Anwar et al., 2014).
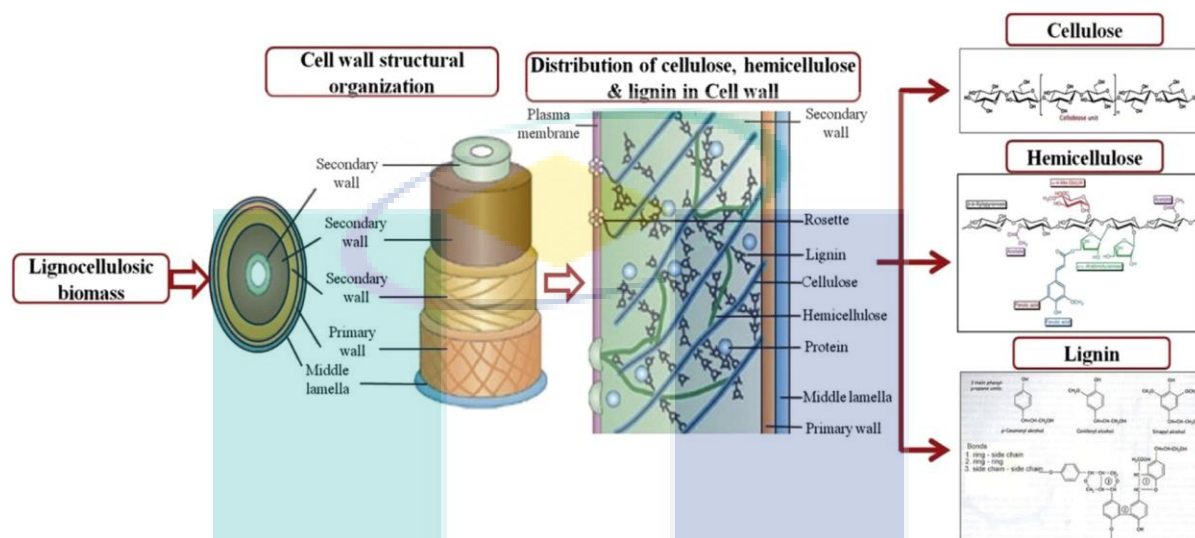
Figure 2.4: Illustration of lignocellulosic components.

Source: Anwar et al., 2014

2.2   CARBON NANOMATERIAL

One of the most abundant elements on earth is carbon whereby the carbon based nanomaterials always get much attention from the scientist since many decades due to their unique properties. The nanostructured material based on the carbon including carbon nanoparticles (Miao et al., 2004), carbon nanotubes (Wang et al., 2008), carbon nanofibers (Knights et al., 1979 and Gao et al., 2012), fullerenes (Galeener, 1979; Galeener and Sen, 1978 and Gao et al., 2012) and many more have been reported. Carbon nanoparticles are in demand due to the variety of properties that can be used in many types of applications in various fields. It has many important properties such as high impact strength, high surface area, optical properties, thermal stability and electrical conductivity (Salman, 2013 and Yuliansyah and Hirajima, 2012).

For instance, carbon nanoparticles have high demand in nanoscience and nanotechnology where it can be applied in wide areas such as in optical devices (Lai and Idris, 2013), antimicrobial agents (Salman, 2013) and pollution prevention materials. In biology field, it can be used as antibodies recognition (Hooi et al., 2009), nucleic acid sequencing and also in bio separation and bio catalysis. Nowadays, too many infectious diseases that are mainly caused by pathogenic microorganisms, unless anti-microbial agents are used, these infectious diseases cannot be cured and prevented. Since the nanotechnology field is a new research area, the nanostructured materials such as carbon nanoparticles can be proposed to be applied in medical and pharmaceutical field because by decreasing the carbon nanosize, the antimicrobial activity increases due to high surface area and it can easily destroy the microorganism cell wall. Thus, the combination between the nanotechnology and microbiology has great potential in curing the diseases (Salman, 2013).

2.2.1 Carbon nanospheres

Carbon nanospheres are known as circular carbon types with bearing concentric graphitic layers in the surface. It is well known for the novel chemical, biological and physical applications (Li et al., 2013). The carbon particle with spherical shapes as shown in Figure 2.5 and Figure 2.6, have very high demand and attracted many attentions due to the wide applications such as biosensor (Wang et al., 2014), electronic devices, catalyst supporter, adsorbents (Walker et al., 1954; Lespade et al., 1982; Cancado et al., 2004 and Tuinstra et al., 1970) and for lithium ion batteries (Krishnamurthy and Namitha, 2013 and Yuan et al., 2008). Besides that, carbon nanospheres also can be used in nanoadditives, energy storage, and separation technology and also as lubricants (Yuliansyah and Hirajima, 2012; Ruan et al., 2014 and Frackowiak and Beguin, 2001).

In addition, the carbon nanospheres are also promising materials for the medicine field, pharmaceutics and material science (Yuliansyah and Hirajima, 2012). The most important key in synthesizing carbon nanospheres with good morphology and high carbon yield depends on the precursor material used (Yuliansyah and Hirajima, 2012 and Trogadas et al., 2014). In order to prepare the carbon nanospheres, there are several methods that

have been used such as chemical vapor deposition (Zhang et al., 2014 and Dikpati et al., 2012), arc plasma techniques, pyrolysis, self-assembly template approach and hydrothermal process (Yuliansyah and Hirajima, 2012). Various types of carbon sources used are based on petroleum precursor using different methods such as laser ablation (Kumar et al., 2013), sol-gel emulsification, spray pyrolysis (Joo et al., 2008), and ultrasonic treatment (Tripathi et al., 2012; Krishnamurthy and Namitha, 2013; Frackowiak and Beguin, 2001; Honary and Zahir, 2013 and Selvi et al., 2012). When it comes to the environmental impact, this kind of precursor has to be avoided and researchers keep searching for better precursor that is environmental friendly and natural carbon sources are seems to be the better choice (Tripathi et al., 2012; Yang et al., 2004 and Qian et al., 2014).
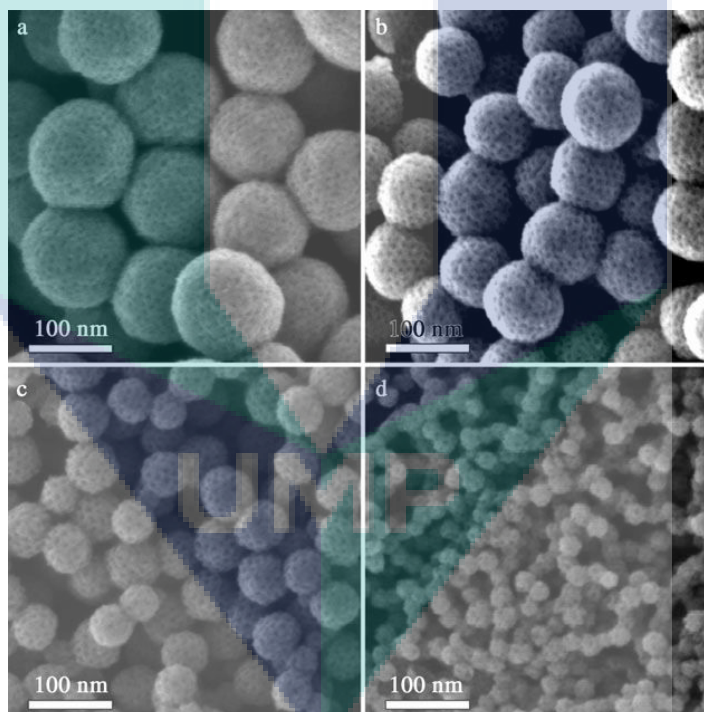
Figure 2.5: Ordered mesoporous carbon nanospheres by using phenolic resol as carbon source.

Source: Fang et al., 2010

Other than that, carbon spheres (1-10 µm) were synthesized from carbonization of polyethylene-poly- (vinyl chloride) in a sealed gold tube and carbon vapor from β-SiC powder decomposition. Fullerene synthesis at 2500-2600 °C without catalyst using deposition of gaseous carbon in helium also produced carbon spheres (20-500 µm) as a side product (Li, M. et al., 2009). These methods need a very high production cost for the experimental conditions and also complicated hence it gives limitations for producing large amounts of carbon spheres. These limitations allow researches related to the carbon field to find new or optimize the synthesizing method in order to produce in large amounts of material (Qian et al., 2014 and Li, M. et al., 2009).
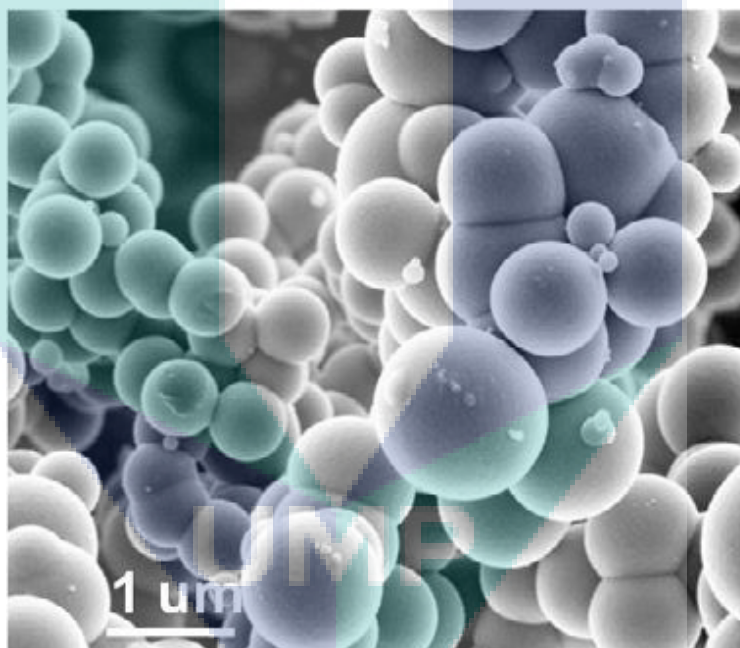
Figure 2.6: Scanning Electron Microscopy (SEM) images of carbon spheres that synthesized based on resorcinol formaldehyde resin.

Source: Zhang, et al., 2014

Reports in carbon spheres research is still little in number compared to other nanomaterials such as the fullerenes, carbon nanotubes and nanofibers studies. Carbon spheres have similarity to graphite that allows them to be use in variety of applications. However, preparing large amount of carbon nanospheres need high cost and the experimental conditions are complicated since not much research have been done to overcome these limitations (Li, M. et al., 2009).

All these reported methods used to synthesize carbon nanospheres with different kind of carbon sources are complicated, time consuming, tedious and involve complicated equipment. The most serious issue is the high cost production when it reached the pilot scale stages. These limitations inspired the researchers not only to find out the simple, lower temperature and cost effective method but also produces high quality carbon nanospheres since it has very wide applications.

Generally, there are three approaches for production of carbon nanospheres. Firstly, it can be synthesized by chemical vapor deposition, hydrothermal treatment and pyrolysis. Secondly is the usage of hard templates (Joo et al., 2008; Li, G. et al., 2008 and Abdullah and Sulaiman, 2013) and thirdly by polymer synthesis followed by thermal approaches in inert atmosphere (Mohan and Manoj, 2012).

Among all available methods, synthesizing the carbon nanospheres using pyrolysis method is the simplest. Pyrolysis is the method been reported earlier where synthesis of carbon nanospheres was done by thermal treatment in an inert atmosphere. The pyrolysis method is one of the ways to control the size of carbon nanospheres easily. As reported before, the carbon nanospheres had been synthesized by using polymer as a precursor and undergone the heat treatment up until 1000°C with a size more than 200 nm and also microspheres sizes of carbon (Krishnamurthy and Namitha, 2013). So, the selection of the ideal precursor and pyrolysis step especially temperature tuning is very important to produce and control the sizes of carbon nanospheres. This become the challenge as to produce high quality carbon nanospheres, which is worth of hard works in carbon nanospheres field due to its wide area of applications.

In order to produce the cost effective production of nanoparticles, the precursor of raw material should be low cost and readily available. When the production cost is low, it is possible to produce this material in a large scale. Here, the approach is to produce carbon nanospheres using bio waste commonly found in nature where it can cut the cost hence can preserve the nature from pollution. This technique of single pyrolysis step by using bio waste without addition of any catalyst at low temperature will efficiently produce high quality carbon nanospheres with porous nature for large scale production.

2.3   APPLICATIONS OF CARBON NANOSPHERES

2.3.1   Cell Lines

Melanoma which is the most killer type of skin cancer is rapidly spreading compared to other types of cancer. Additionally, melanoma incidence hits the white populations around the world due to the increase of thin rather than thick melanomas (Su et al., 2009). Melanoma is a skin cancer that comes from the malignant melanocytes transformation (Looi et al., 2013 and Chodurek et al., 2010). Majority of melanoma cases occur in a skin, whereby it is rarely detected in an eyeball, brain meninges, genitalia and mucous membrane of oral cavity (Chodurek et al., 2010).

The cases of melanoma around the world are doubling each year (Caputo et al., 2011 and Looi et al., 2013). Most of the patients (80 %) found to be cured by surgical excision since it was detected at early stage. However, metastatic melanoma has an unfavorable prognosis with median rate of survival (Caputo et al., 2011 and Su et al., 2009). In addition, no prospective information is available to clearly expose the prevention and early detection efficiency of this tumor. Even though many discoveries were found in this melanoma cases in terms of therapeutic approaches, yet there is still a need in improvement of treatment and survival rate of patients (Caputo et al., 2011).

Each of cancer cells has different sensitivity to chemotherapy and malignant melanoma is one of the most challenging cancers to treat. The number of effective therapies for this disease was low due to drug resistance in malignant melanoma (Chen et al., 2014). Besides that, the rapid proliferation and high resistance to current treatment of malignant melanoma creates high demand for alternative therapies (Chodurek et al., 2010). Therefore, the mechanisms of melanoma development are critical for efficient therapeutic strategies (Caputo et al., 2011).

Neuroblastoma is the most common cancer arising from neural crest cells found in infants and young children. Most patients in stages 1 and 2 can be cured through chemotherapy and surgery (Weinstein et al., 2003). Neuroblastoma was diagnosed as disseminated disease especially at stage 4 in 60 % cases. Compared to other type of malignant cancer, stage 4 neuroblastoma diagnosis shows three distinct clinical patterns based on the distribution of disease and patient's age. The disseminated form of neuroblastoma affects infants in the first few months of life. The rapid growth of tumor is usually followed by spontaneous slower regression of it. Stage 4 of neuroblastoma is often diagnosed by small size of adrenal tumor, with skin and liver disease by modest bone marrow involvement. For stage 4 patients, the extensive involvement of bone marrow was common and frequently happened in older patients with bone lesions (Benard et al., 2008).

Neuro 2A (N2A) is a mouse neural crest-derived cell line that has been extensively used to study neuronal differentiation, axonal growth and signaling pathways. A convenient characteristic of these cells is their ability to differentiate into neurons within few days. For instance, the neural crest-derived N2A cell line has been widely used to study neuronal differentiation, neurite growth, synaptogenesis and signaling pathways. N2A cells have the advantage of responding quickly to serum deprivation and other stimuli in their environment by expressing signaling molecules that lead to neuronal differentiation and neurite growth (Tremblay et al., 2010).

Madin-Darby canine kidney known as MDCK cells are a permanent cell line derived from dog kidney that are widely used as a cell line model for studies in cell growth regulation (Irvine et al., 1999), epithelial polarization, formation and regulation of tight junctions, epithelial transport and mechanisms of infection (Lang and Paulmichl, 1995). MDCK cells have the ability to differentiate into columnar epithelium and form tight junctions when cultured on semipermeable membranes. MDCK cell line is used as a model for cellular barrier for assessing intestinal epithelial drug transport since it is a good candidate for simple epithelia modelling (Irvine et al., 1999).

MDCK cells are commonly used for isolation of influenza viruses due to its high sensitivity to infection of different influenza strains. Because of this ability, MDCK cells have been used as a substrate for isolation of influenza virus and production of vaccine (Seitz et al., 2010). Furthermore, MDCK cell can proliferate in suspension where it is important to facilitate scale up process for influenza virus production. It is reported that MDCK cell is an excellent producers for several viruses especially influenza A and B viruses (Chu et al., 2009).

There are many types of cancer cell lines that have been used to study the cell activity towards the carbon nanospheres. The cellular uptake of carbon nanospheres can enhance the drug delivery to the specific target, which is cancer cell by not interfering with normal cells. The higher efficiency of drugs to reach the specific target can optimize the drugs effect. This approach can be as an alternative way for chemotherapeutic agents that have side effects to the patients.

2.3.2 Cell Imaging

Carbon nanospheres can be applied in the field of medicine where it can merged with fluorescent materials and these properties are useful for biological system such as tumor cell detection and cell tracking (Selvi et al., 2008 and Vakili et al., 2014). For the cell imaging and drug delivery, usually the nanospheres are tagged with fluorescence agent such as Coumarin (Doolanea et al., 2014) and antibodies (Vakili et al., 2014).

Targeted drug delivery is a process where the drug is targeted and focused towards the specific site hence it would prevent the drug from affecting the other parts of body. This method improves the affectivity of the drug itself for therapeutic purposes. For example, Central Nervous System (CNS) is an important specific area that drugs should reach efficiently where it can treat neurological disorders and various other diseases. However, the big problem is the presence of protective barriers, (Blood Brain Barrier and Blood Cerebro Spinal) which are not allowing the drugs to enter it and making brain unreachable for insoluble lipids compounds such as polar molecules and small ions (Kim et al., 2008 and Dikpati et al., 2012).

The presence of nanotechnology in this field gives better penetration of therapeutic and diagnostic agents for drug delivery (Han et al., 2011). These nanomaterials are able to transfer the drugs pass through the barriers with its target to the specific tissue or cells. The nanoparticles have many benefits towards the drug delivery system where the nanoparticles synthesis should be easy, stable and also can protect drugs from chemical and enzymatic degradation. Nanoparticles also can be combined with imaging or sensing agents to gain multifunctionality. The small size of particles has the ability for easy penetration into the small capillaries that allow the drug to accumulate efficiently to the target cells. The excellent nanoparticles properties in drug delivery system should be non-toxic, biocompatible and biodegradable. It should have narrow particle sizes and less than 200 nm. Besides that, the nanoparticles also should be stable in blood where no aggregation occurred (Kim et al., 2008 and Dikpati et al, 2012).

In the field of medicine, cancer therapy is aiming to the goal to achieve high drug efficacy and decrease the toxicity. Chemotherapeutic drugs used are having side effects so there should be a way to solve these problems and increase the efficacy of drugs while delivering it directly to the tumor cells. Previously, gold nanoparticles have been used for the drug delivery system, but the toxicity effects of the nanoparticles occurred since it is made of heavy metals thus making it the limitations for the applications. Furthermore, gold nanoparticles also are able to suppress the fluorophores that exists in the fluorescence material, which is not suitable for in vivo tracking. Recently, the fluorescent carbon

nanoparticles (Poinern et al., 2012) have been discovered that can be an alternative way for cancer therapy. The studies on toxicity of carbon nanoparticles proved that it is non-toxic to living things. Demonstrations have been done for in vitro and in vivo studies where the cell with carbon nanoparticles performed more than 80 % of survival rates for in vitro studies while showing lower toxicity as no toxicity sign in the treated mice for in vivo. These studies represented the carbon nanoparticle as almost nontoxic and biocompatible (Lee and Moon, 2014). Apart from it, there are very few reports on the carbon nanospheres for the cell imaging applications and drug delivery (Dawood and Hassan, 2014 and Roslan et al., 2014).

Carbon nanospheres have the unique characteristics where it has low toxicity, low photo bleaching, no optical blinking, and biocompatible. These unique properties make the carbon nanospheres play its role as an alternative way for biological applications. It is reported that carbon nanospheres can be taken up by cells depending on the time and concentration used. Carbon nanospheres showed low cytotoxicity and well hemocompatibilty (Roslan et al., 2014 and Ray et al., 2009). It can be taken up by cell and in vivo, carbon nanospheres are mostly distributed into heart where it has high potential for heart diagnosis probe while the rest were distributed into spleen, liver and kidney. Carbon nanospheres have high potential for heart cell imaging since no obvious toxicity shown and hemolysis rate was lower. It can be said that the carbon nanospheres can be applied for cell imaging, tracking in vivo and drug delivery (Yuliansyah and Hirajima, 2012; Dawood and Hassan, 2014 and Roslan et al., 2014).

CHAPTER 3

METHODOLOGY

3.1 SAMPLE PREPARATION

The sample collection was done by collecting oil palm fronds, a bio waste from the nearby plantation in Malaysia. The leaves were separated from the fronds part. Besides that, another bio waste was sago hampas, which was collected from Sarawak areas. The oil palm leaves (OPL) and sago hampas (SH) were then crushed into small pieces and further dried by keeping it in the oven at 60 °C for two days to remove the moisture content. After that, the bio wastes were grinded into smaller size at speed of 12000 rpm using grinder (Retsch, ZM 200, Germany). The grinded bio wastes were further sieved into smaller particle by the size of 62 μm.

3.2 SYNTHESIS OF CARBON NANOSPHERES

The carbon nanospheres were synthesized using single step pyrolysis where it underwent thermal treatment in the tube furnace (Nabertherm, EW-33334-36). The sample was placed in the tube furnace connected with temperature controller. The tube was connected to the nitrogen gas cylinder and flow meter was used to control the gas flow as shown in Figure 3.1. It was also connected with water bubbler at another end of tube to allow excess gas to escape from the furnace and also acted as cooling system.

.

The temperature in the range of 400- 700 °C was used to pyrolyze the sample under continuous nitrogen flow of 150 ml/cm^3 with the heating rate at 5 °C/min for 2 hours. After reaching the final temperature, the sample was cooled to room temperature, with the nitrogen atmosphere in order to obtain the pyrolyzed sample.
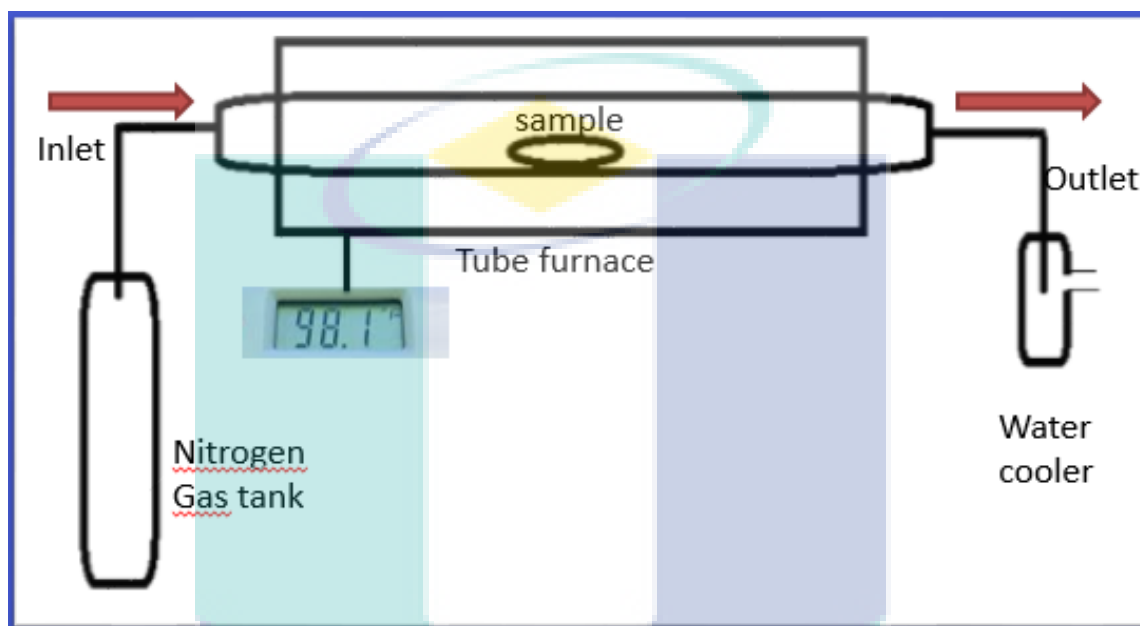
Figure 3.1: The experimental set up for one step pyrolysis.

3.3   CHARACTERIZATIONS

The obtained bio waste precursor and synthesized carbon nanospheres were characterized using Fourier Transform Infrared Spectroscopy (FTIR) (Perkin Elmer, Spectrum 100), Field Emission Scanning Electron Microscopy- Energy Dispersive X-ray (FESEM) (JEOL, JSM-7800F), X-Ray Diffraction (XRD) (Rigaku Miniflex II) and Transmission Electron Microscopy (TEM) (JEOL, JSM 1230). The surface area and pore width was measured using BET (Micromeritics ASAP 2020) with degassing at 200 °C for 12 hours. The Raman spectra were measured using HORIBA Scientific Raman spectroscopy while zeta potential values were measured using Zetasizer (Malvern).

3.3.1 Fourier Transform Infrared Spectroscopy (FTIR)

An infrared spectrum defines as a fingerprint of materials with absorption peaks that corresponds to vibrations frequencies between atoms bond that making up the material. So, each of compound in the materials have different kind infrared spectrum. Hence, it is good analysis to detect and identify the material presence in the system.

In the FTIR machine, a moving mirror, fixed mirror, beam splitter, IR (Infrared) radiation source and detected are included. Michelson interferometer used for IR radiation analysis after passing through sample and collimated by mirror. The resultant beam is divided at beam splitter. Half of beam passes through fixed mirror and half refracted to moving mirror. The two light beams from the mirrors recombined at beam splitter where the interference wave formed. It passes through cell and after that radiation are focused to detector. The detector will measures all frequencies that pass through the cell and routes the information to the computer. The information received is decoded by Fourier transformation and decoded spectrum is directed to data form (Baravkar, 2011 and Faix, 1992).

FTIR measurements were used to determine the presence of functional groups in the bio waste and in the synthesized carbon nanospheres. The small amount of sample was mixed with potassium bromide (KBr) by grinding it using mortar and pestle. It was grinded into a fine powder and was put between two stainless steel disks. The sandwich was transferred into the pistil in the hydraulic press for few seconds before the pressure was released. The disks were removed and the pellet was taken out, which was been inserted into the sample holder before running the spectrum in the range of wavelength 400-4000 cm^{-1} with transmittance units.

3.3.2   X-ray Diffraction (XRD)

Solid matter is divided by amorphous and crystalline material. The atoms are arranged in a random way for amorphous material. In another way, the crystalline material having an atoms that are arranged in ordered pattern and there is a smallest volume element in three dimensions, can describe the crystal. XRD is a powerful method to study the crystal structures and atomic spacing. In XRD, the powder diffraction is mainly used for various solid materials where it is important to have a sample with a smooth plane surface. The ideal sample is homogenous and the sample is pressed into a sample holder to obtain a smooth flat surface (Sharma et al., 2012).

A typical powder XRD components included an X-ray source, specimen stage, receiving optics and X-ray detector. The source and detector lie on the circumstances of focusing circle and at the center of the circle is the specimen stage. Bragg's law is used to make accurate quantification for crystal structures determination. The fine powder of sample is mounted on the sample holder and when an X-ray beam is incident on the sample, it is scattered by each atom in the sample. The atomic planes from where the X-rays are scattered is called as reflecting planes (Sharma et al., 2012).

X-ray diffraction is based on constructive interference of monochromatic X-rays and a crystalline sample. A typical diffraction spectrum consists of a plot of reflected intensities versus the detected angle 2θ. The 2θ values of the peak depend on the wavelength of the anode material of the x ray tube. For practical applications of X-ray diffraction, X-rays of a single wavelength, i.e. monochromatic radiation usually used to improve experimental results. The Bragg's law relates the wavelength of the reflected X-ray, the spacing between the atomic plane and the angle of diffraction. These diffracted X-rays are then detected, processed and counted. Conversion of the diffraction peaks to d-spacing gives identification of the material because each material has different d-spacing where it can be compared with standard reference pattern. A key component of all diffraction is the angle between the incident and diffracted rays (Sharma et al., 2012 and Fultz and Howe, 2013).

The X-ray diffraction measurement was carried out to measure the average spacing between layers or rows of atoms presents in the material. It is also used to determine the crystalline behavior of the material. The powder material sample was mounted onto sample holder and levelled using spatula before inserted into the XRD instruments. The measurement conditions are shown in Table 3.1.

Table 3.1: Measurement conditions of X-ray diffractions.

Parameter	Conditions
X-ray detector	Copper tube
Generator voltage	30kV
Generator current	15mA
Scanning range	10-80°
Scan speed	1 deg/min
Sampling step	0.02°

3.3.3 Raman spectroscopy

Raman spectroscopy is based on vibration of molecules that can be used to observe the chemical and physical structure of material based on light scattering. When monochromatic radiation is incident on the sample, the light will interact with the sample either it may reflected, absorbed or scattered. In the Raman spectroscopy, it measures the scattering radiation that occurs upon the sample. The scattered radiation produces the frequency (wavelength) of the incident radiation (Rayleigh scattering) and small amount of radiation that scattered in different wavelength (stokes and anti-stokes). The change in

wavelength is useful to study the chemical and structural information of the sample (Smith and Dent, 2013).

The scattered light consists of two types which are elastic and inelastic scattering. The major part that scatter elastic where the energy of incident light is equal to emitted light. This is known as Rayleigh scattering. The minor part that scatters inelastically is called Raman spectroscopy where the energy and wavelength of incident and scattered light are different. Inelastic scattering can be divided by two based on the molecule energy state. The first one is called stokes scattering where the Raman scattering process from the ground vibrational state lead to the absorption of energy by the molecules and it promoted to excited vibrational state. The second one is called anti stokes Raman scattering where the molecule is at excited vibrational state and after excitation the photo falls back to ground state. Anti-Stokes-Raman scattering is mostly weaker than Stokes-Raman scattering as the vibration frequency increases due to the decreased of excited vibrational state population. So, Stokes-Raman scattering is mainly measured in Raman spectroscopy (Smith and Dent, 2013).

Raman spectroscopy instrument consist of Raman spectrometer, measurement cell, potentiostat and computer. The light source of a Raman spectrometer is a laser with a specific wavelength. The light beam is focused on dichroic filter and it will be reflected to the sample. The resulting Raman scattering will be focused back to the filter. It acts as band stop filter as it isolate the single laser beam. The measured light is redirected by mirrors to monochromator by using grating to diffract the beam into wavelength with narrow band. The detector such as CCD (charge couple devices), then measured the photo current produced from each wavelength section. The measured data is then can be evaluated (Bumbrah and Sharma, 2015).

3.3.4 Field Emission Scanning Electron Microscopy (FESEM)-Energy Dispersive X-ray (EDX)

FESEM was used to measure the images and particles size from the sample. EDX was also used to measure the elemental content in percentage and atomic value of the material. The sample powder was placed on the double-sided carbon tape and mounted on a sample stub. No sputter coating was required. Sample was then fitted into the vacuum chamber for Field Emission Scanning Electron Microscopy and further analyzed for Energy Dispersive X-ray (EDX) for the elemental analysis of the sample.

The field emission scanning electron microscope (FESEM) one of the electron microscope that can view the images of the sample surface by scanning with a high-energy electron beams in a raster scan pattern. The field emission was produced by electron emitter where it can produce up to 1000 x the emission of a tungsten filament. However, higher vacuum conditions are needed for this process. After the electrons beam exit the electron gun, it will confined and focused into a thin focused, monochromatic beam using metal aperture sand magnetic lenses. Detectors of each type of electrons in the microscopes will collect signals to produce an image of the specimen (Alyamani and Lemine, 2012).

The FESEM works when the electrons are produced from a field emission source and accelerated in a high electrical field gradient that can be known as primary electrons within high vacuum column. The primary electrons are focused and deflected by electronic lenses to produce a narrow scan beam that bombards the object where the secondary electrons are emitted from the object. The angle and velocity of these secondary electrons relates to the object surface structure. A detector will detect the secondary electrons and produces an electronic signal. The signal is amplified and transformed to a video scan-image that can be seen through computer to be processed further for example in terms of magnification (Alyamani and Lemine, 2012).

For measuring the images in FESEM, the important condition for the sample is that it must be conducting in nature. There is no problem in handling the metallic/conducting sample. But different case for insulators where it should be coated by extremely thin layer (1.5-3.0 nm) of conducting material such as gold to get clearer images (Sengupta and Sarkar, 2015).

EDX is a suitable method for elemental analysis where each of the different element having their own unique structure hence creates particular peaks from X-ray emission spectrum. The sample is being bombarded with high charged particles (proton, electron or X-ray). These highly charged particles will collided with electron that might make it get out from its shell created an electron hole in its place. So, an electron from higher energy shell will come to occupy that hole and the energy in the X-ray form releases. The emitted ray energy is corresponding to the energy difference between the higher energy shell (where the electron came in) and the lower energy shell (where the electron come out). This emitted energy is unique to the corresponding electron shells and subsequently the atomic structure of the element. Hence, the element can be identified from the value of the emitted energy and thus the constituent elements of the sample can be known along with the atomic percentage of each element (Sengupta and Sarkar, 2015).

3.3.5 Transmission Electron Microscopy (TEM)

The TEM was used to measure the images of the material structure with very high resolutions hence it can measure very fine particles sizes. The sample preparation for the TEM instruments was prepared by dispersing the sample powder in the DMSO solution, followed by few minutes of sonication. A drop of dispersed suspension was dropped onto the carbon grid and allowed to dry in order to remove the DMSO from the material. The sample was then mounted into sample holder and inserted into the instruments.

A modern TEM is consists of an illumination system, specimen stage, objective lens system, the magnification system, the data recording system, and the chemical analysis system. In the illumination system, the electron gun is the man component. LaB6 usually

used for thermionic emission source or a field emission source where it gives a high illumination current, but not as high as field emission source. Field emission source is unique for performing high coherence lattice imaging, electron holography, and high spatial resolution microanalysis. The illumination system has the condenser lenses that important for fine electron probe formation. Other than that, the specimen stage is the place to carrying out structure analysis, because it can be used to perform in situ observations by induction of annealing, electric field, or mechanical stress. Hence, it can possibly give the characterization of physical properties for the material measured. The objective lens in the TEM determines the limitation of image resolution. The magnification system consists of two types of lenses, which are intermediate lenses and projection lenses. This lenses can contributes up to 1.5 million magnification. The data recording system is used with a charge coupled device (CCD), for quantitative and quantification data processing. Finally, some of the TEM instrument is attach with the chemical analysis system that is known as energy-dispersive X-ray spectroscopy (EDS) and electron energy loss spectroscopy (EELS). Both of this spectroscopy is able to quantify the chemical composition of the material (Wang, 2000; Reimer, 2013 and Egerton, 2006).

3.3.6   Brunnaer–Emmet–Teller (BET)

The BET theory of determination of surface area is based on the physical adsorption of gases on the external and internal surfaces of a porous material. The relation between the relative vapour pressure and adsorbed gas amount at constant temperature is known as adsorption isotherm (Fagerlund, 1973). Apart from that, BET also commonly used to determine the surface area, pore size and pore width, besides identifying the porosity of the obtained nanomaterials. Adsorption can be divided by monolayer and multilayer where monolayer can be best describe by Langmuir isotherm and multilayer by BET theory. In the adsorption process in the BET method, the surface will adsorb the gas molecules onto the surface sites followed by the formation of monolayer (one molecules thickness) that derived from the Langmuir's model and as the gas pressures increases the formation of multilayer molecules that fit the Brunnaer–Emmet–Teller theory where it can determine the

surface area. After the complete coverage of molecules and all pores are filled, the BJH derivation can be used to determine the pore size, pore volume and distribution.

The Langmuir's model work on monolayer adsorption where the adsorbed amount corresponds to complete monolayer coverage (Sing, 2001). IUPAC classification on pores width are macroporous materials should be more than 50 nm, mesoporous in between 2 – 50 nm and microporous is less than 2 nm. (Sing, 1998). As in the Langmuir theory where it assumes monolayer adsorption, the adsorbent surface is pictured as an array of equivalent sites on which molecules are adsorbed in a random manner. It is assumed that the occupation probability of a site is independent of the occupancy of neighboring sites and that there are no lateral interactions between the adsorbed molecules (i.e. the ideal localized monolayer) (Sing, 2001).Besides that, Langmuir isotherms also refers to homogenous adsorption where all sites possess equal affinity for the adsorbate. Moreover, it is characterized by a plateau, a saturation point where once a molecule occupies a site, no further adsorption can take place (Foo and Hameed, 2010).

Surface area is the external surface area of a solid object including surface attributable to pores. Brunnaer Emmet Teller is the best method to determine the surface area of materials where it derived the isotherm for multilayer adsorption (Foo and Hameed, 2010 and Joyner et al., 1945). It assumes a random distribution of sites that are empty or that are covered with by one monolayer, two layers and so on, as illustrated alongside. The BET surface area usually obtained from Brunauer, Emmett and Teller theory to analyze nitrogen adsorption/desorption isotherms measured at 77 K. The physical adsorption of inert gas usually nitrogen (argon and krypton can be used) is the best method for surface area and morphologies properties of porous solids. The amounts of nitrogen molecules adsorbed onto the sample using either gravimetric, volumetric or dynamic flow through methods. The model for BET isotherm uses binding energy between adsorbate and surface for the first monolayer taken as equal to the isosteric heat of adsorption, and a second binding energy for adsorption of all subsequent mono layers that is taken as equal to the molar heat of condensation (Tan et al., 2012).

Total pore volume is derived from the amount of vapor adsorbed at a relative temperature close to unity (assuming pores are filled with liquid adsorbate). Pore radius is the average pore size can be estimated from the pore volume. Theory of BJH is the popular method for pore size distribution from nitrogen isotherm (Sing, 2001). The Barrett-Joyner-Halenda (BJH) method for calculating pore size distributions based on a model of the adsorbent as a collection of cylindrical pores. The method accounts for capillary condensation in the pores using the classical Kelvin equation. In each pore the total excess adsorption is given by a surface layer thickness plus a pore-filling term; the pore is filled if the pressure satisfies (Gelb and Gubbins, 1999). The Kelvin equation relates the amount of adsorbate removed from the pores of the materials, as relative pressures is decreased from a high to low value, to the size of the pores.

A 100 mg of synthesized carbon nanospheres was transferred into the sample tube. It was degassed at 200 °C for 12 hours in order to remove the moisture and volatile compounds. The experiment was run isothermally at -196 °C with continuous nitrogen flow applied.

3.3.7   Thermogravimetric Analysis (TGA)

The TGA curves measured the weight loss of the sample used. An initial measurement was done for the bio waste to determine the needed temperature for the pyrolysis. The pyrolysis temperature used was determined from the TGA curves of bio waste precursor. The sample was placed on the aluminum pan with continuous nitrogen flow with heating range from 30-1100 °C with heating rate of 10 °C/min.

TG is a technique where the substance weight in the environment that being heated or cooled at controlled rate, and recorded as a function of time or temperature. The data obtained are showed as thermal curve with weights unit/percent versus temperature/ time units. So TGA is suitable method to observe the weight loss of the substances according to temperature varies. TGA have wide range of properties such as thermal stability, oxidative stability, effect of different atmosphere and moisture and volatile content (Pan et al., 2005).

The most important part in the TGA instrument is the furnace and balance. Measurement of changes in the sample mass with temperature is using thermo balance with a pan loaded with the sample and furnace. The sample is loaded into the pan that attached to sensitive microbalance. After that, the sample holder of TGA balance is then placed into the furnace. The furnace can be controlled or programmed for specific heating rate or temperature range versus time. In the sample chamber, the atmosphere should be purged with inert gas to avoid oxidation. The balance allows the measurement of changes of weight of the sample. The balance should be in suitably enclosed system so that the atmosphere can be controlled. The TGA instrument continuously weighs a sample as it is heated. As the temperature increases, various components of the sample are decomposed and the volatile products can be measured. The data collected in then converted into thermogram (McMahon, 2008).

3.3.8   Zeta Potential

Zeta potential analysis is a method to determine the surface charge of nanomaterial (also known as colloids) in solution form. Zeta potential values provide key information about the nanoparticles stability in suspensions and cellular uptake (Zeng et al., 2013 and Perrault et al., 2009). Zeta potential is measured to determine the suspension's ability of the particles in solutions. Zeta potential is the electro kinetic potential in colloidal systems where it referred to potential differences between the medium of dispersion and fluid stationary layer that are attached to the dispersed particle (Honary and Zahir, 2013). Nanoparticles have a surface charge that attracted opposite charge of ions thin layer to nanoparticles' surface. The double layer of ions and nanoparticles will spread throughout the solutions. The electric potential at double layer boundary is known as Zeta potential. The common range of the zeta potential values is from +100 mV to -100 mV. The colloidal stability can be determined by zeta potential values where the range from +30 mV or less than -30 mV is having high degrees of stability (Zeta potential analysis of nanoparticles guidelines, 2012). As the zeta potential increases, the larger repulsive interactions will be, hence creating more stable particles with uniform size (Hans and Lowman, 2002).

Zeta potential is a technique to find out the surface of nanoparticles state and its long term stability. It can influence the pharmacokinetic properties in the body that also affects the phagocytosis of nanoparticles in the blood (Honary and Zahir, 2013). The zeta potential was measured using the capillary cell along with two gold electrodes. The voltages up to 200 V were applied and the movement of particles was observed. It measures the phase changes in light scattered of moving particles with the influences of electric field (Zeta potential analysis of nanoparticles guidelines, 2012). It has been used in cell biology for adhesion of cell, activation and agglutination depending on surface charge properties of the cell involved (Zhang et al., 2009).

The sample preparation was done by dispersing the small amounts of the carbon nanomaterial into the deionized water. The dispersed solution was then filled into capillary cells. It should be injected slowly to prevent the formation of bubbles in the cells. The cell was then placed into the Zetasizer to measure the zeta potential values.

3.4   CELL IMAGING STUDY

3.4.1   Materials

Dulbecco's Modified Eagle's Medium (DMEM), Fetal Bovine Serum (FBS), Penicillin-streptomycin, Insulin, TrypLE™ Express were purchased from Gibco (Paisley, UK); MTT from Invitrogen (USA); DMSO from Sigma-Aldrich (St. Louis, MO, USA); Cell culture plastics from Nunc Thermoscientific (USA); Cell lines UMR 106 (ATCC® CRL-1661™), A-375 (ATCC® CRL-1619™), N2A (ATCC® CCL-131™) and MDCK (NBL-2) (ATCC® CCL-34™) from the ATCC (Rockville, MD, USA). Tissue culture vented flask 25 cm^2 and 75 cm^2; 10 cm^2 and 6 cm^2 tissue culture dishes; 5 and 10 ml serological pipettes; 200 μl, and 1000 μl pipette tips were purchased from Corning, (USA); 6, 12, 24 and 96 well plates from Greiner Bio-one CELLSTAR (Germany).

3.4.2   Cell culture

Next, cell culture experiment was done to be used for tagging the carbon nanospheres. First of all, seeding of cell culture was done by preparing the cell lines in the four T-flask that contained media of Dulbecco's Modified Eagle Medium (DMEM) with 10 % fetal bovine serum (FBS) and 1 % antibiotic (streptomycin). After that, media was removed from the flask. The flask was washed with PBS few times to remove serum that might inhibit the activity of trypsin. Next, 500 µl of trypsin EDTA was added into the flask as a detaching media and incubated at 37 °C for 1 minute. After incubation, the trypsin EDTA was removed and the cell was neutralized by 5 ml media. The cells were detached by pipetting up and down the media through the surface for few times. The cell suspensions from all flasks were gathered in one flask. The measurement of cell count was done by haemocytometer. A 2 µl of cell suspension was taken and dropped onto the haemocytometer slide and was observed under microscope. Cell count was done to determine the amount of cells suspension needed to reach cell density of 1.5×10^5 cells/ml.

Then, it was proceed by cell transfection where the incubated cells from seeding process were observed visually to detect any contamination. If the nanospheres solution turned to cloudy, it might be contaminated. The old media was removed and 900 µl of fresh media was added into each well plate. This step should be done in sterile biosafety cabinet.

3.4.3   Fluorescence imaging

For the cellular uptake, a 100 µl of CNSs suspension tagged with C-6 was used. A new 24 wells plate was employed and the calculation had been done to get the total amount of nanoparticles solution with C-6 needed for each well. These calculations were done for three ratios, which are 5, 50 and 100. Experimental set up was started by swabbing the laminar cabinet, apparatus and materials needed with alcohol and sterilized under UV light for 15 minutes. All formulations had been added into the well according to the calculated amount with aseptic techniques applied. After that, the plate was incubated for 1 hour at

37 °C. Finally, the plate was then observed under inverted microscope together with the other two plates prepared for cell transfection.

Later, an experiment had been done for tagging the carbon nanospheres with dyes, which was C-6 for fluorescence imaging. C-6 mixed with carbon nanospheres was prepared. A 10 mg of carbon nanospheres was added into 1 % of C-6 solution, and stirred continuously for six hours. After that, the remaining of C-6 was separated by centrifugation. The particle was washed for few times with distilled water. Then, the obtained carbon nanospheres were used for fluorescence imaging and cell uptake study. C-6 was added as fluorescence probe. Cell uptake study was performed according to the method described by Doolaanea et al (2014). UMR 106 (OSTEOBLAST) cells were obtained from American Type Cell Culture (ATCC). Cells were seeded at 1.5×10^5 cells/well in 24 well plates for 24 hours prior to cell uptake study. Cells were treated with 100 μg of C-6 tagged carbon nanospheres. After 72 hours, cells were washed with ice cold PBS to remove the excess nanoparticles and the images were captured with a Nikon Eclipse Ti fluorescence microscope. After that, the different type of cell lines are also used for the cell uptake study of tagged CNSs.

3.4.4 Cell viability

Cell viability was evaluated by the conversion of MTT, 3-(4, 5-dimethylthiazol-2-yl)-2, 5-diphenyltetrazolium bromide to formazan as described previously by Han, Jung, and Park (2012) with slight changes. The cell lines were seeded in 96-well plates at density of 2.0×10^4 cells/ml and pre-treated with carbon nanospheres at different concentrations (0-250 μg/ml) in phosphate buffer saline (PBS) for 24 hours at 37 °C in humidified 5 % CO_2 atmosphere. At the termination of culture, cells were rinsed with 1X PBS and 20 μL of MTT solution (5 mg/ml) was added to each well. The cells were cultured for another 4 hours. Then, 100 μL of DMSO was added to each well to dissolve formazan crystals and left at room temperature for 1 hour. The optical density (OD) was measured at 570 nm by a microplate reader (Infinite M200 Nanoquant, Tecan). The dispersion medium for the CNSs

was used as control in each cell for the entire study. Cell viability was estimated according to the stated equation:

$$\text{Viability (\%)} = [\, (A_{Sample} - A_{Blank}) / (A_{Untreated} - A_{Blank}) \,] \times 100$$
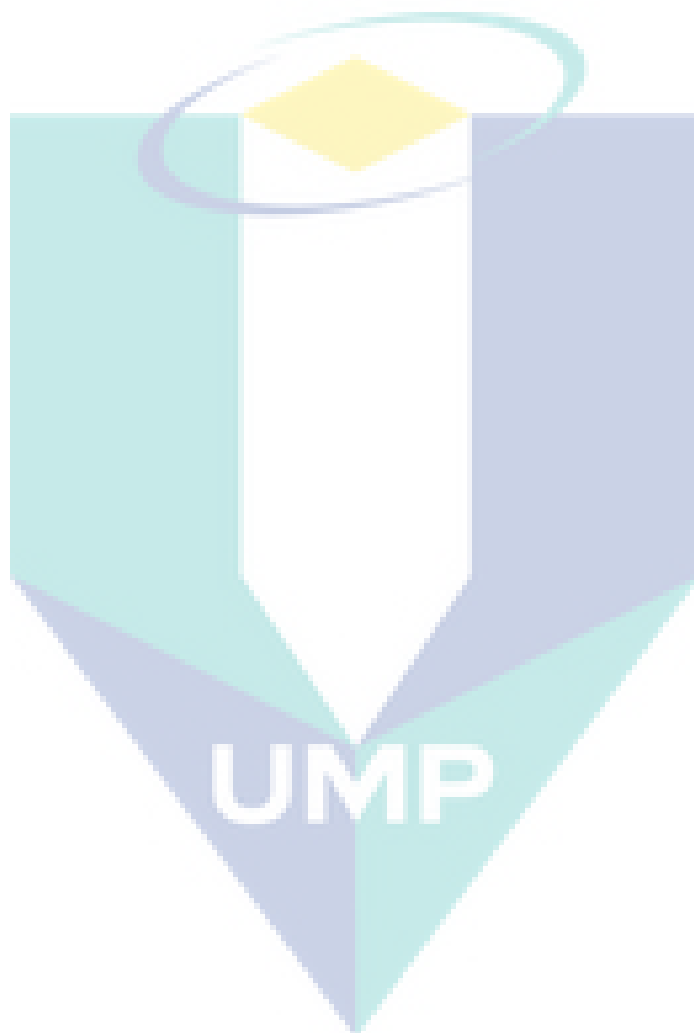
CHAPTER 4

RESULTS AND DISCUSSIONS

4.1   CHARACTERIZATIONS OF BIO WASTE

4.1.1   Oil palm leaves (OPL)

Thermogravimetric Analysis (Figure 4.1) was used to determine the temperature needed to start the pyrolysis and from the burning curve, one can see that OPL is completely burned around ~600 °C. From that value, the temperature used varies from 500 °C (which is just finished burning), 600 °C (completely finished burning) and 700 °C (much above the temperature where burning finished) to observe the carbonization effect to the raw material. At around 300 °C, OPL started losing its weight (around 95 %) and entire procedure is completed at around 600°C as shown where almost 85 % OPL is burnt completely
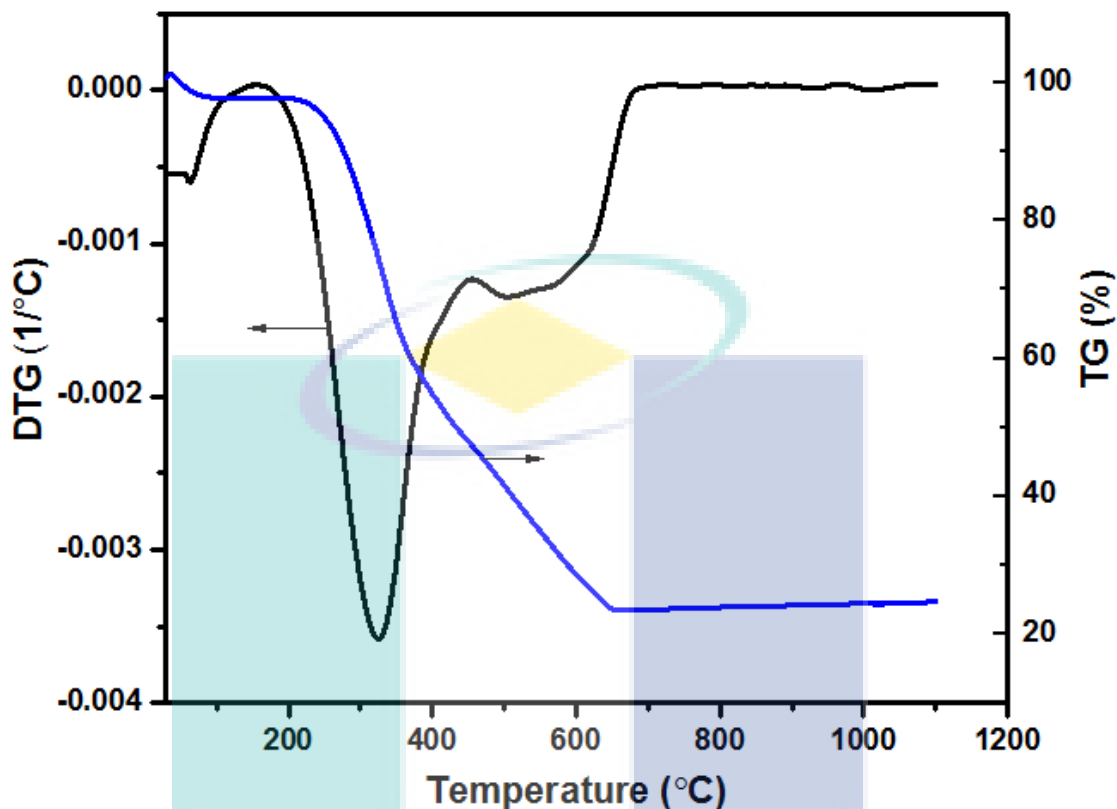
Figure 4.1: Thermogravimetric Analysis curve for the OPL.

The usage of OPL as a precursor is due to the silica content found where it acts as a template for fabrication of carbon nanospheres (Roslan et al., 2014). The silica template in the precursor has a porous nature that is finally transferred into the shape of nanomaterial produced during the carbonization process (Kumar et al., 2014). By saying that, the analyses have been done on the raw material of OPL to confirm the presence of silica content. The FESEM-EDX has been done to measure the structure and the percentage of silica in OPL. The FESEM images show the rigid surface structure of OPL at the 100 μm scales as shown in Figure 4.2 (a). At the scale of 10 000 μm, it shows the images of OPL cell wall (Figure 4.2 (c) and the secondary cell wall was observed as shown in Figure 4.2 (b). In Figure 4.2 (d), the depth images of the OPL cell wall was viewed at 800 nm scale.

From the detection area in Figure 4.2 (d), the energy dispersive X-ray (EDX) of the OPL was measured to identify the element content in its cell wall (Figure 4.2 (e)).

Element	Weight (%)	Atomic (%)
C K	49.11	59.47
O K	36.31	33.01
Na K	0.34	0.22
Mg K	0.14	0.08
Al K	0.18	0.09
Si K	13.30	6.89
K K	0.25	0.09
Ca K	0.38	0.14
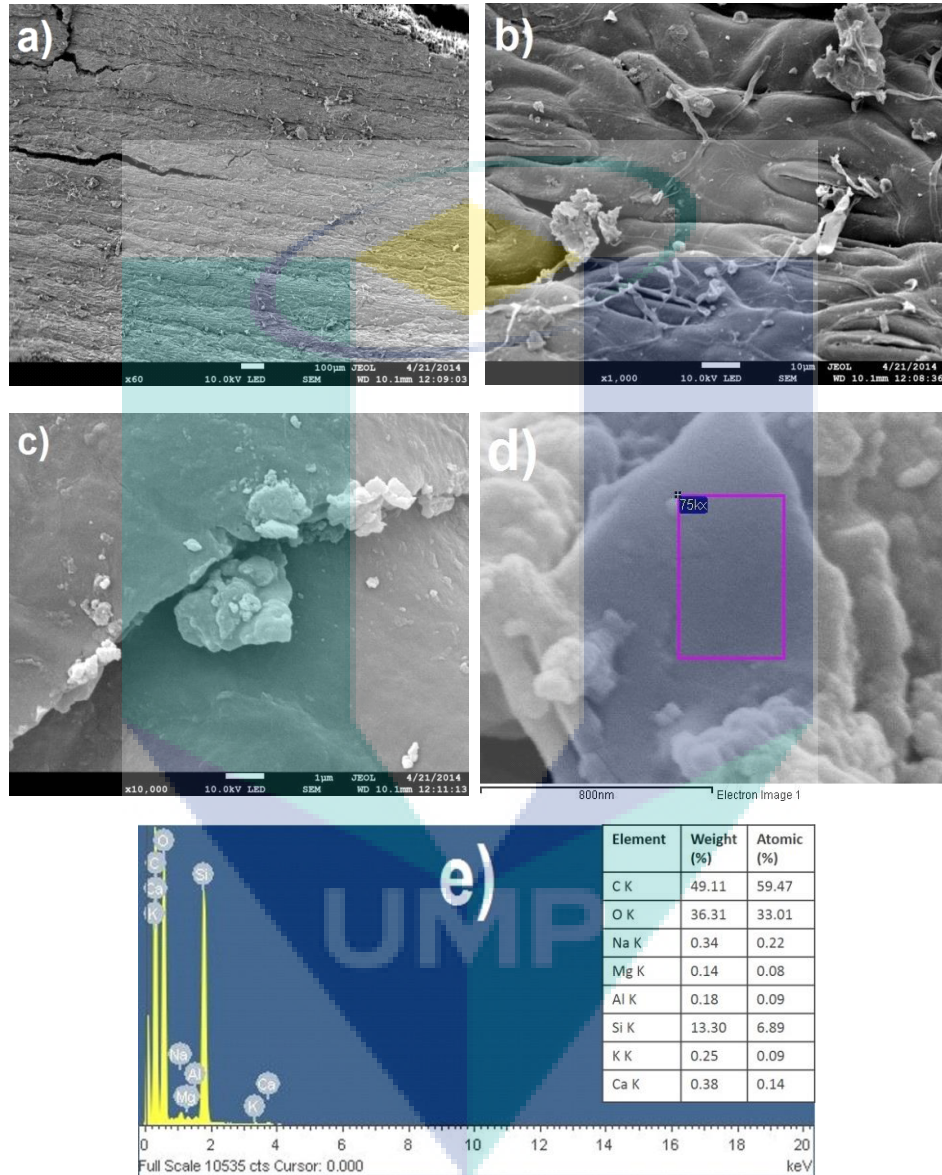
Figure 4.2: The Microscopic (FESEM) images of OPL (a) surface structure of OPL at 100 μm scale, (b) OPL cell wall at 10 100 μm scale, (c) secondary wall layer of OPL at 1 100 μm scale, (d) cell wall at 800 nm scale and (e) energy dispersive X-ray (EDX) analysis of different elements present in the cell wall of OPL.

Besides that, the FTIR measurements were used to observe the functional group presents in the raw material of OPL (Figure 4.3). From the figure, it shows the presence of Si-H bond, which belongs to the wavelength of 655 cm^{-1} where it represented the stretching of mono-hydrogen bond (Knights et al., 1979 and Gao et al., 2012). At wavelength 1409 cm^{-1}, it shows the presence of Si-CH$_3$ that again confirmed the Si content in the raw material. At 1050 cm^{-1}, there are Si-O vibrations caused by the oxygen atom motion in the Si-O-Si plane. This is parallel with the line of two adjacent silicon atoms (Galeener, 1979; Galeener and Sen, 1978 and Gao et al., 2012).
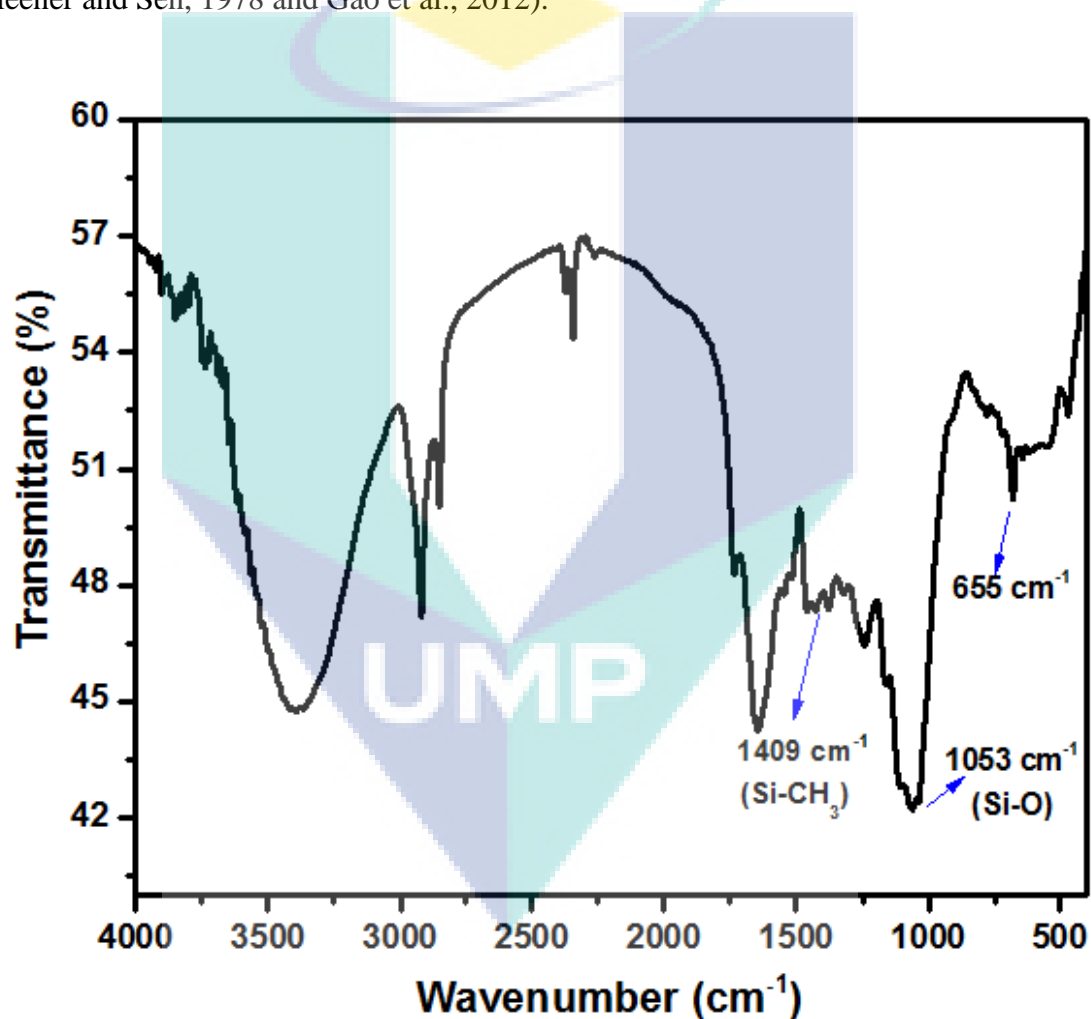

Figure 4.3: FTIR spectrum for OPL.

The XRD analysis is also used to confirm the presence of silica in the raw material of OPL. Figure 4.4 below shows the result obtained from the XRD analysis where it shows three major peaks that were present in the XRD pattern. First peak presents at $2\theta = 21.35°$ with interlayer d-spacing equals to 4.159 A° that corresponds to plane 110. The high intensity and sharp peak observed at $2\theta = 26.867°$ with d-spacing 3.3157 A° represents the 020 planes. At $2\theta = 67.72°$, 240 planes were present with d-spacing equals to 1.3825 A°. The sharp peaks present indicate the high crystallinity of the material. These three different peaks are related to silicon dioxide (SiO_2) appear in the raw material with different crystalline phase of 110, 020 and 240, according to ICDD 10821555 (Kumar et al., 2014 and Saceda et al., 2011). The crystalline behavior in the XRD originated from the silica content in OPL itself. As known, silica usually comes with crystalline phase. The presence of silica in OPL due to the accumulation of silica particles in epidermal tissue or cell wall of leaves where transpiration induces a loss of water, which in turn increases the concentration of silica (Currie and Perry, 2007 and Blackman, 1968). The occurrence of Si within the plant is a result of its uptake, in the form of soluble $Si(OH)_4$ or $Si(OH)_3O^-$, from the soil and its controlled polymerization at a final location (Mitani and Ma, 2005 and Prychid et al., 2003). The individual silica bodies each consist of about 100,000 silica rods and the silica particles in each rod have a diameter of 1-2 nm (Davanandan, 1983).
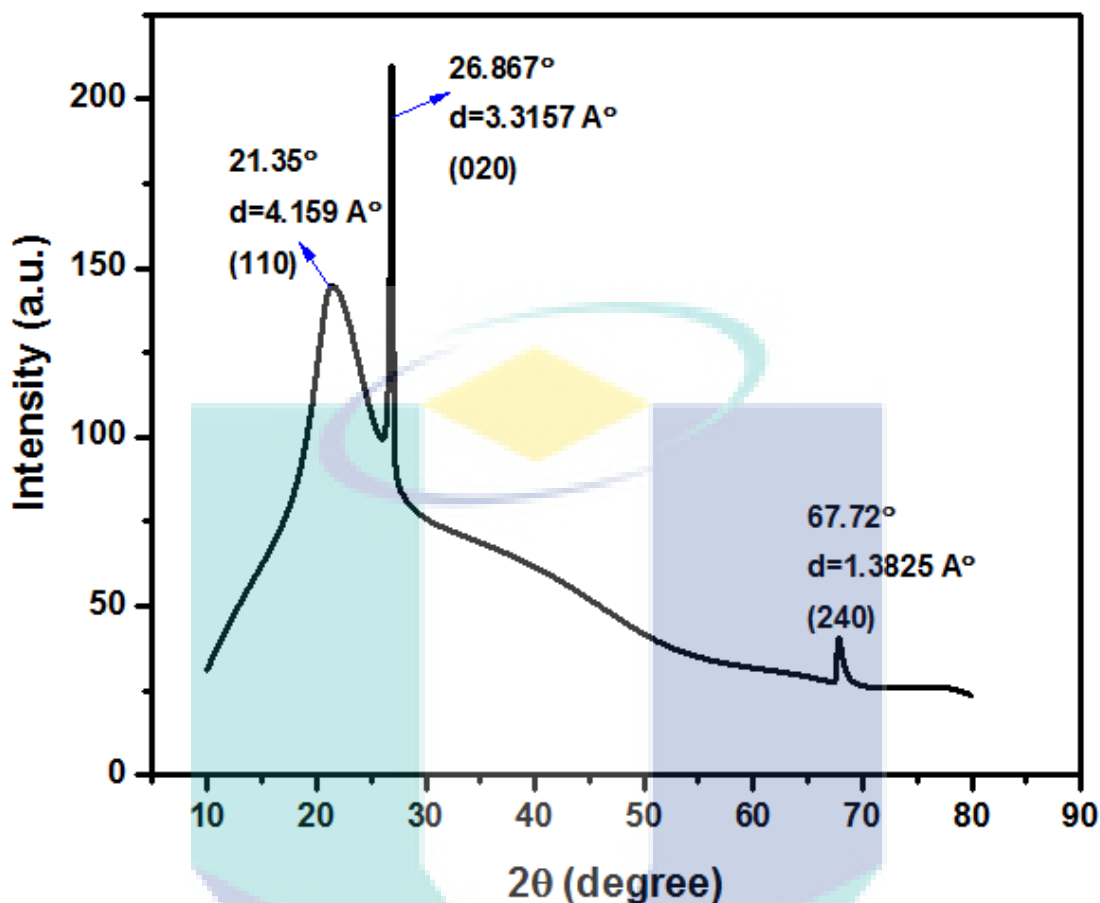
Figure 4.4: The XRD result for the raw material, OPL.

4.1.2   Sago Hampas

On the other hand, sago hampas is another kind of bio waste produced in South East Asia that need to be taken care since every year, these kind of waste materials are accumulating in the environment and improper burning of these materials can cause asthma related problems among human beings. Here, we attempted to use sago hampas bio waste as a precursor and characterized it using several techniques to elucidate their potentiality in the field of cell imaging and other related applications. TG-DTG curves of the precursor sago hampas revealed that, the degradation takes place in a single step. The mass degradation starts at 270 °C and major degradation takes place around 360 °C (Figure 4.5).

The curve shows complete burning at ~900 °C and from this point, the pyrolysis temperature used are 400 °C (after major degradation complete) and 600 °C (middle temperature just before complete burning). Based on this, a green method was applied for the synthesis of CNSs by a convenient and harmless catalyst free pyrolysis technique.
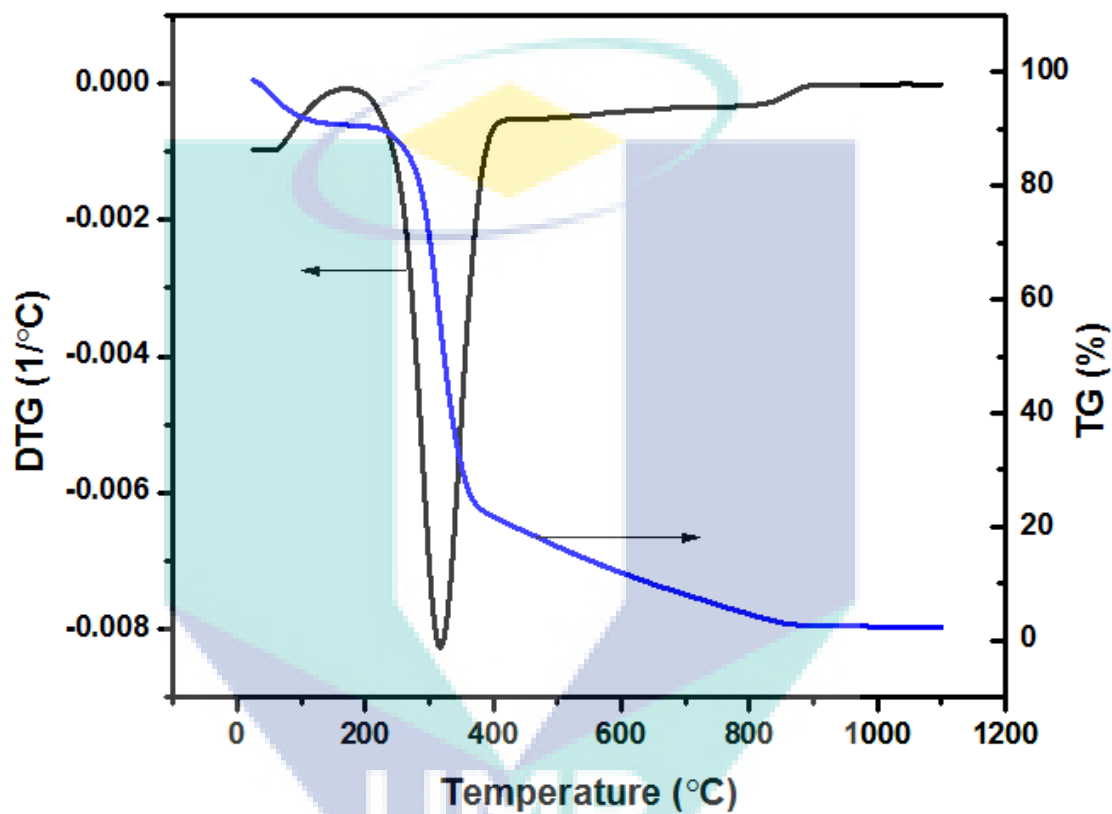
Figure 4.5: TG-DTG of raw sago hampas.

FESEM observation combined with energy dispersive X-ray (EDX) was carried out for the precursor sago hampas to know the original shape and the mass ratios of carbon along with other elements. Figure 4.6 (a) shows the FESEM images of raw sago hampas where the EDX spectrum was taken from the detection area in this figure. The major content of the precursor based on atomic percentage was carbon with 58.85 % of it and oxygen with 40.89 % as shown in Figure 4.6 (b). Very less content of silicone and calcium

were also observed. This fibrous shape and the coarse porous nature of the sago hampas can act as a base/template for the formation of CNSs without any catalysts and templates.

Element	Weight%	Atomic%
C	51.62	58.85
O	47.77	40.89
Si	0.33	0.16
Ca	0.29	0.10
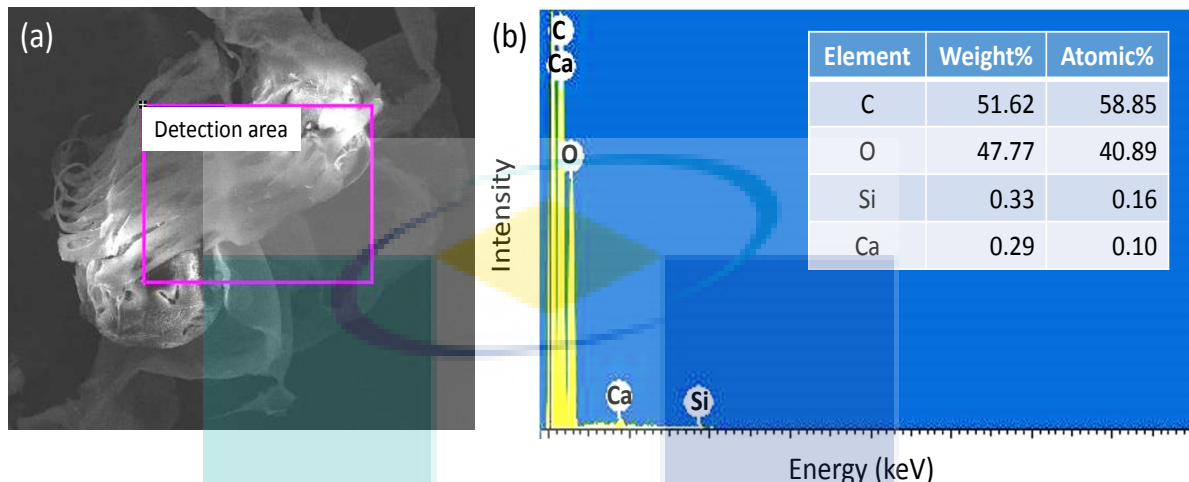
Figure 4.6: (a) FESEM images of sago hampas; (b) EDX spectrum taken from the detection area from Figure (a).

FT-IR study is helpful in ascertaining the absorption bands associated with lignocelluloses such as cellulose, hemicelluloses and lignin in sago hampas (Figure 4.7). The characteristic of hemicelluloses band observed around 1159 cm^{-1} may be ascribed to glycosidic linkage C-O-C and cellulose absorption bands are observed at 1425 cm^{-1}, respectively (Sim et al., 2012 and Cheng et al., 2006). A very weak shoulder band was observed around 1510 cm^{-1}, which is very difficult to be identified as a peak, due to an aromatic characteristic of lignin. This indicates the presence of low lignin content in sago hampas. The strong stretching vibration band observed around 1640 cm^{-1} can be assigned to carboxyl group, (C=O) which gives an evidence for the high oxygen content of sago hampas (Sim et al., 2012 and Cheng et al., 2006). Along with this, the other numerous absorption bands observed in the region 2900 and 1500-900 cm^{-1} may be due to structural diversity of celluloses and hemicelluloses (Peng et al., 2009) including C-OH, C-H, C-C-O functional groups. The bands at 1159 cm^{-1} and 1032 cm^{-1} suggest the presence of arabinosyl residues and α-glucan of hemicelluloses (Kacurakova et al., 2000). Hence, the

glycosidic linkages and hydroxyl groups of celluloses and predominant ether bond of hemicelluloses and lignin as observed in this FTIR spectrum of sago hampas are in accordance with the previous literature suggesting lignocellulosic compositions of about 64.4 % cellulose, 25.1 % hemicellulose and 10.5 % lignin (Kuroda et al., 2001).
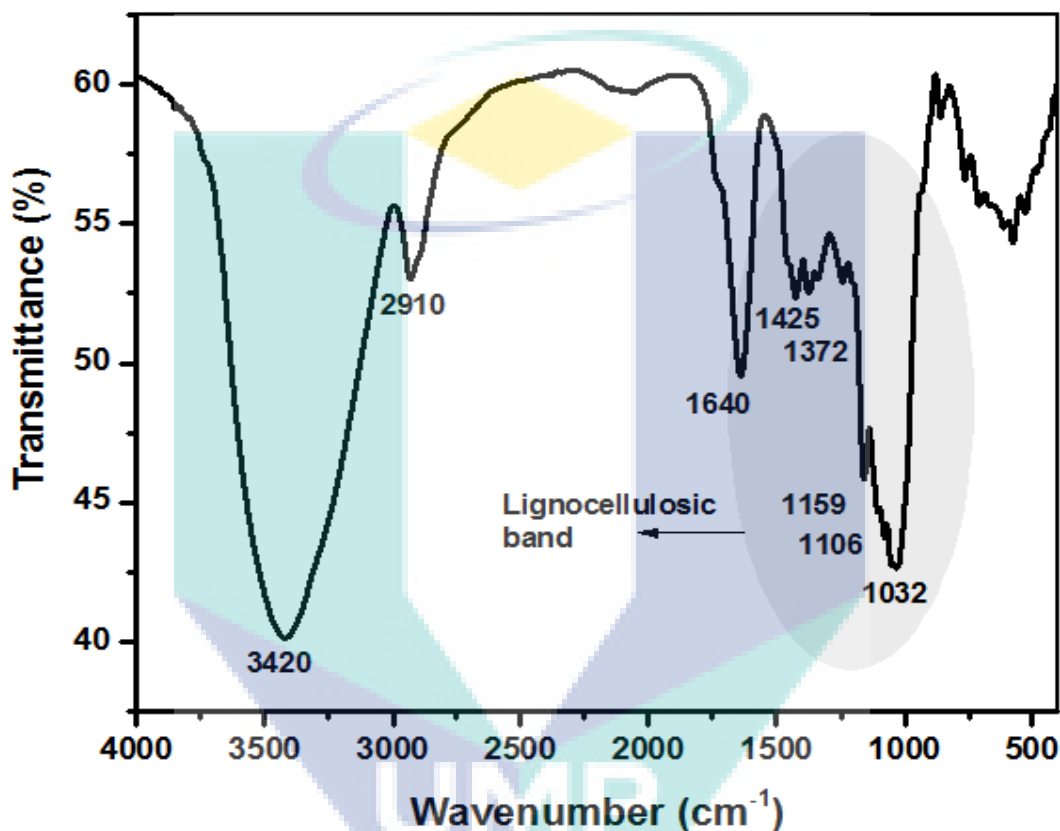
Figure 4.7: FTIR spectrum of sago hampas.

In the wide-angle XRD pattern of the sago hampas, two peaks were observed. The first peak is at $2\theta=17.8°$ ($d= 4.02$ Å) and followed by the second at $2\theta=22.3°$ ($d= 5.00$ Å), which corresponded to 001 and 011, respectively (Figure 4.8) (Nishiyama et al., 2003), indicating microcrystalline nature of the celluloses (Mathew et al., 2005). Thus, the above characterization data highlight high content of carbon and oxygen in sago hampas and that has contributed to the formation of CNSs.
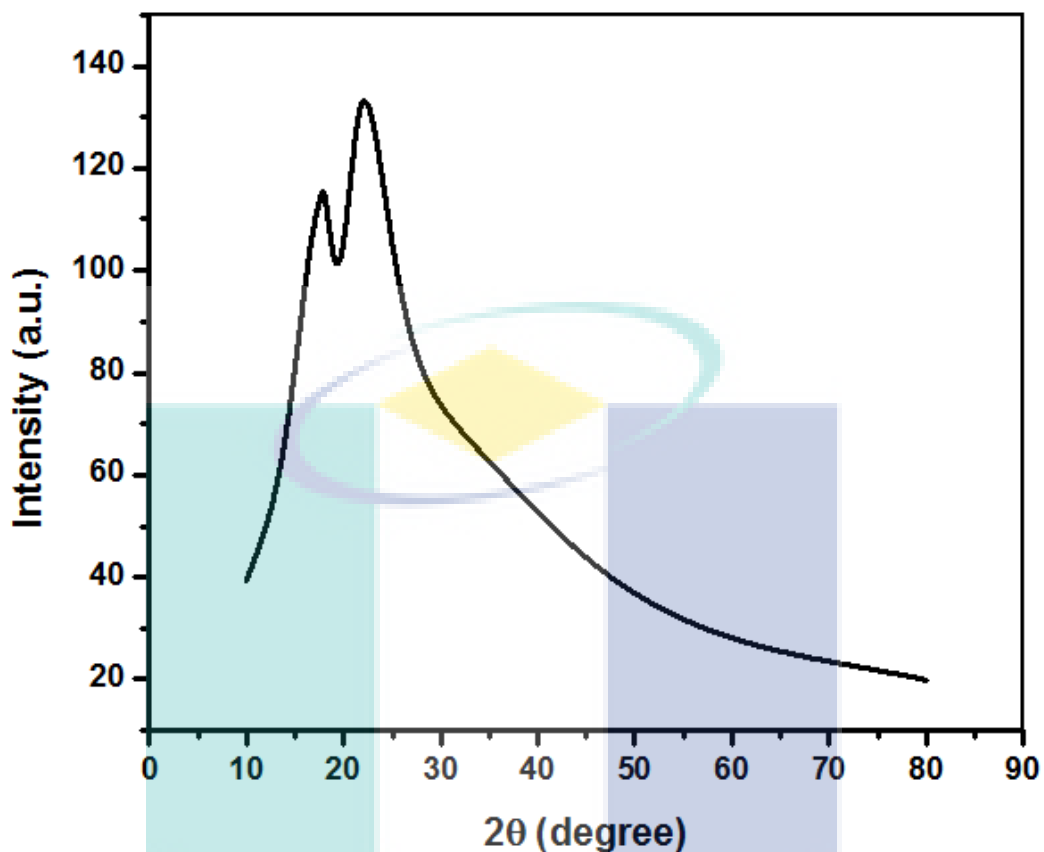
Figure 4.8: XRD pattern of raw sago hampas.

4.2   PYROLYSIS OF CARBON NANOSPHERES (CNSs)

The sample of oil palm leaves (OPL) and sago hampas were used to synthesize porous carbon nanospheres (CNSs) using a pyrolysis step by thermal treatment. The OPL underwent pyrolysis with three different temperatures, which are 500 °C, 600 °C and 700 °C. As the pyrolysis temperature varies, the heating rate, gas flow and holding time were kept constant. The same experimental set up and conditions were done for raw sago hampas. It was treated at two different temperatures, which is 400°C and 600°C where it depends on the TGA curve obtained. Different type of biomass precursor has different decomposition state.

4.3   CHARACTERIZATION OF CARBON NANOSPHERES (CNSs) PREPARED USING OIL PALM LEAVES (OPL)

4.3.1   Fourier Transform Infrared Spectroscopy

CNSs were used for FTIR measurement to observe the functional groups present in the material. Figure 4.9 shows the FTIR analysis of the raw material of oil palm leaves followed by the pyrolyzed CNSs that already undergone the carbonization by pyrolysis with different final temperatures. The FTIR spectrum of the samples is different from the raw material as some of the functional group disappeared after carbonization process due to the thermal degradation effect during carbonization that caused the destruction in some of intermolecular bonding (Salman, 2013). The peak at ⁓3500 cm^{-1} represents the –OH groups where the intensity decreasing as the pyrolysis temperature increases. This phenomenon happened due to the water loss from the raw material that is also known as dehydration (Yuliansyah and Hirajima, 2012).

The peak at ⁓2900 cm^{-1} contributes to aliphatic CH_n disappearance as the raw material undergone carbonization process where only in raw material, the strong peak is present. It indicates that it is broken down by several long aliphatic chains. The peak 1700-1740 cm^{-1} represents the carbonyl (C=O) stretching vibrations that disappeared when it undergoes pyrolysis (Yuliansyah and Hirajima, 2012). The peak at 1695-1630 cm^{-1} and 1500-1450 cm^{-1} represents the C=C stretching where the peak slowly disappeared as the temperature increased (Lai and Idris, 2013). The C-H bending peaks showed in the range of 1470-1350cm^{-1} represents the alkane group (Hooi et al., 2009). The peak at ⁓1050 cm^{-1} refers to glycosidic bond that represented the cellulose where it weakens in all samples. It seems that the cellulose was degraded from the raw material (Yuliansyah and Hirajima, 2012). C-H deformation in cellulose occurs at range 915-650 cm^{-1} where the peaks shifted as the temperature increase (Lai and Idris, 2013 and Hooi et al., 2009).
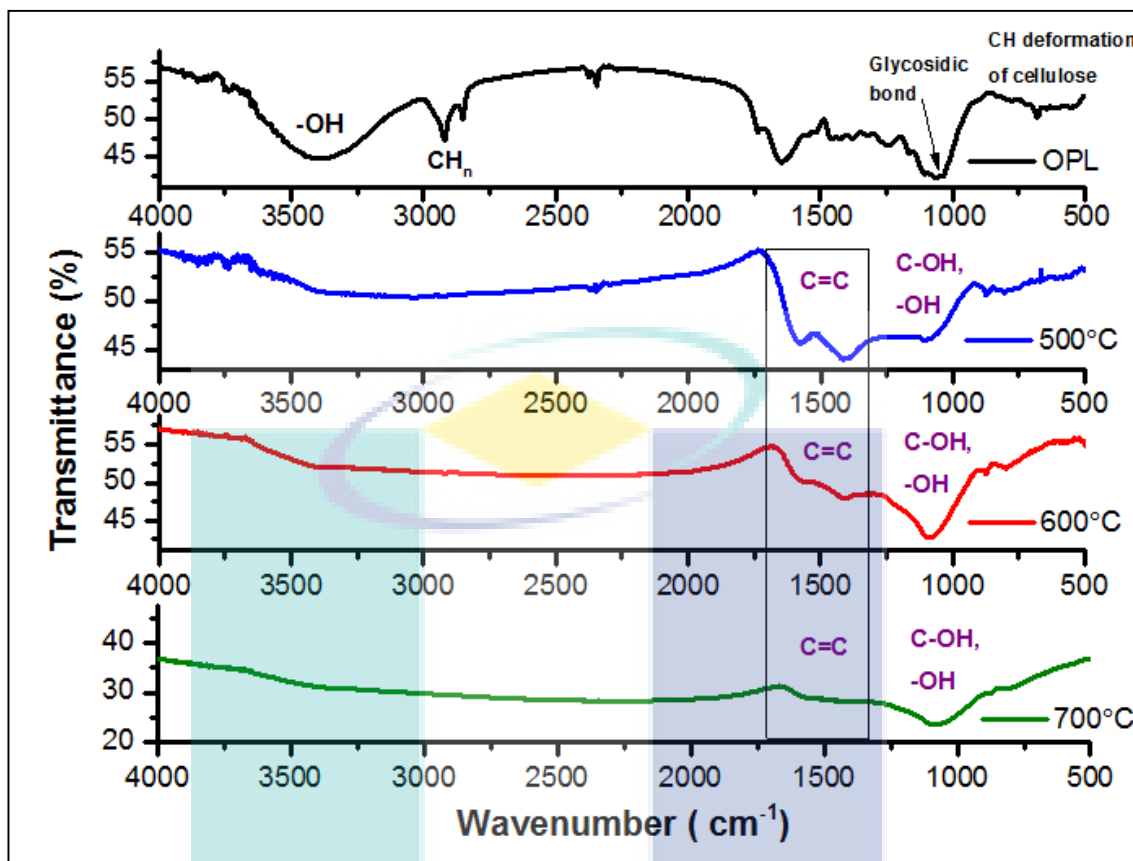
Figure 4.9: The FTIR spectrum for the OPL and CNSs with different pyrolysis temperature.

The peaks in the range of 1340-1700 cm^{-1} represents the C=C of graphene materials. The C-OH stretching peaks and OH bending vibrations were shown at 1118 cm^{-1} while 2921 and 2852 cm^{-1} peaks represents C-H stretching vibrations. At 1580 and 1636 cm^{-1}, the peaks appear due to the stretching vibrations from carboxylic group. These peaks show that there are many residues including hydroxyl and carboxyl groups and it is an important key to spherical formation process (Krishnamurthy and Namitha, 2013).

4.3.2   X-Ray Diffraction (XRD)

The X-ray diffraction was measured to observe the presence of crystalline and amorphous carbon from the CNSs. Figure 4.10 below shows the XRD curve for each sample with different temperature. When CNSs are pyrolyzed at 500°C, the peak observed is at $2\theta = 26.65°$ with 002 planes of graphite (ICDD 10713739) and an interlayer d-spacing 3.3418 A°. This peak existed from the low curvature graphite face found in graphite. In addition, the previously reported literature confirmed that the peak at 26.65° represent the 002 planes, which belongs to the phase of graphite (Im et al., 2014 and Li et al., 2013).

The 600°C pyrolyzed CNSs show two close peaks, which at $2\theta=26.56°$ and 26.85°, the latter being close to reflection for 002 planes of graphite. At $2\theta=44.67°$, the 101 phases of diamond syn. (ICDD 10750410) appears and shows the presence of 111 phases that belongs to graphite (Wang et al., 2014 and Hossain and Islam, 2013). This kind of peak does not appear at 500 °C pyrolyzed CNSs that may due to the improper carbonization of precursor. The phase intensity of 002 planes shows the difference between sample of 500 °C and 600 °C where the 500 °C sample has lower peak intensity due to amorphous carbon content and 600 °C have a higher intensity of peak because of the presence of graphite carbon (Chen et al., 2004). The sharpness of peaks represents the presence of crystalline carbon phase in the porous carbon nanospheres (Krishnamurthy and Namitha, 2013).
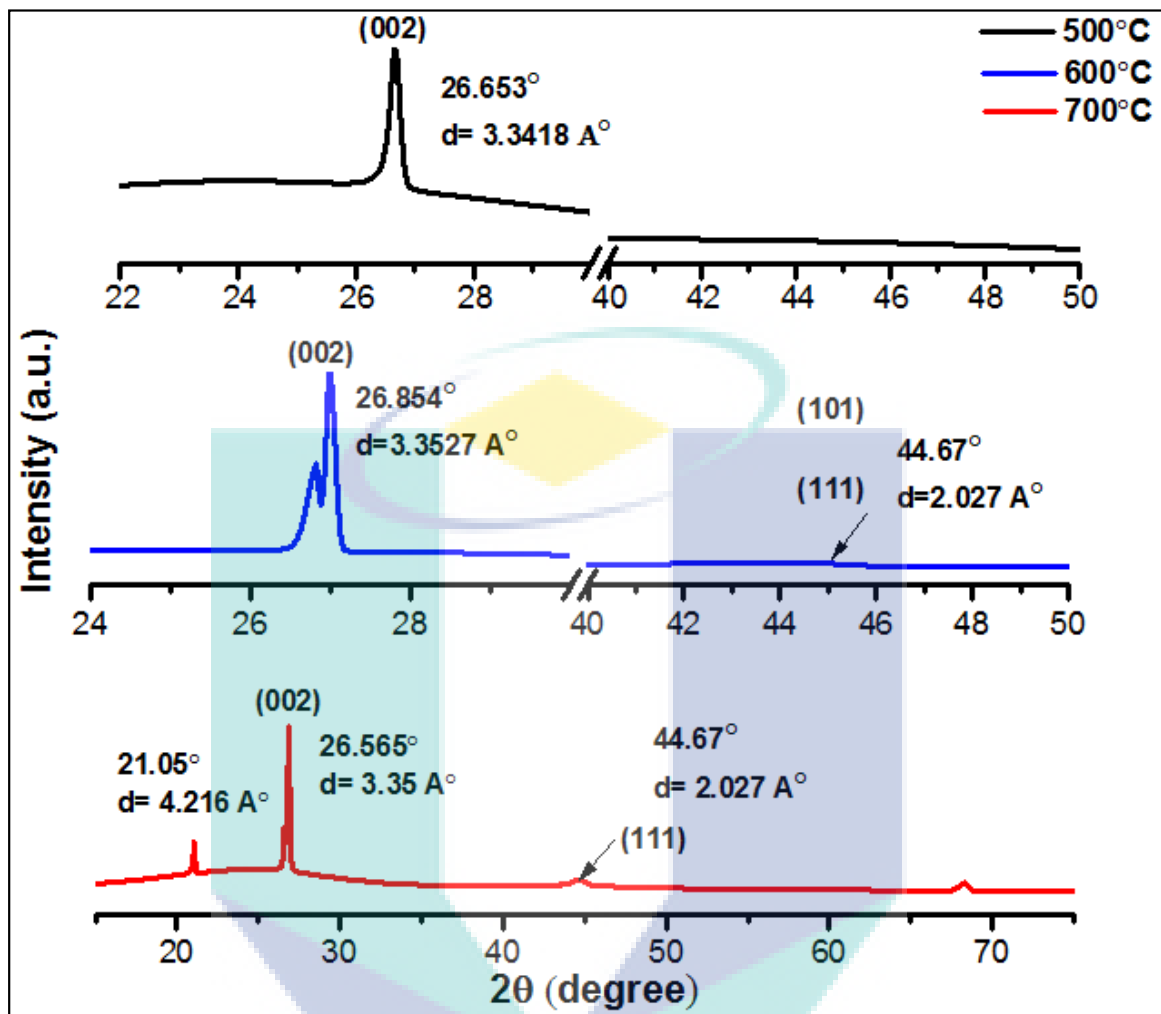
Figure 4.10: The X-ray diffraction peaks for CNSs pyrolyzed at 500 °C, 600 °C and 700 °C.

The 700 °C CNSs have peak at $2\theta= 26.565°$ with d-spacing of 3.35 A° that was belong to graphite phase 002. Another peak also appears at $2\theta= 44.67$ with d-spacing 2.027 A° representing graphite phase (111) (Hossain and Islam, 2013). The peak at 68.30° represents α-aluminum with d-spacing 1.372 A°. There were also peaks that show the presence of Fe at $2\theta= 21.05°$ with d-spacing of 4.216 A°. So, the pyrolyzed sample at 700 °C shows the presence of the various compounds where the major content come from Fe and carbon.

4.3.3   Thermogravimetric Analysis (TGA)

Thermogravimetric Analysis (TGA) was measured for carbon nanospheres to determine the thermal stability of the CNSs. The measurement was carried out in the nitrogen atmosphere.
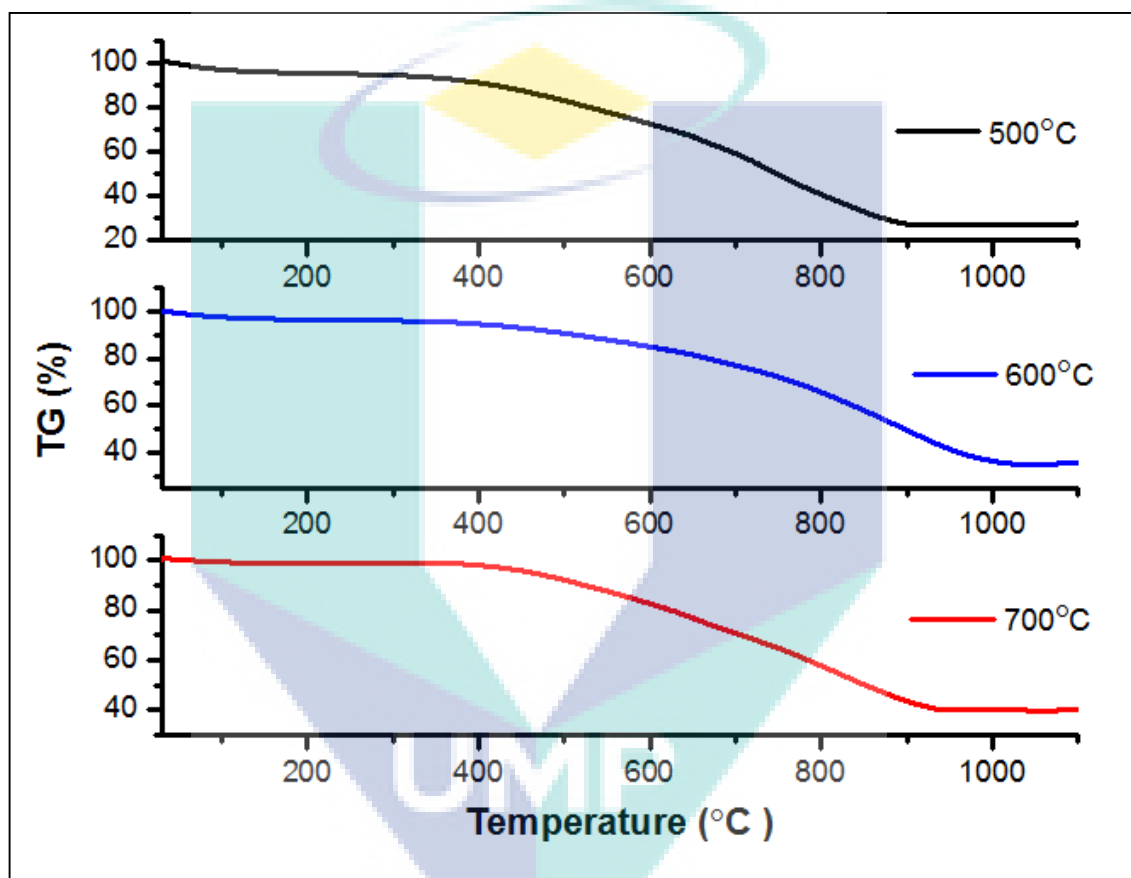
Figure 4.11: The TGA curve for CNSs pyrolyzed at different temperatures.

Figure 4.11 above shows the TGA curve that explains the weight loss with respect to the temperature for all carbon nanospheres with different pyrolysis temperature. There is a slight weight loss for all pyrolyzed samples from 30 to 120 °C, which might be due to the water loss from the sample. The major decomposition for CNSs 500 °C starts at 300 °C until 900 °C where the CNSs 600 °C pyrolyzed samples start at 400 °C until 1100 °C. For

CNSs 700 °C pyrolyzed sample, it starts at 450 °C until 950 °C. It shows that the sample pyrolyzed at 600°C have higher thermal stability compared to the other two samples. Weight loss of pyrolyzed sample at 500 °C is 75 %, followed by 600 °C at 65 % and 700 °C at 60 %.

4.3.4   Brunauer-Emmett-Teller (BET)

The Brunauer-Emmett-Teller (BET) was measured to determine the material surface area, pore volume and size. Figure 4.12 shows the nitrogen adsorption and desorption curve of CNSs at different temperature. Table 4.1 shows the BET measurements for all obtained CNSs at different temperature. The 600 °C of CNSs have a BET surface area (S_{BET}) of 52 m^2/g with t-plot micropore surface area (S_{t-plot}) of 39 m^2/g. These two values indicated that 600 °C CNSs is having a high micropore ratio equals to 75 % (S_{t-plot}/S_{BET}). The reported value of micropore percentage of conventional activated and in template carbon was much lower from these values (Wang et al., 2013 and Lin et al., 2013).

The 500 °C CNSs have a BET surface area (S_{BET}) of 32 m^2/g with t-plot micropore surface area (S_{t-plot}) value is at 15 m^2/g that contributed to the micropore percentage of 47 % while the 700 °C CNSs have 39 m^2/g BET surface area and 22 m^2/g of t-plot micropore values which give 56.4 % of micropore percentage. Therefore, as the pyrolysis temperature increased, the surface area also increased together with micropore percentage but limited to 600 °C since the 700 °C CNSs values dropped. This phenomenon happened due to the aggregation of CNSs where it is intact and exhibit smooth surfaces thus the surface area was drastically decreased compared to the earlier reports on carbon nanospheres (Nieto-Marquez et al., 2011).

Table 4.1: BET measurement for CNSs.

CNSs	BET surface area (S_{BET}) (m^2/g)	t-plot micropore (S_{t-plot}) (m^2/g)	Micropore ratio (S_{t-plot}/ S_{BET}) (%)	Pore diameter (BJH method)
500 °C	32	15	~47	(2.07-2.1 nm)
600 °C	52	39	75	(1.97 nm)
700 °C	39	22	56.4	(1.98 nm)
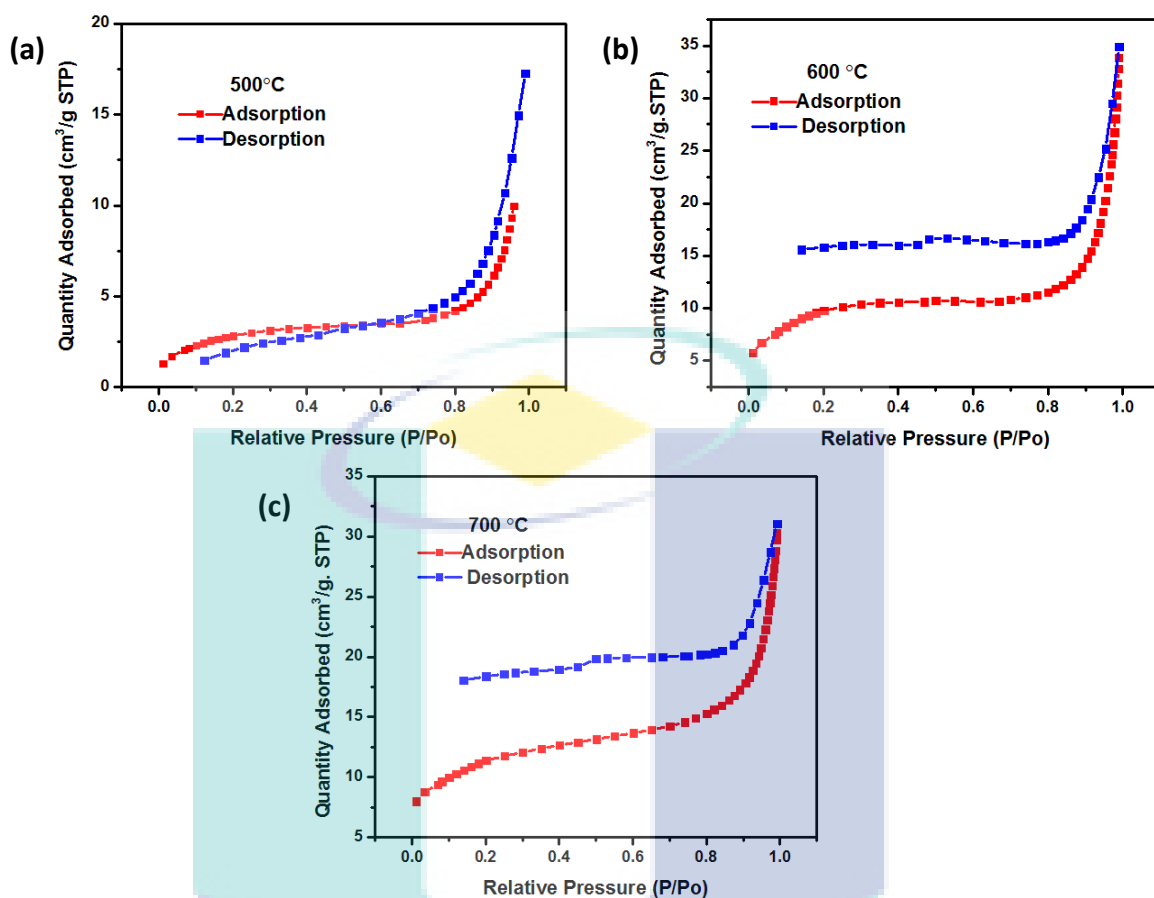
Figure 4.12: Nitrogen adsorption and desorption isotherm of CNSs of (a) 500 °C, (b) 600 °C and (c) 700 °C.

The pore diameter of CNSs (Figure 4.13) also has been measured using BET. The pore diameter for 500 °C CNSs is around 2.07-2.10 nm and decreased to 1.97 nm for 600 °C CNSs followed by slight increases in pore diameter for 700 °C CNSs which gives 1.98 nm. All CNSs with different pyrolysis temperature give quite similar pore diameter values, which are around 1.9-2.0 nm.
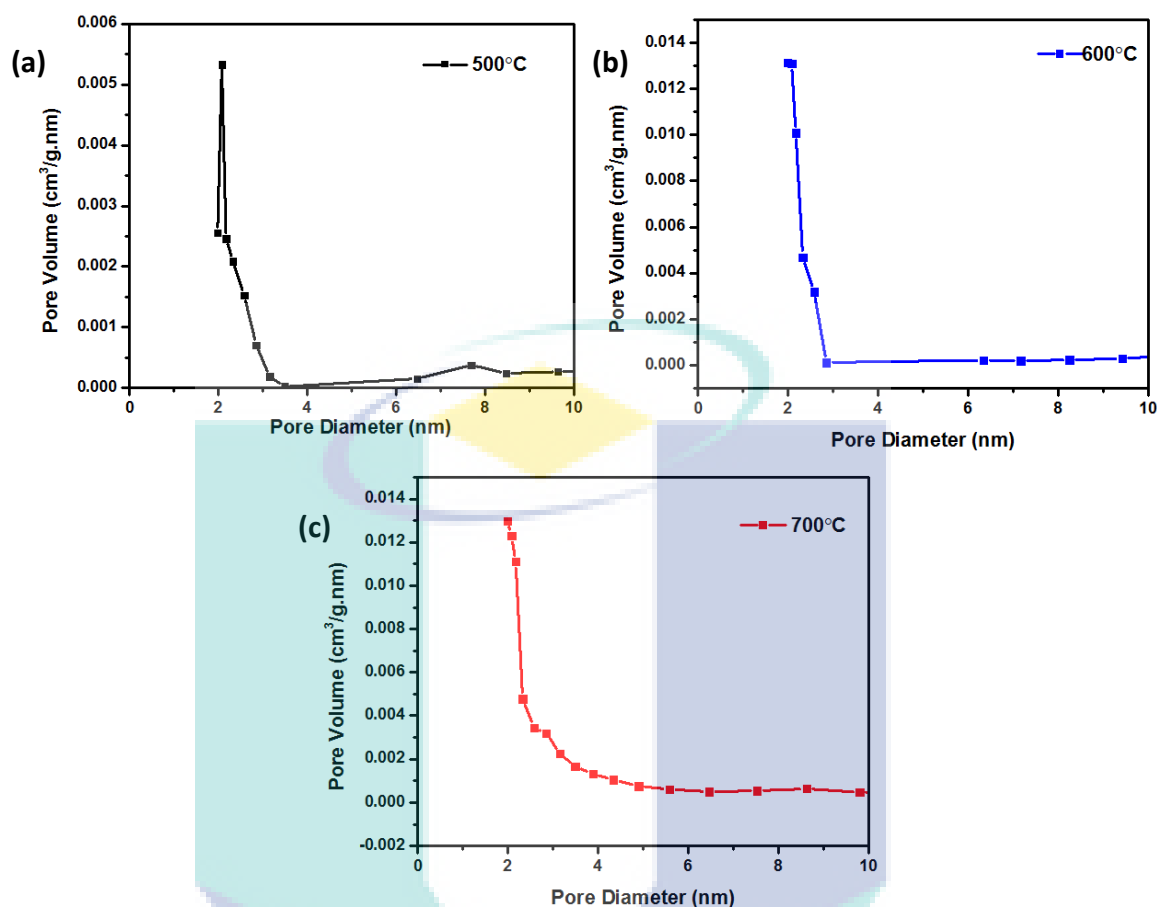
Figure 4.13: Pore diameter for CNSs at (a) 500 °C, (b) 600 °C and (c) 700 °C.

4.3.5 Raman Spectroscopy

The graphite materials is proved by the G band appearing in between 1580-1590 cm^{-1} that is also known as a doubly degenerate phonon mode associated with E_{2g} symmetry at the BZ centre and is related to sp^2- bonded carbon atom vibrations in a two dimensional hexagonal lattice. It is resulted from the C=C stretching modes that belongs to the typical graphite (Wang et al., 2008; Krishnamurthy and Namitha, 2013; Li, Y. et al., 2009; Li, G. et al., 2008; Mohan and Manoj, 2012 and Xu et al., 2010). The D band in between 1350-1361 cm^{-1} is known as disorder-induced character of graphite attributed with A_{1g} mode. It is associated due to the presence of structural defects and disorders of carbon materials (Wang et al., 2008; Krishnamurthy and Namitha, 2013; Li, Y. et al., 2009; Li, G. et al., 2008;

Mohan and Manoj, 2012 and Xu et al., 2010). The Raman band between 2500-2800 cm^{-1} corresponds to the overtone of D band known as G' (Im et al., 2014; Lespade et al., 1982; Cancado et al., 2004 and Tuinstra and Koenig, 1970).

Figure 4.14 shows the G band at 1589 cm^{-1}, 1588 cm^{-1}, and 1589 cm^{-1} for 500 °C, 600 °C and 700 °C CNSs respectively. Besides that, D band also present in Raman spectra at 1360 cm^{-1} and 1358 cm^{-1} for 600 °C and 500 °C CNSs sample respectively and 1356 cm^{-1} for 700 °C CNSs that shows it possess the induced disordered. The shape of D and G peaks depend on the crystallite size of the sample. As the crystallites become larger, the peak will become narrower. It will move to the high frequency and G peak intensity will automatically increases compared to D peak (Mohan and Manoj, 2012).

The I_D/I_G is the intensity ratio of D and G bands that were used to determine the quantity of defects in graphite materials (Walker et al., 1954 and Lou et al., 2014). The higher the ratio, the higher the degree of graphite disorder (Li, G. et al., 2008) will be. There is no much difference of I_D/I_G ratios of the CNSs. The I_D/I_G is decreased from 0.73 for 600 °C to 0.69 for 500 °C, and it increased to 0.78 for 700 °C. For both pyrolysis temperatures of 500 °C and 600 °C, G' band also appeared at the band around 2800 cm^{-1} but for 700 °C, there was only very low peak for G' band. From the lower intensity ratio of I_D/I_G, it shows that the prepared carbon nanospheres have a high percentage of crystalline graphite.

.
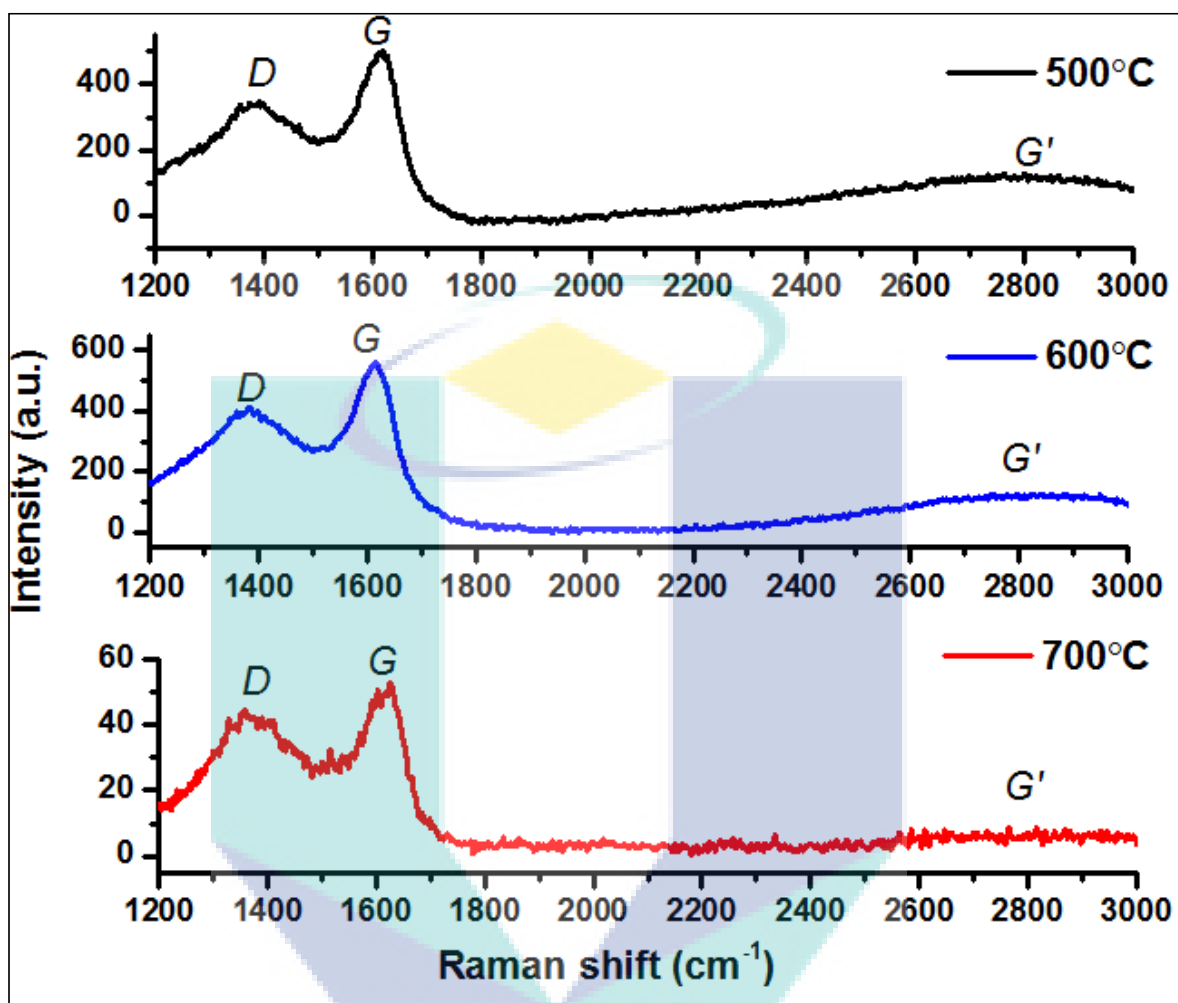
Figure 4.14: The Raman spectroscopy for CNSs at pyrolyzed temperature of 500 °C, 600 °C and 700 °C.

4.3.6 FESEM-EDX

FESEM measurement (Figure 4.15) has been done to observe the images that show the average diameter and shape appeared for the nanomaterial. Three samples with different pyrolysis temperature undergone the measurement where the 500 °C CNSs sample shows the average diameter of 20-40 nm (Figure 4.15 (a)) with 150 k magnification whereas the 600 °C CNSs sample shows the particles sizes around ~20 nm (Figure 4.15 (b)) and the

distribution of particles is also better than 500 °C CNSs sample. The 700 °C CNSs sample shows the ~20-22 nm particle size as shown in Figure 4.15 (c). The entire samples exhibit the sphere shape of particles and it was distributed uniformly. The particle sizes depend on the pyrolysis temperature and it shows that 600 °C was an ideal temperature to obtain the lowest particle size with uniform shape.
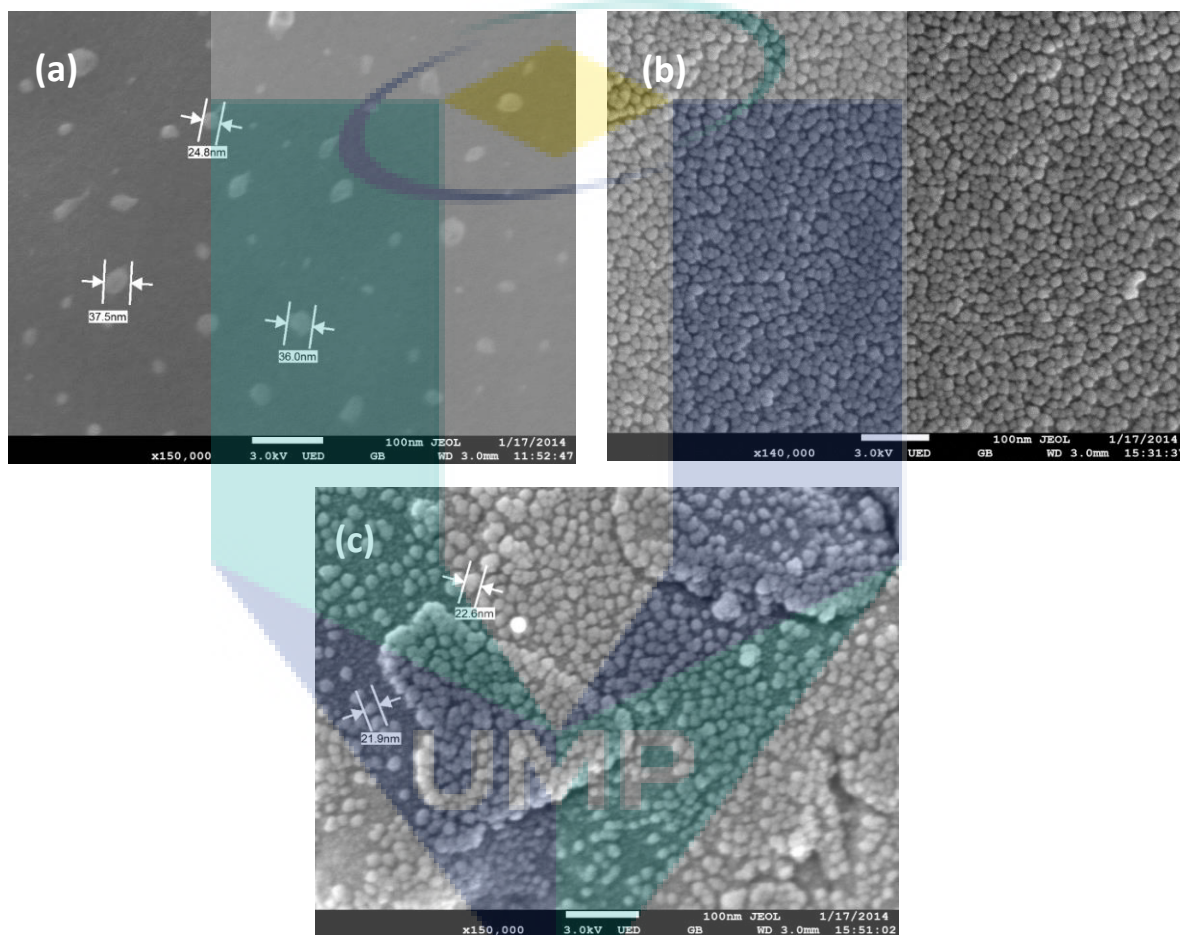
Figure 4.15: The FESEM images of CNSs pyrolyzed at (a) 500 °C, (b) 600 °C and (c) 700 °C.
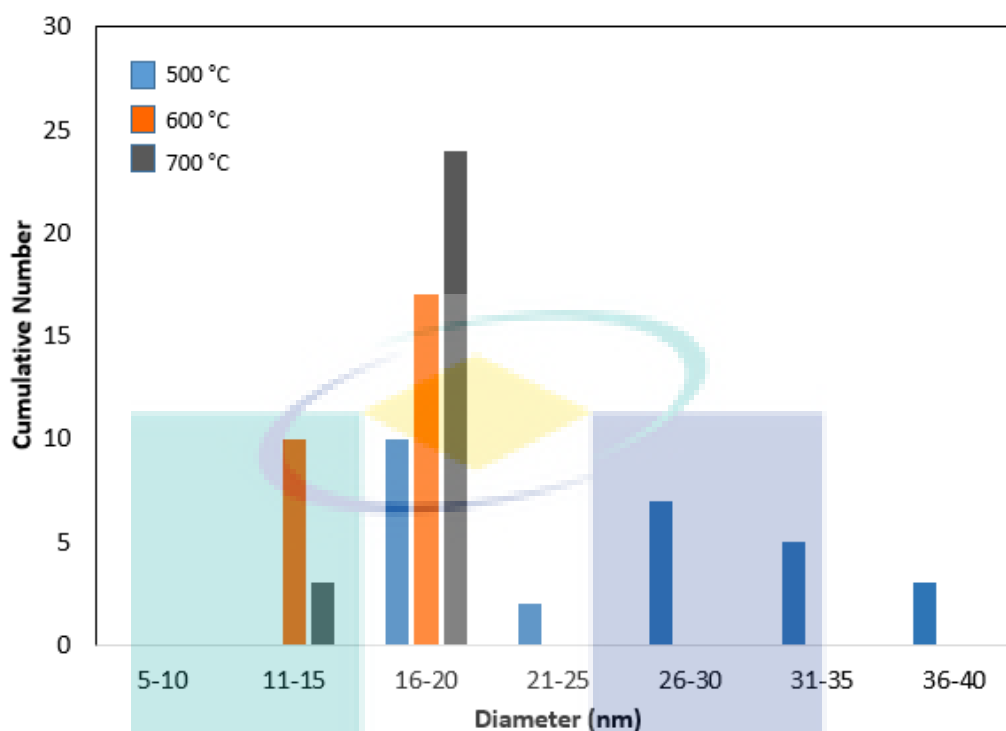
Figure 4.16: Particle distribution of FESEM images with CNSs.

The particle size distribution of FESEM images was shown in Figure 4.16. From the chart, the 500 °C pyrolyzed CNSs contains the particle sizes in the range of 16-40 nm whereas for the 600 °C, the CNSs sizes are in the range of 11-20 nm. It shows that the size of particles reduces as the pyrolysis temperature increases. On the other hand, the range of size for CNSs at 700 °C is mostly at 20 nm. The particle sizes of CNSs depend on the temperature used and 600 °C was preferable for obtaining the smallest particle size.

Table 4.2: The carbon percentage of CNSs for each temperature.

Pyrolysis temperature (°C)	Carbon percentage (%)	
	Weight	**Atomic**
500	71.40	80.74
600	82.73	87.90
700	28.08	44.87

Besides that, EDX analysis (Table 4.2) was also measured to determine the elemental content in the nanomaterial. It shows that the carbon content for 500 °C CNSs is ~78 % and for 600 °C CNSs is ~87 % whereas for 700 °C is ~44 %. So, the prepared materials have a good carbon percentage and it changed depending on the pyrolysis temperature. As higher the temperature get, the carbon content is also higher but when the optimum temperature was reached, higher temperature will not affect carbon percentage anymore since it might contain other elements as well.

4.3.7 Transmission Electron Microscopy (TEM)

The TEM images (Figure 4.17) for the carbon nanospheres pyrolyzed at different temperature were measured. The carbon nanospheres obtained at carbonization temperature of 500 °C have the average particle size of 80 nm (Figure 4.17 (a)) whereas at 600 °C the average particle size is 30 nm (Figure 4.17 (b)). For the 700°C, the average particle size is 40 nm as shown in Figure 4.17 (c). The TEM images show the uniform distribution of the spherical shape of carbon nanospheres. It shows that the particle size decreases as the pyrolysis temperature increases but limited to 600 °C. From Figure 4.17 (a), the black spot present in the carbon nanospheres might be due to the incomplete removal of silica during

the carbonization process. Figure 4.17 (c) shows the presence of small white dots that might represent the presence of various compounds rather than carbon.
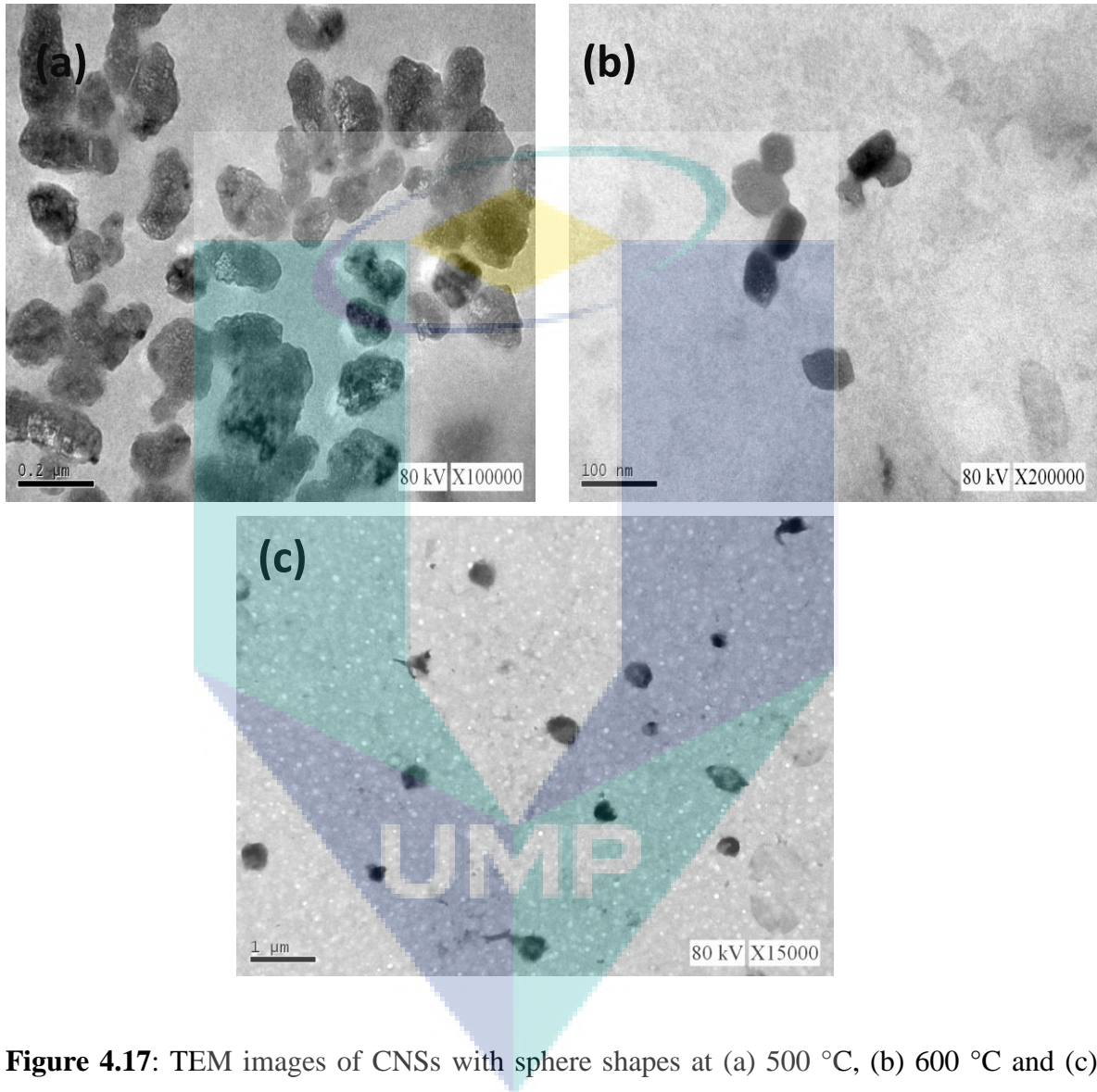
Figure 4.17: TEM images of CNSs with sphere shapes at (a) 500 °C, (b) 600 °C and (c) 700 °C pyrolysis temperature.

The particle size distribution based on TEM images in Figure 4.18 shows the CNSs obtained at the pyrolysis temperature of 600 °C exhibits the smallest particles, mostly in 10-20 nm sizes. Furthermore, the particle distribution for the 500°C pyrolysis temperature was in the range of 70-100 nm whereas 700 °C pyrolyzed CNSs contained larger particles size, in the range of 170-200 nm. Therefore, the optimum temperature to exhibit smallest particle size was 600 °C.
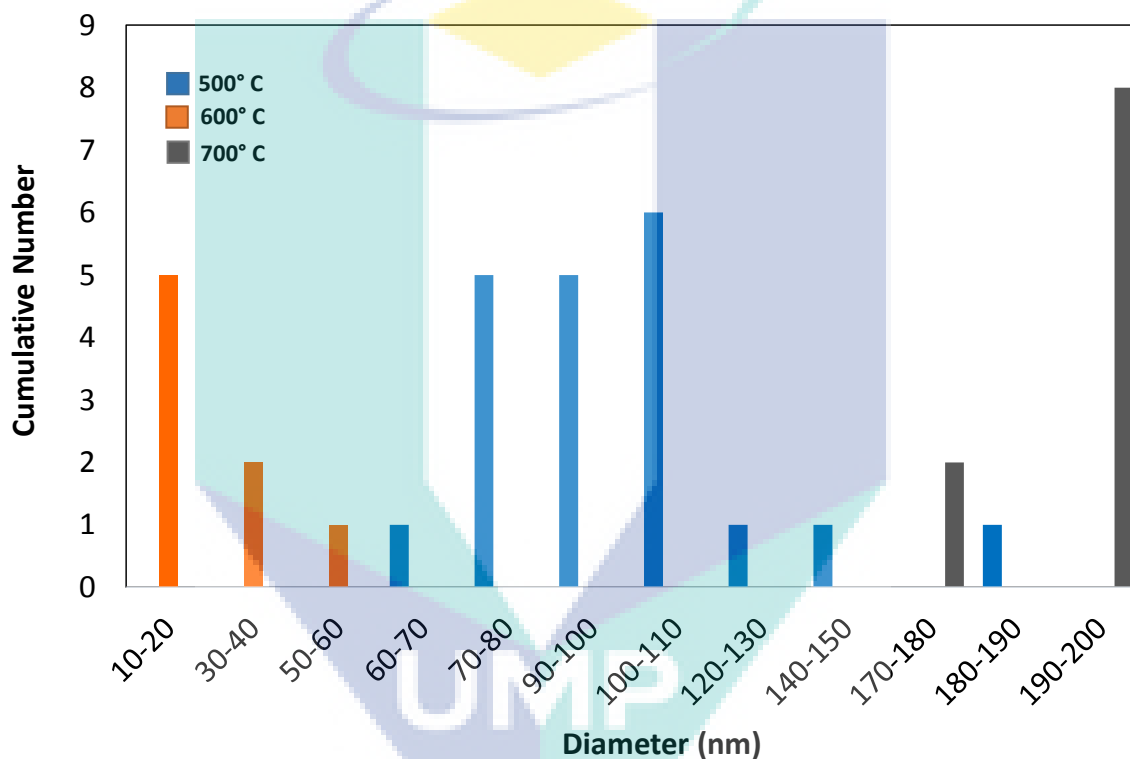
Figure 4.18: Particle distribution of TEM images with CNSs

From the data obtained for TEM and SEM, it can be clearly observed that the size difference of CNSs between this two analysis is quite differs. This phenomenon happened due to the different sample preparation in both cases. The area of measurements also might affect the obtained images since the CNSs was not activated so the size difference will be there. Besides that, the resolution of instruments and sample coating also might be the reason.

4.4 CHARACTERIZATION OF CARBON NANOSPHERES PREPARED USING SAGO HAMPAS

4.4.1 Fourier Transform Infrared Spectroscopy(FTIR)

In the FTIR spectra of the obtained CNSs, the strong absorption band around 1620 cm^{-1} were assigned to (C=O) bond of the carbonyl group. The absorption bands around 3400, 2900 and 1500 cm^{-1} are assigned to the C-OH, C-H and C=C stretch of the carbon skeleton. Large deviation in the shifts was observed in the region of 1500-900 cm^{-1}, that is due to the lignocelluloses characteristics in sago hampas as a precursor (Figure 4.19). Thus, the FTIR spectrum provides the information about the surface functional groups of the carbon.

Both figures show the FTIR spectra for CNSs treated at 400 °C and 600 °C (Figure 4.19 and Figure 4.20) that have some similar peaks such as around 3400 cm^{-1}, which represents C-OH stretching and around 2900 cm^{-1} that represents C-H stretching of the carbon skeleton. Besides that, the peaks observed at 1620 cm^{-1} for CNSs treated at 400 °C was assigned to C=O bond of carbonyl group but the peaks were shifted to 1563 cm^{-1} that represents the C-H bending for CNSs treated at 600 °C. The large deviation can be seen in the range of 1500 – 900 cm^{-1} for both samples as it is due to the lignocellulosic materials behavior from the sago hampas precursor. The shifting of the peaks in this range was increased as the pyrolysis temperature increased as the lignocellulosic material in the precursor is degrading.
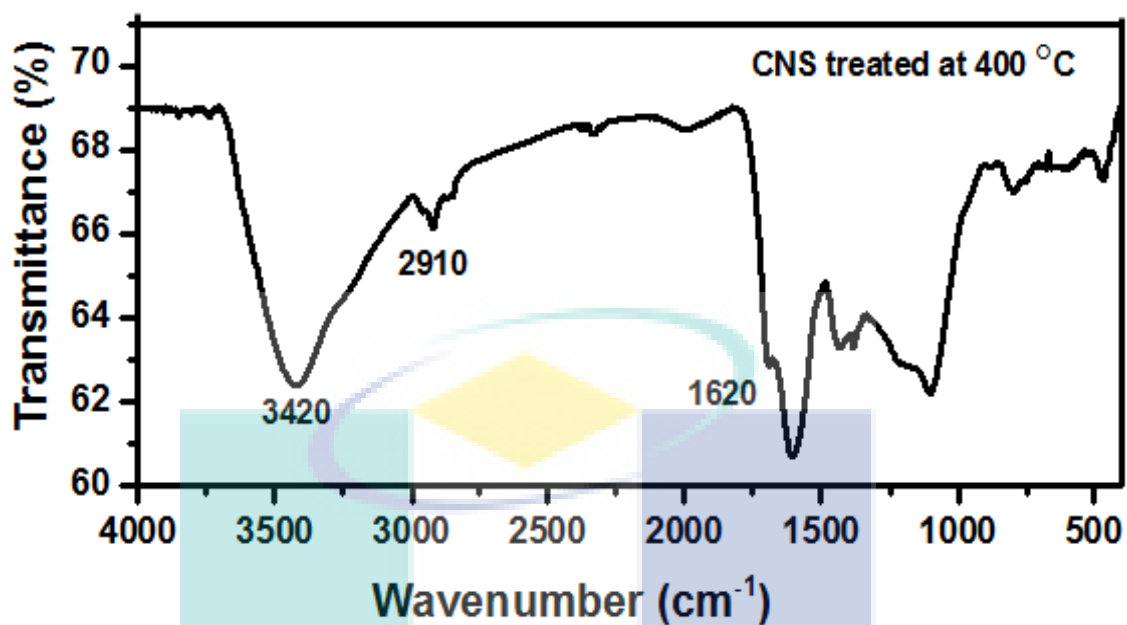
Figure 4.19: FTIR spectrum for CNSs treated at 400 °C.
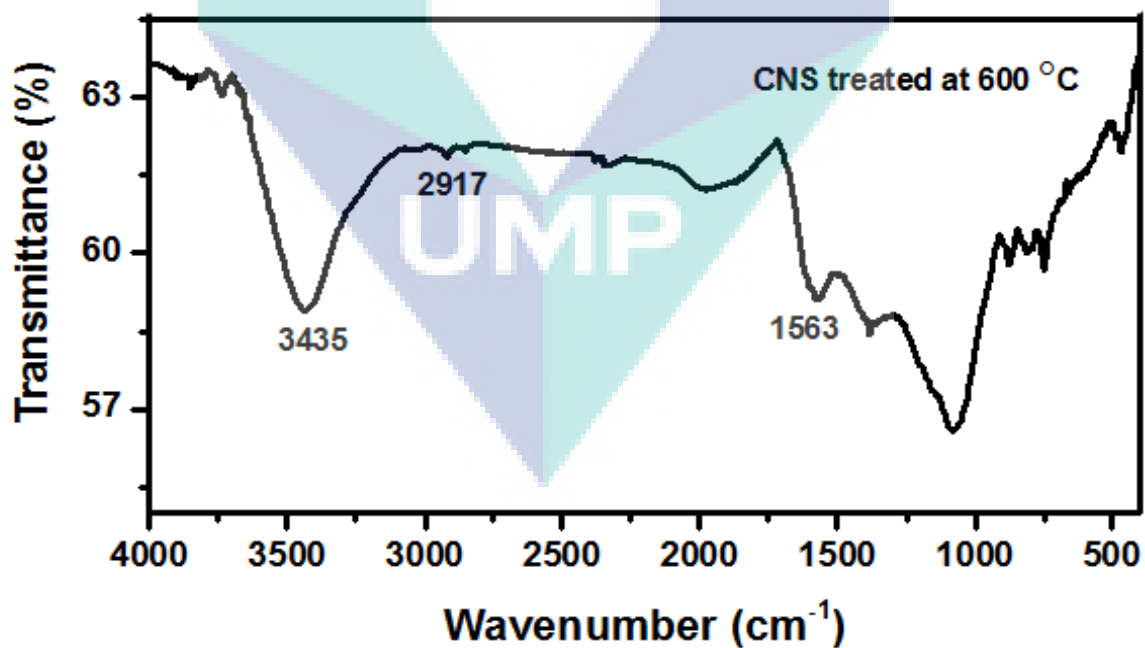
Figure 4.20: FTIR spectrum of CNSs treated at 600 °C.

4.4.2   X-Ray Diffraction (XRD)

Wide-angle XRD patterns give important information for the graphitic structures of carbon as shown in Figure 4.21. The CNSs treated at 400 ºC gave a main diffraction peak at $2\theta=25.4^o$ corresponding to 002, which can be attributed to graphite (ICDD 10777164). The interlayer d-spacing (d_{002}), which was used as a quantitative measurement of graphitic character, is 3.50 Å (Li et al., 2013). In contrast, the CNSs treated at 600 ºC gave a peak observed at $2\theta=26.8^o$ ($d_{002}=3.32$ Å), which is assignable to 002 of graphite (ICDD 10713739). At higher temperature, the interlayer d-spacing is slightly reduced. It is noted that additional peaks ($2\theta=23.5^o$ for 400 ºC, $2\theta=22.2^o$ for 600 ºC) are also confirmed. These peaks are probably due to the highly crystalline cellulose fibers (Mathew et al., 2005; Wu et al., 2013 and Klemm et al., 2005) which evolved from the hemicelluloses and celluloses of sago hampas. The most important point is that the XRD pattern for CNSs treated at 600 ºC show two peaks at $2\theta=41.5^o$ and 46.4^o, which can be assigned to 100 of graphite (*i.e.*, in-plane structure) (Kuga et al., 2002). This peak was not observed in the case of CNSs treated at 400 ºC (Kumar et al., 2014 and Ali et al., 2014). It is clear that high graphitic structure appeared after thermal treatment at 600 ºC.
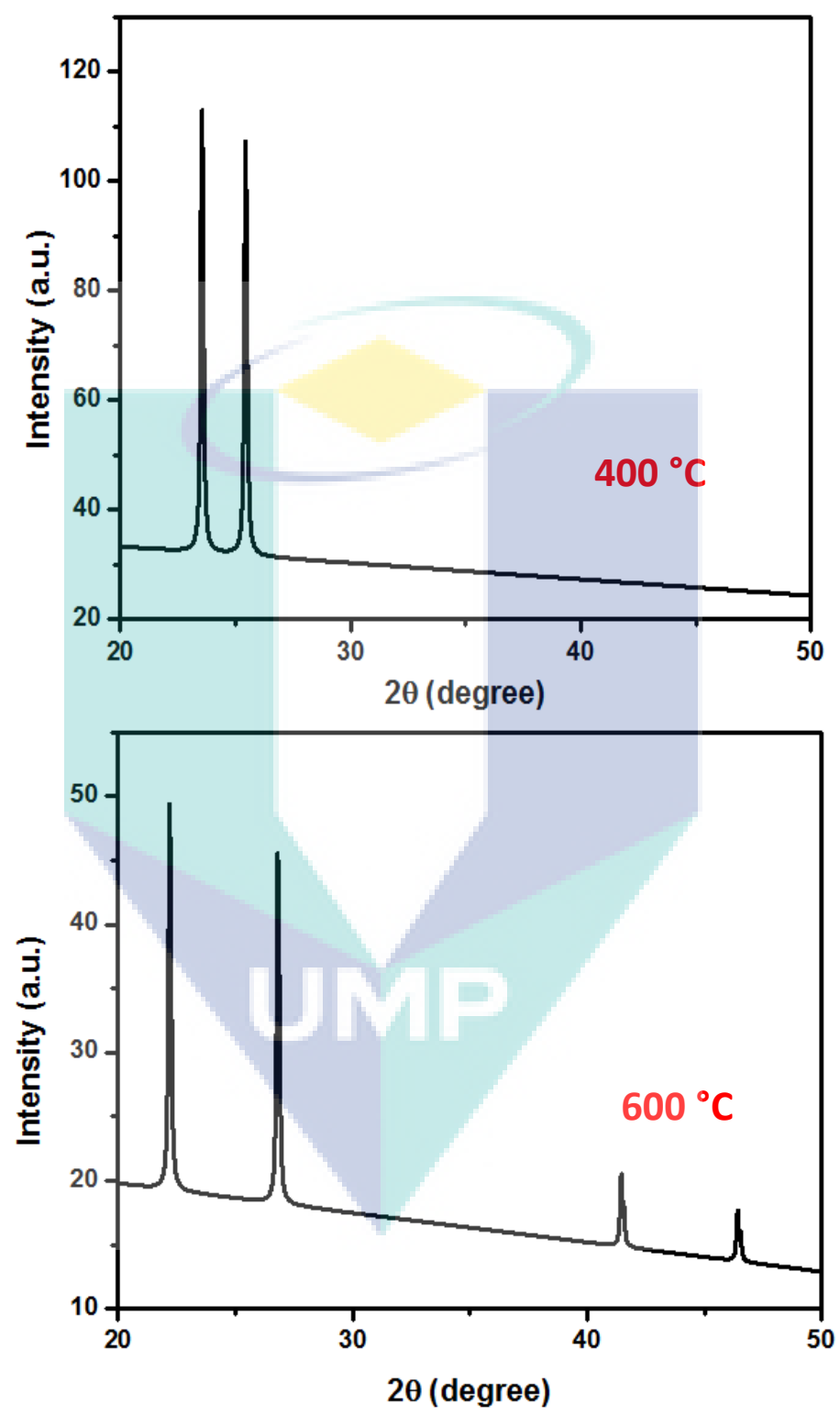
Figure 4.21: XRD for CNSs treated at 400 °C and 600 °C.

4.4.3 Raman Spectroscopy

Raman spectroscopy is extremely useful in deducing the graphitic structure of carbon materials. Raman spectra of CNSs treated at 400 and 600 ºC shows that the carbon materials produced two main peaks denoted as D- and G-bands as shown in Figure 4.22. The D-band, which is a diagnostic of disorder in the carbon structure, was observed at 1397 and 1380 cm^{-1} for CNSs treated at 400 ºC and 600 ºC, respectively. The G-band diagnostic of structural order, which is related to the sp^2 bonded carbon atoms from stretching modes of C=C bonds corresponding to the E_{2g} mode of graphite was found at 1619 and 1624 cm^{-1} for CNSs treated at 400 ºC and 600 ºC, respectively (Li, Y. et al., 2009 and Li, G. et al., 2008). Despite the different pyrolysis temperature, the peaks for D and G bands are similar. The graphitic character can further be assessed by the relative intensities of D- and G-bands (I_D/I_G). In present case, I_D/I_G ratio was found to be 0.87 and 0.84 at 400 ºC and 600 ºC, respectively (Qian et al., 2004). The full-width at half-maximum (FWHM) of the G- band is found to be 82 cm^{-1} and 63 cm^{-1} at 400 and 600 ºC, respectively. The graphitic character increases as the FWHM value decreases with the increase in the pyrolysis temperature. Thus, Raman results together with XRD results give evidence of the strong graphitic character of the prepared CNSs treated at 600 ºC.
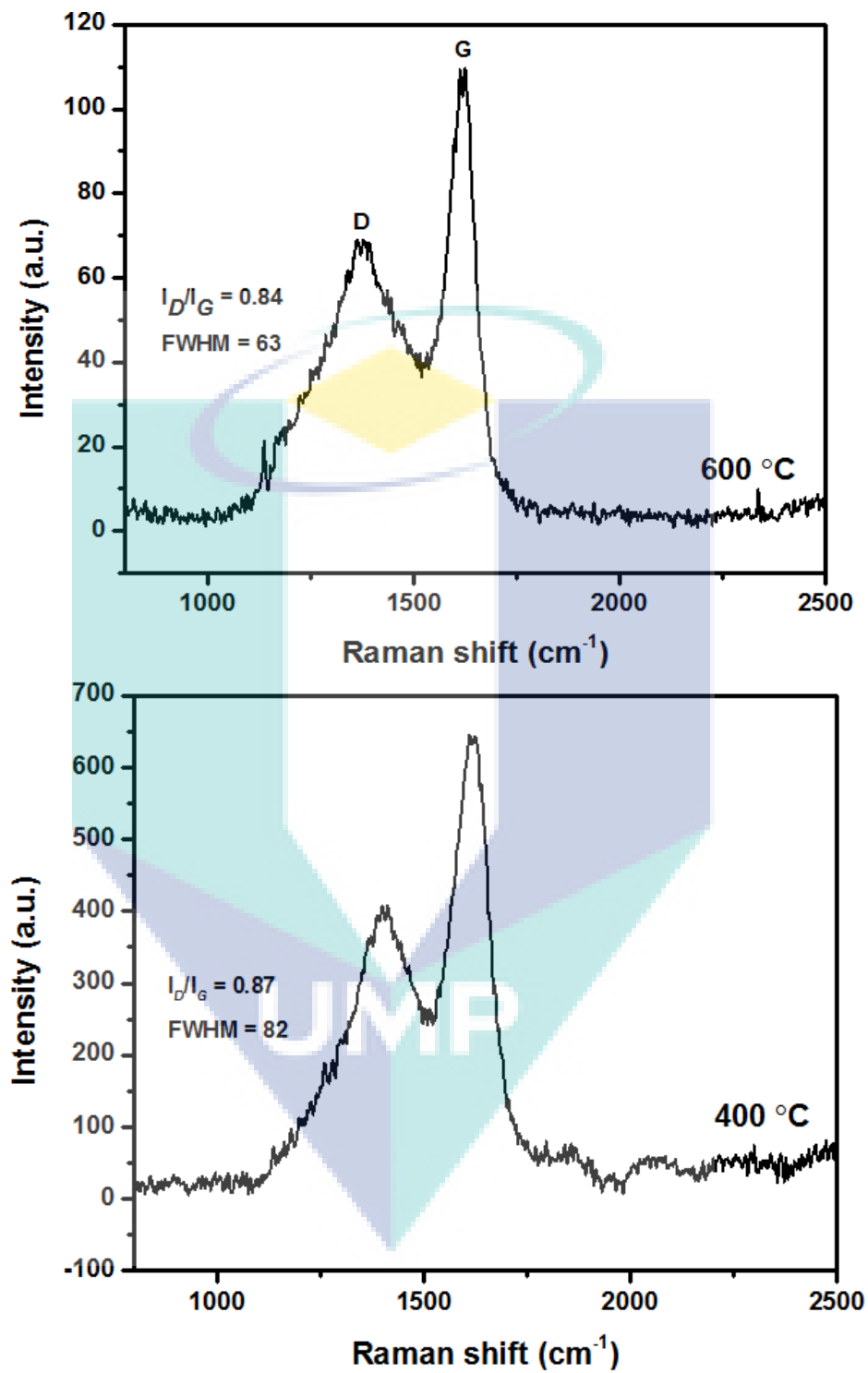
Figure 4.22: Raman for CNSs treated at 400 °C and 600 °C.

4.4.4 FESEM-EDX and TEM

FESEM (Figure 4.23) and TEM (Figure 4.24) observations were performed. As shown in the figures, all the obtained CNSs show a spherical shape without any irregular shaped carbon nanospheres. The TEM analysis presents the CNSs of an average particle size of 50 ± 5 nm obtained at pyrolysis temperature 600 $^{\circ}$C and 65 ± 5 nm at 400 $^{\circ}$C. FESEM of CNSs pyrolyzed at 600 $^{\circ}$C shows the particle size of around 60-70 nm and 80-90 nm at 400 $^{\circ}$C. The particle size distribution histogram is presented in Figure 4.23 (c) and Figure 4.23 (c). Thus, the particle size was decreased with an increase in the applied pyrolysis temperature. Higher temperature offers an ideal condition to obtain CNSs with smaller particle size. The EDX analysis (Table 4.3) confirmed that the relative carbon amounts for CNSs treated at 400 and 600 $^{\circ}$C are 80.15 and 83.79 atomic percentage respectively. With the increase of the applied temperature, the carbonization degree is improved, in which the particle becomes to shrink (*i.e.*, the particle size is slightly decreased).

Table 4.3: EDX analysis on carbon percentage.

Pyrolysis temperature (°C)	Carbon percentage (%)	
	Weight	Atomic
400	74.09	80.15
600	76.22	83.79
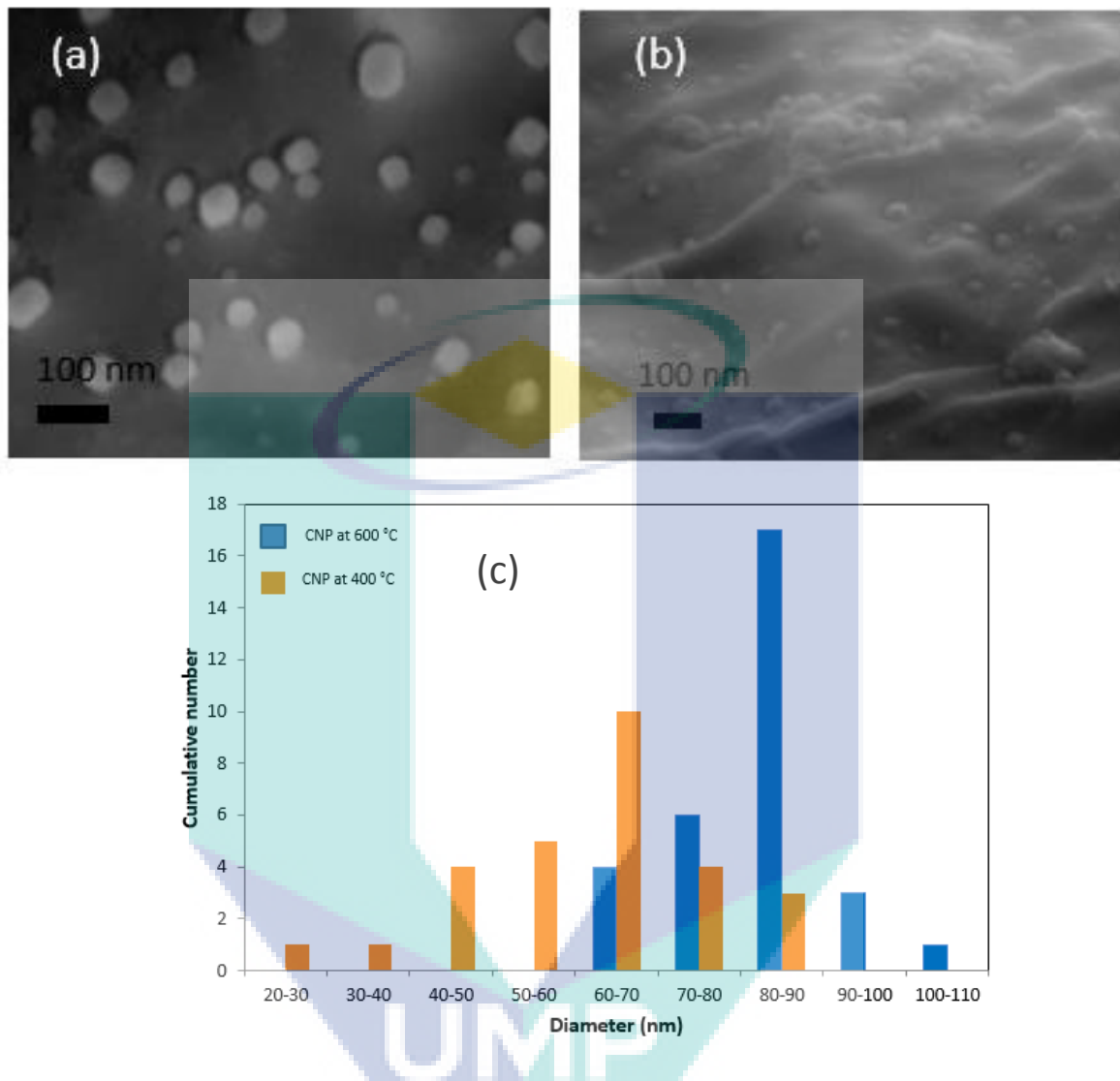
Figure 4.23: FESEM images of CNSs at (a) 600 °C (b) 400 °C (c) particle size distribution.
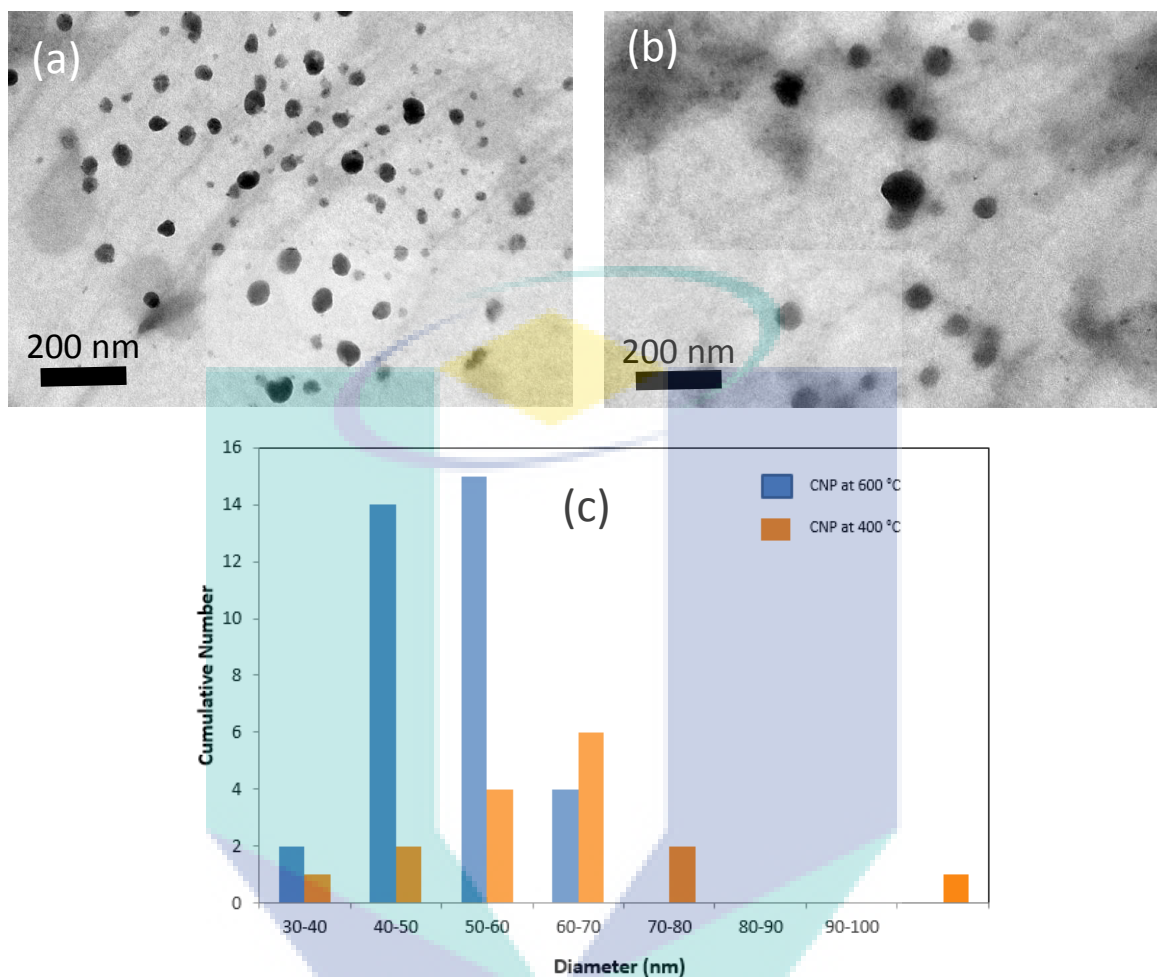
Figure 4.24: TEM images of CNSs (a) 600 °C, (b) 400 °C and (c) particle size distribution.

The same case happened for the CNSs obtained from sago hampas where it can be clearly observed that the size difference of CNSs between TEM and FESEM is quite differs. Similar explanation as mentioned for CNSs from OPL where different sample preparation in both cases can be the factor. The area of measurements also might affect the obtained images since the CNSs were not activated so the size difference will be there. Moreover, the resolution of instruments and sample coating also might be the reason.

4.4.5   Brunauer-Emmett-Teller (BET)

The porous nature was investigated through Brunauer-Emmett-Teller (BET) method. In IUPAC classification, the pore with diameters less than 2 nm is classified as micropore, whereas the pore with diameters from 2 to 50 nm is classified as mesopore. Table 4.4 shows the BET measurements of CNSs from sago hampas. For the CNSs treated at 600 $^{\circ}$C, the BET surface area (S_{BET}) is 64 m²·g^{-1} and t-plot micropore surface area ($S_{t\text{-plot}}$) is 38 m²·g^{-1}. The $S_{t\text{-plot}}/S_{BET}$ value is quite high (59.4 %), showing large contribution from the micropores. When the applied pyrolysis temperature is 400 $^{\circ}$C, S_{BET} and $S_{t\text{-plot}}$ values of CNSs are 30 m²/g and 14 m²/g, respectively and the $S_{t\text{-plot}}/S_{BET}$ value is 46 %. Hence, with an increase in pyrolysis temperature, microporous structure in the CNSs is gradually developed.

Table 4.4: BET measurements of CNSs from sago hampas.

CNSs	BET surface area (S_{BET}) (m^2/g)	t-plot micropore ($S_{t\text{-plot}}$) (m^2/g)	Micropore ratio ($S_{t\text{-plot}}/$ S_{BET}) (%)
400 °C	30	14	46
600 °C	64	38	59.4

4.5   APPLICATIONS: CELL IMAGING STUDY OF CNSs FROM OPL

4.5.1   Zeta Potential

Zeta potential values provide key information about the nanoparticles stability in suspensions and cellular uptake (Zeng et al., 2013 and Perrault et al., 2009). Zeta potential is measured to determine the suspension's ability of the particles in solutions. The good and excellent zeta potential values is an indicator that the particles can be used in the medical field such as for cell imaging, drug delivery (Mura et al., 2011) and also cancer therapy (Zhang et al., 2008). Higher values of zeta potential lead to fast approaching to the cell surface while the lower values might make the slow approaching and nanoparticles move away from target cells (Xu et al., 2006). The particle surface charge plays important roles for the targeting since it need to merge with the cell surface charge as it will determine the efficacy of drug targeting. Zeta potential measurement will determine whether the particle could reach the target cell or the stability of the dosage used was perfect (Honary and Zahir, 2013 and Selvi et al., 2008).

The zeta potential phase plot in Figure 4.25 showed the fast electric field reversal (FFR) information from 0 to 1.2 sec. It shows a rapid oscillating lower voltage to determine the mean zeta potential value whereas the V shape curve shows the slow field reversal (SFR). SFR was measured over the large voltage range to determine the large range potential distribution. Those pyrolyzed samples of 500 °C, 600 °C and 700 °C in the figure shows the high quality of the phase data plot. The lower quality of phase data will show the trending of FFR portion and higher noise where it will not appear in the smooth V curve (Zeta potential analysis of nanoparticles guidelines, 2012).
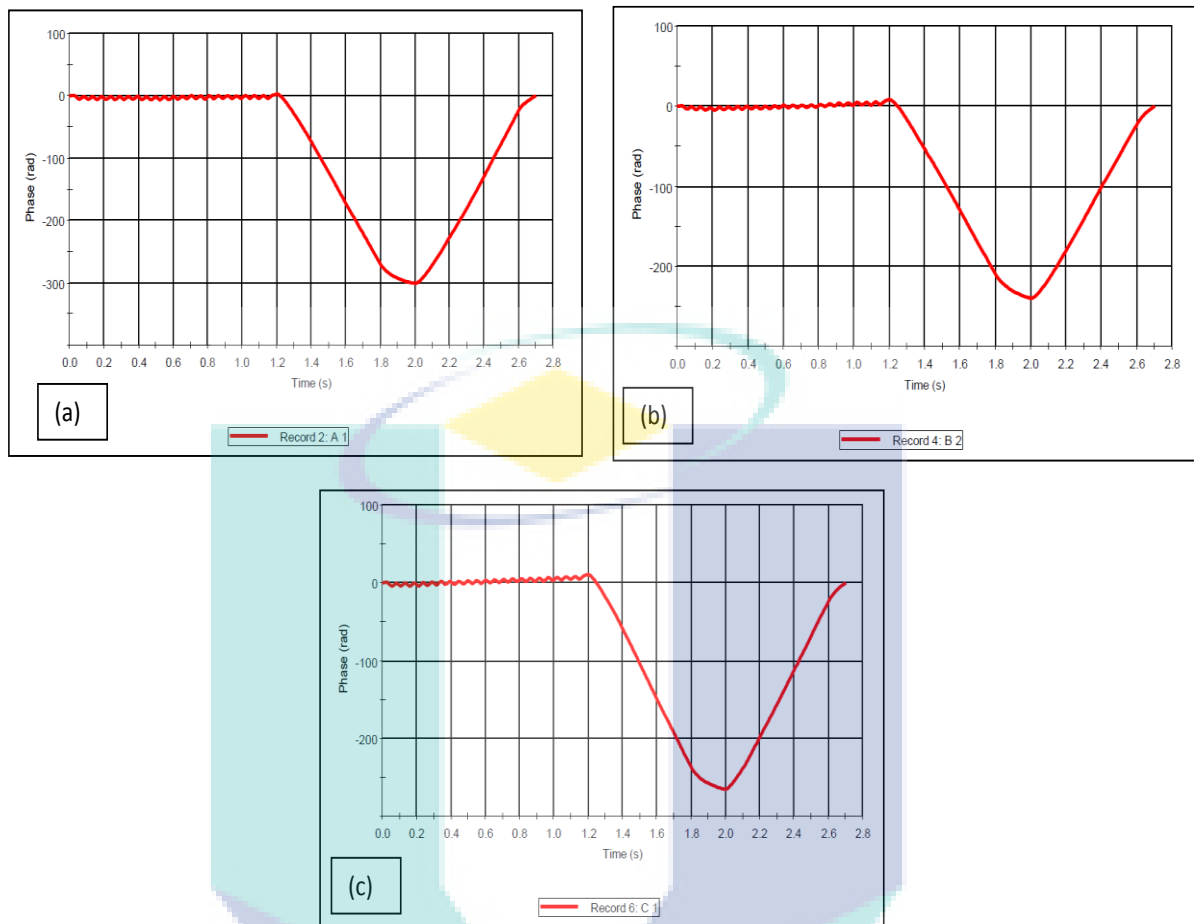
Figure 4.25: Zeta potential phase plot of CNSs from oil palm leaves, (a) 500 °C, (b) 600 °C and (c) 700 °C.
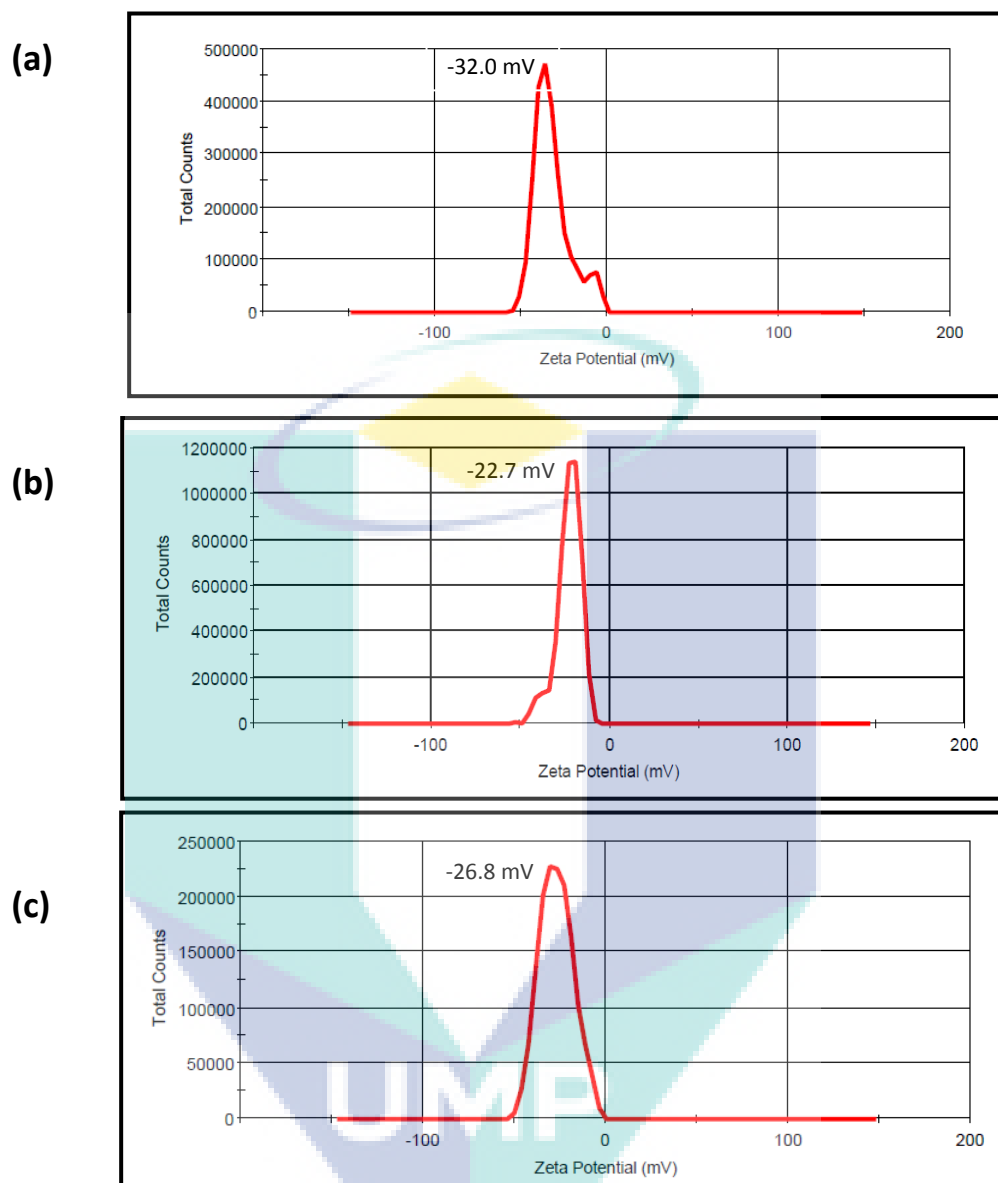
Figure 4.26: Zeta potential value for CNSs from oil palm leaves (a) 500 °C, (b) 600 °C and (c) 700 °C.

The zeta potential value (Figure 4.26) also have been measured for those three samples of different pyrolysis temperature. The pyrolyzed sample at 500 °C gave zeta potential value of -32.0 mV whereas 600 °C pyrolyzed sample value was -22.7 mV. For the CNSs 700 °C, it gives a value of -26.8 mV. All the carbon nanospheres were measured in suspension of deionized water. Among those three samples of carbon nanopsheres, the

CNSs 600 °C give the excellent zeta potential values that suggested the high stability of particles in the colloidal form.

The C-6 was used as a fluorescent dye that later been tagged with the CNSs. The zeta potential of tagged CNSs was again measured to observe the stability of both materials in the suspension form. From the Figure 4.27, the zeta potential value of -35.3 mV shows high stability in colloidal form. Furthermore, this value was much higher compared to CNSs value where it might be due to the tagging process of the CNSs and dye. The presence of these two materials increased the zeta potential values.
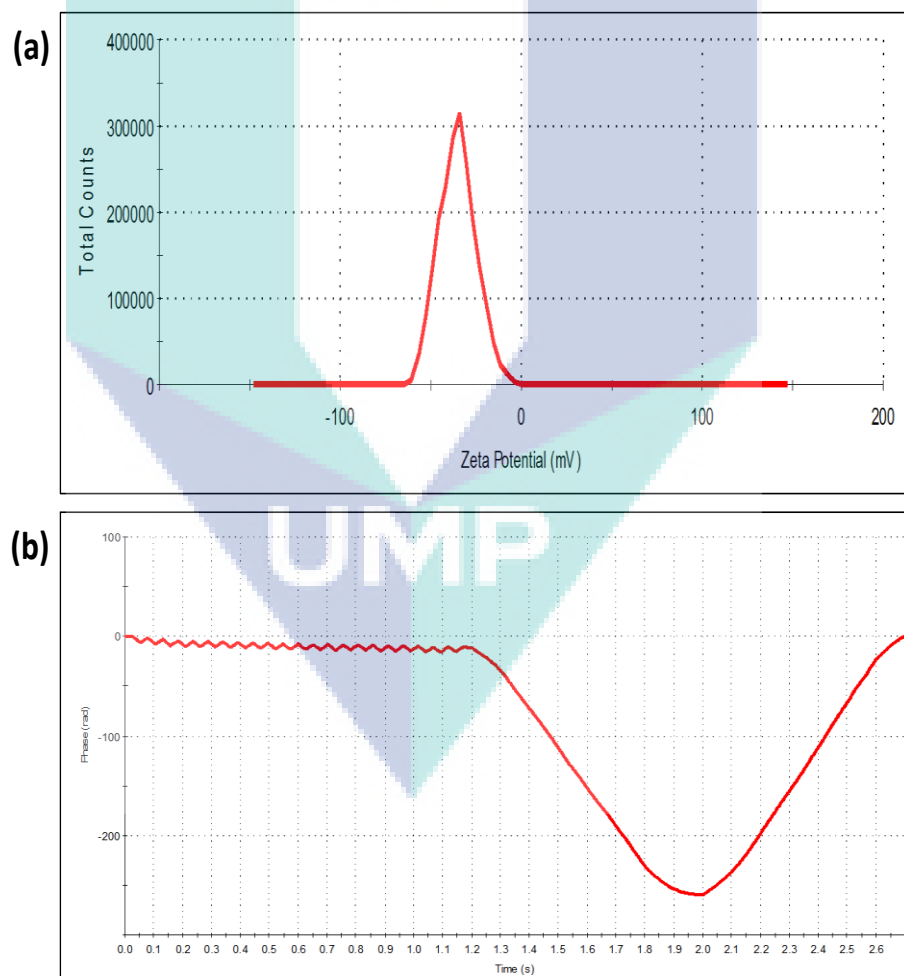
Figure 4.27: Measurement of (a) zeta potential and (b) phase plot of carbon tagged with C-6.

4.5.2 Fluorescence Microscopy

For the cellular uptake study, UMR 106 (OSTEOBLAST) cell line that was used as a model to observe the function of carbon nanospheres as a nanocarriers for therapeutics and drug delivery. The effect of the particle size might differ for each type of cells. The smaller diameter of the particles (100 nm) having efficient cellular uptake compared to the larger diameter particles. Besides that, different cell having a different way of cellular uptake mechanisms. In this study, C-6 was used as a fluorescent probe for tagging with carbon nanospheres that can quantify the cellular uptake and help for easy visualization of carbon nanospheres in the cultured cell. Previous study showed that C-6 was suitable for the cellular uptake study as it do not cause acute toxicity (Doolaanea et al., 2014).

The C-6 was tagged with carbon nanospheres and cell uptake study was performed according to the method described by Doolaanea et al., 2014. After 72 hours treated with C-6 tagged carbon nanospheres, the cells were washed using PBS and images of the cellular uptake results was observed using a fluorescence microscope (Figure 4.28). The images show that carbon nanospheres were efficiently taken up by the UMR 106 (OSTEOBLAST) cells without significant cytotoxicity.
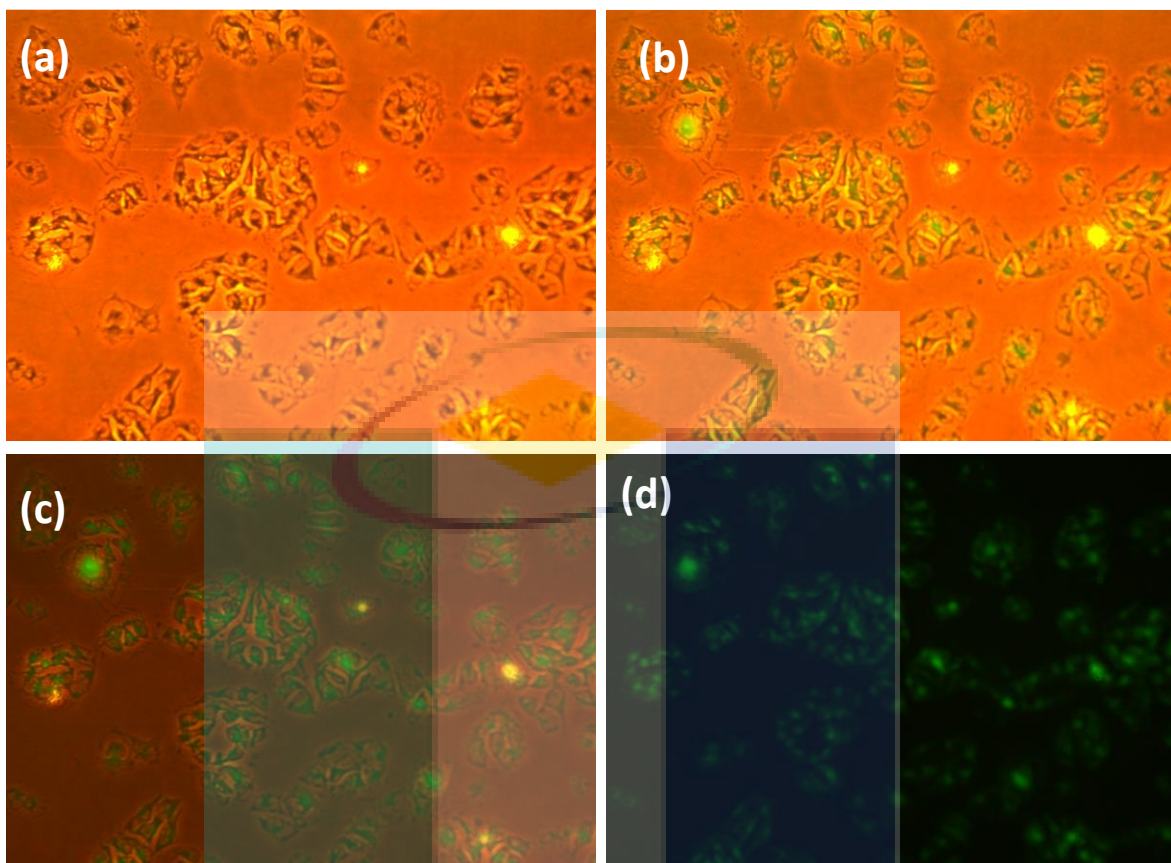
Figure 4.28: (a) Untreated UMR 106 (OSTEOBLAST) cell line (phase contrast image), (b) and (c) Cell treated with CNSs (merged phase contrast image), (d) Cell treated with CNSs (fluorescence image).

Other than that, the cellular uptake studies also had been done using different type of cells which are A375 (Figure 4.29), N2A (Figure 4.30), and MDCK (Figure 4.31). The cells treated with CNSs for 2 hours and 4 hours were observed under fluorescent microscopy.

Melanoma cell lines used which is A375 was treated with CNSs tagged with C-6 as a fluorescent dye. The images were taken for the cells treated at 2 hours and 4 hours. From the Figure 4.29 (a) and (b), where the cells were treated for 2 hours, the cellular uptake of C-6 tagged CNSs was not significant. However, after 4 hours treatment, the green fluorescence observed around the nucleus of the cells as shown in the Figure 4.29 (c), (d) whereas Figure 4.29 (e) and (f) indicating nanoparticle localization within cells. Green fluorescence appeared from C-6 tagged with CNSs that was taken up by the cell after crossing the cell membrane.

Neuroblastoma cell line (N2A) showed distinct shape of the cells (Figure 4.30 (a) and (b)) but after nanoparticle incubation for 4 hours green fluorescence around the nucleus of the cell observed under fluorescence phase. After 4 hours treatment, the CNSs exhibited maximum uptake in the cells as shown in the Figure (c) and phase contrast image in Figure (d). There is no fluorescence was observed after 4 hours where it cannot be seen properly as shown in Figure 4.30 (e).

On the other hand, cell line of MDCK after 2 hours (Figure 4.31 (a)) and 4 hours (Figure 4.31 (b) and (c)) fluorescent images did not exhibit significant uptake may be dependent on the respective cellular physiology.
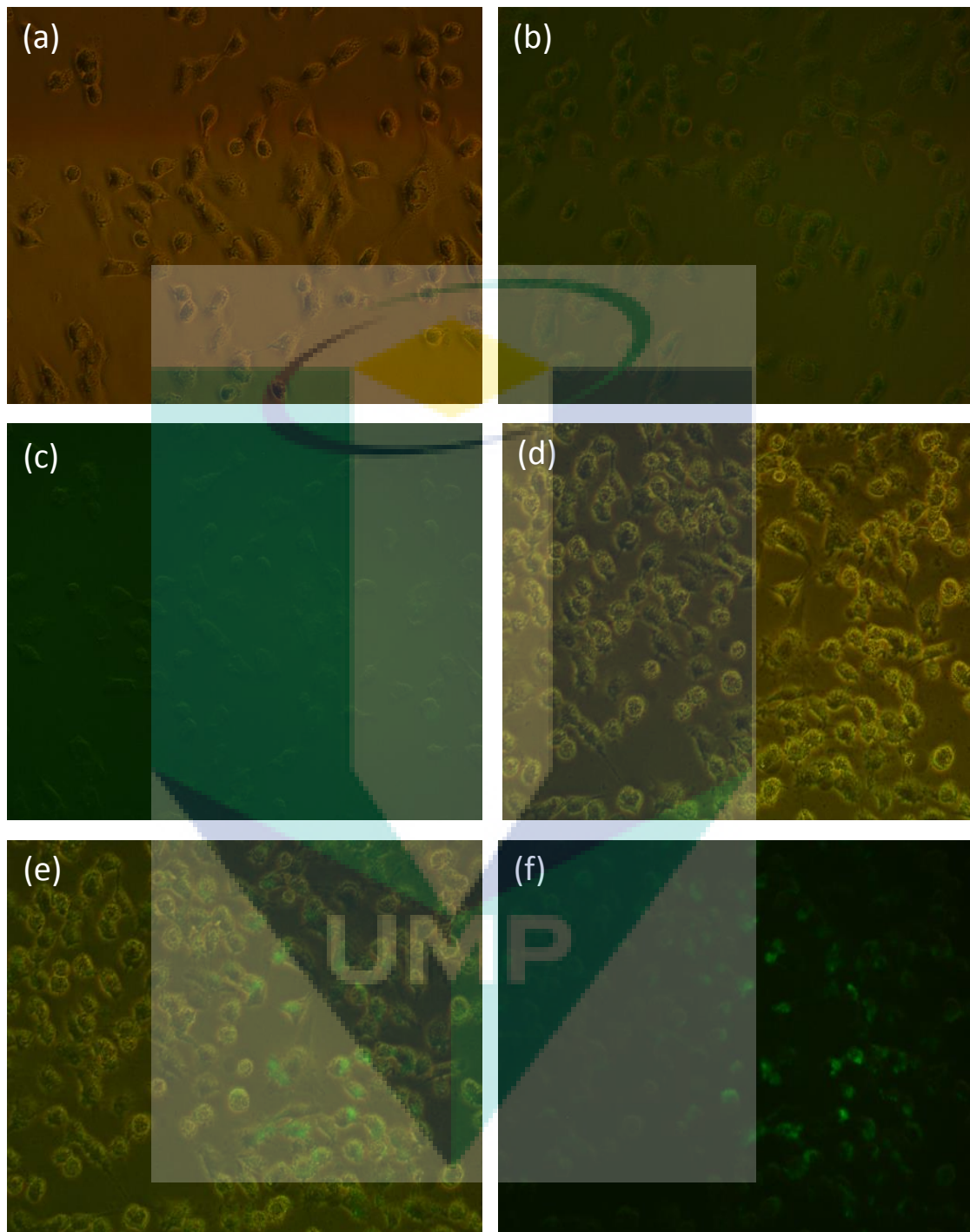
Figure 4.29: Melanoma cell lines images of A375 treated after 2 hours (a) phase contrast; (b) merge phase; (c) fluorescence phase and after 4 hours (d) phase contrast; (e) merge phase; (f) fluorescence phase images.
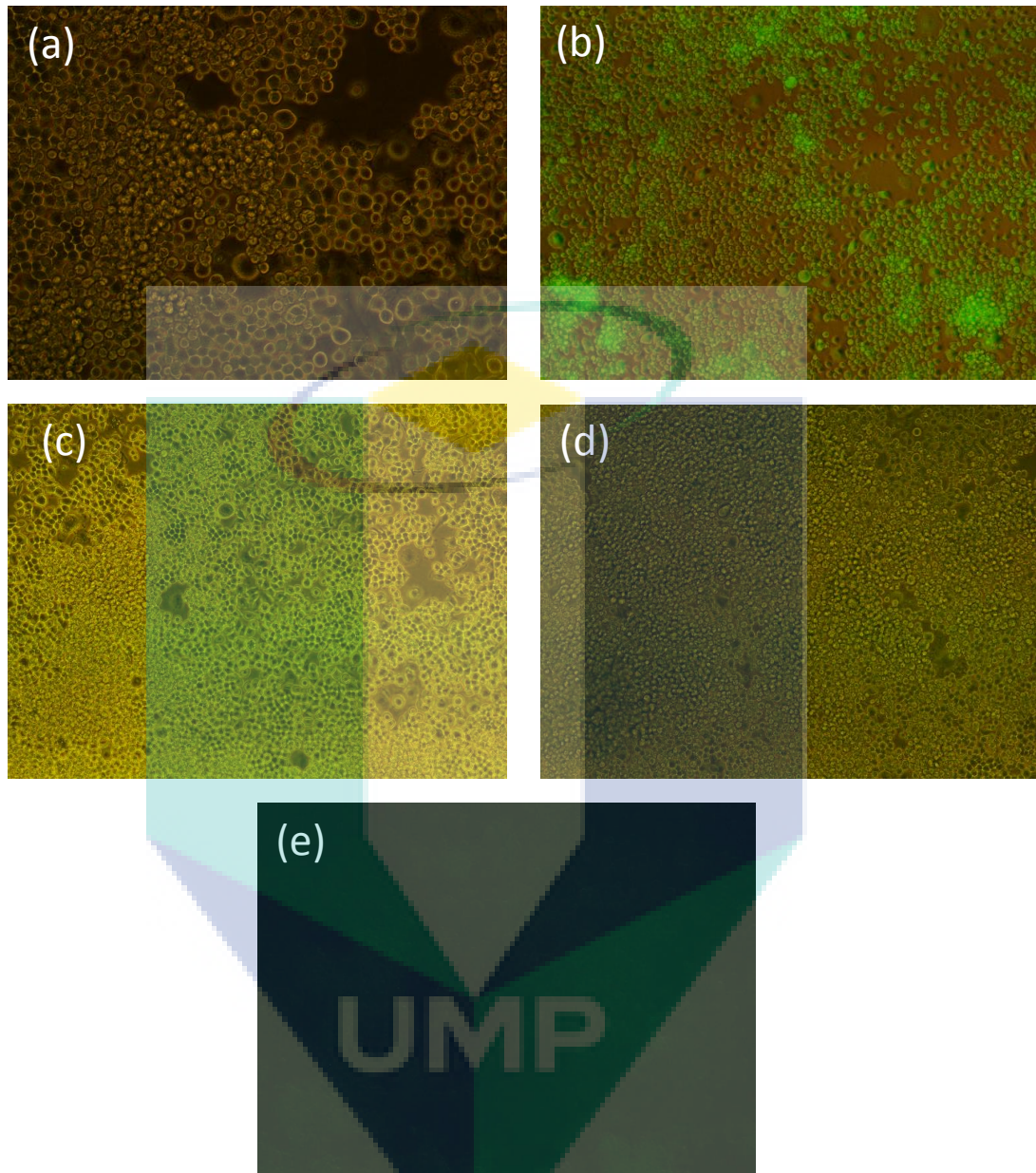
Figure 4.30: Neuroblastoma cell lines images of N2A treated after 2 hours (a) phase contrast; (b) merge phase; and after 4 hours (c) phase contrast; (d) merge phase and (e) fluorescence phase.
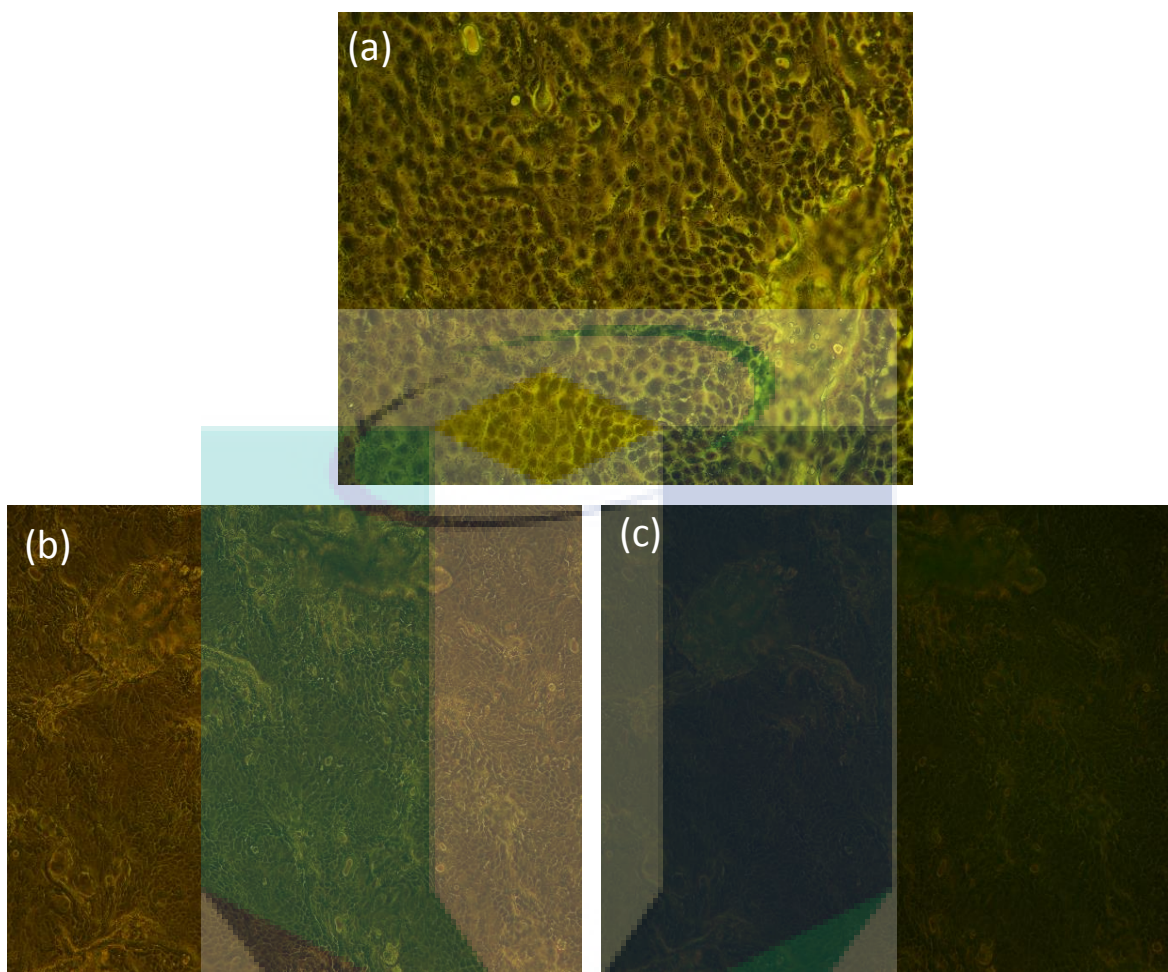
Figure 4.31: MDCK cell lines treated after 2 hours (a) merge phase; and after 4 hours (b) phase contrast; (c) fluorescence phase images.

The cell line used which is A375 and N2A shows good cellular uptake of the CNSs that can be observed from the images whereas the MDCK images was not clearly observed that may be due to low cellular uptake. Different cell have different mechanisms and cytotoxicity effect that need more specification and details study, for example the concentration of CNSs for the cell. Therefore, the cytotoxicity of the CNSs in the biological system which is cell line should be studied to check the viability of the cell with the present of CNSs.

4.5.3   Cytotoxicity assay

Cell viability was performed to check cytotoxic effect of carbon nanospheres in inhibiting proliferation of cell lines following designated concentration. Viability of cell lines was depicted in Figure 4.32. It was found that when A375, MDCK and N2A cells are treated with CNSs at increasing concentrations (25, 50, 100 and 250 μg/ml), cellular viability was reduced. The nanospheres caused increased A375 cell's death at increasing concentration and IC_{50} of 90 μg/ml was determined. No IC_{50} concentration was reported for MDCK and N2A cell as it was more than 250 μg/ml.
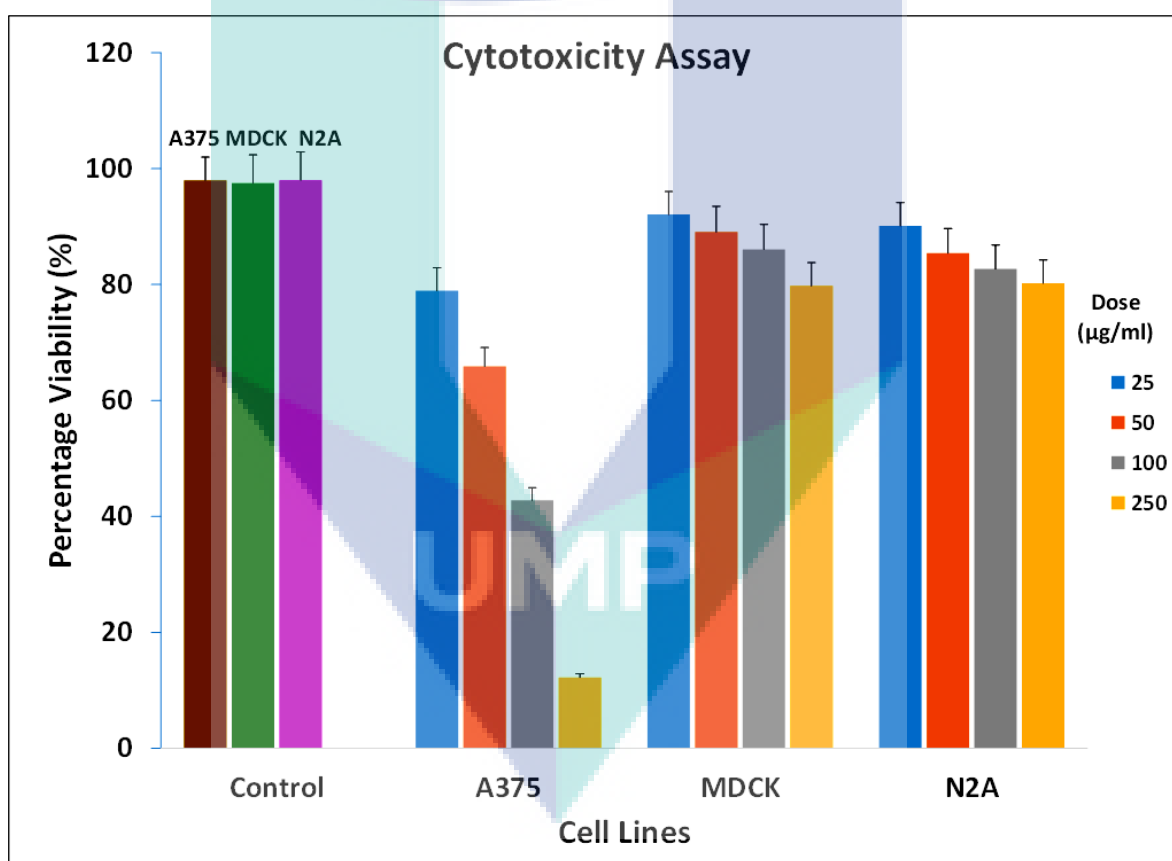
Figure 4.32: Percentage viability of cell lines 24 h after treatment with carbon nanospheres. Data are expressed as percent viability against untreated control (Mean±SD, n=3) of three independent experiments. Untreated control contained basal media.

Based on Figure 4.32, it showed the cytotoxicity effect of CNSs towards cell. For A375 it shown that the cell viability decreased as the dose level increased. In the case of MDCK cells, the cell viability gradually decreases as the dose of CNSs increases and the same pattern observed in the N2A cells. The dispersion medium for the CNSs was used as control in each cell for the entire study. Based on the ANOVA with Tukey test analysis, the comparison was made between the control and the subsequent doses of the CNSs that the cells were exposed to. All doses of CNSs is significantly differs from the control in terms of cell viability. This indicates that CNSs showed enhance cytotoxicity with increased in dosage level. This similar phenomenon is observed for all the three cell lines (A375, MDCK and N2A) used in the study. From this study, it shows that the CNSs inhibit cell proliferation of MDCK and N2A at low percentages but it clearly created cell apoptosis for A375 with the effect of dose dependent. Data from this study can provide the useful information for further study by using different type of cell and more varies concentration that might be useful for anti-cancer alternatives. (Xu et al., 2014).

4.5.4 FESEM-EDX

The tagging activity of CNSs with fluorescent dye which is C-6 also had been measured by FESEM-EDX where the structure and images of particles before and after tagging can be observed. Figure 4.33 (a) belongs to the CNSs that appeared as a single particles and Figure 4.33 (b) shows the agglomeration of CNSs after been tagged with C-6 that proved the combination of these two materials. Besides that, EDX analysis was done to measure the elemental analysis after the tagging process. From Figure 4.34, it shows the EDX data for CNSs before and after tagged with C-6. Extra elements present in the tagged CNSs especially sulphur (S) that come out from the C-6 acts as an evidence of the incorporation of CNSs with dyes.
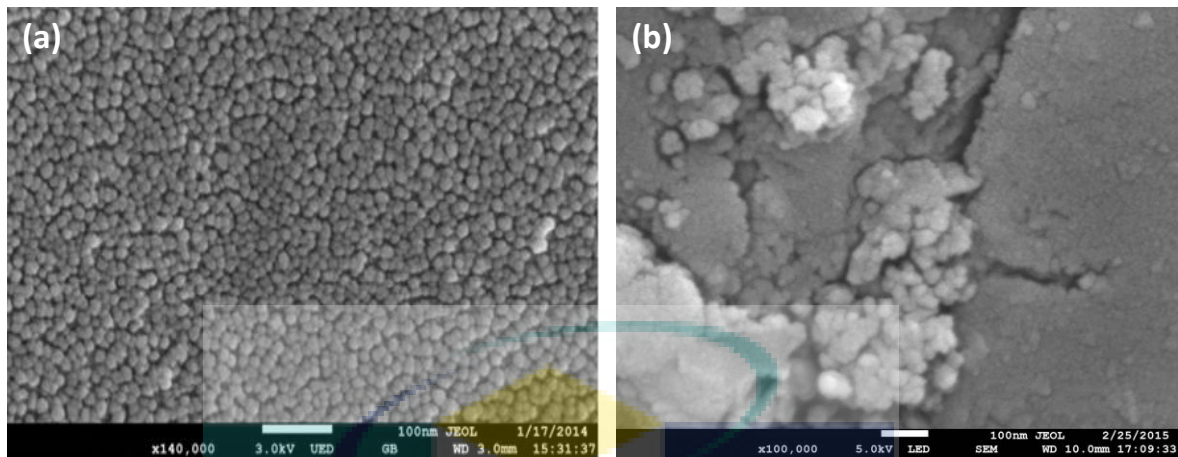
Figure 4.33: FESEM images of (a) CNSs at 600 °C and (b) CNSs after tagged with C-6.

(a)

Element	Weight (%)	Atomic (%)
C	82.73	87.90
O	13.19	10.52
Mg	0.55	0.29
Al	0.22	0.10
Si	0.92	0.42
K	0.56	0.18
Ca	1.83	0.58

Full Scale 4516 cts Cursor: 0.000

(b)

Element	Weight (%)	Atomic (%)
C	74.82	80.16
O	24.00	19.30
Si	1.07	0.49
S	0.11	0.04

Full Scale 4559 cts Cursor: 0.000
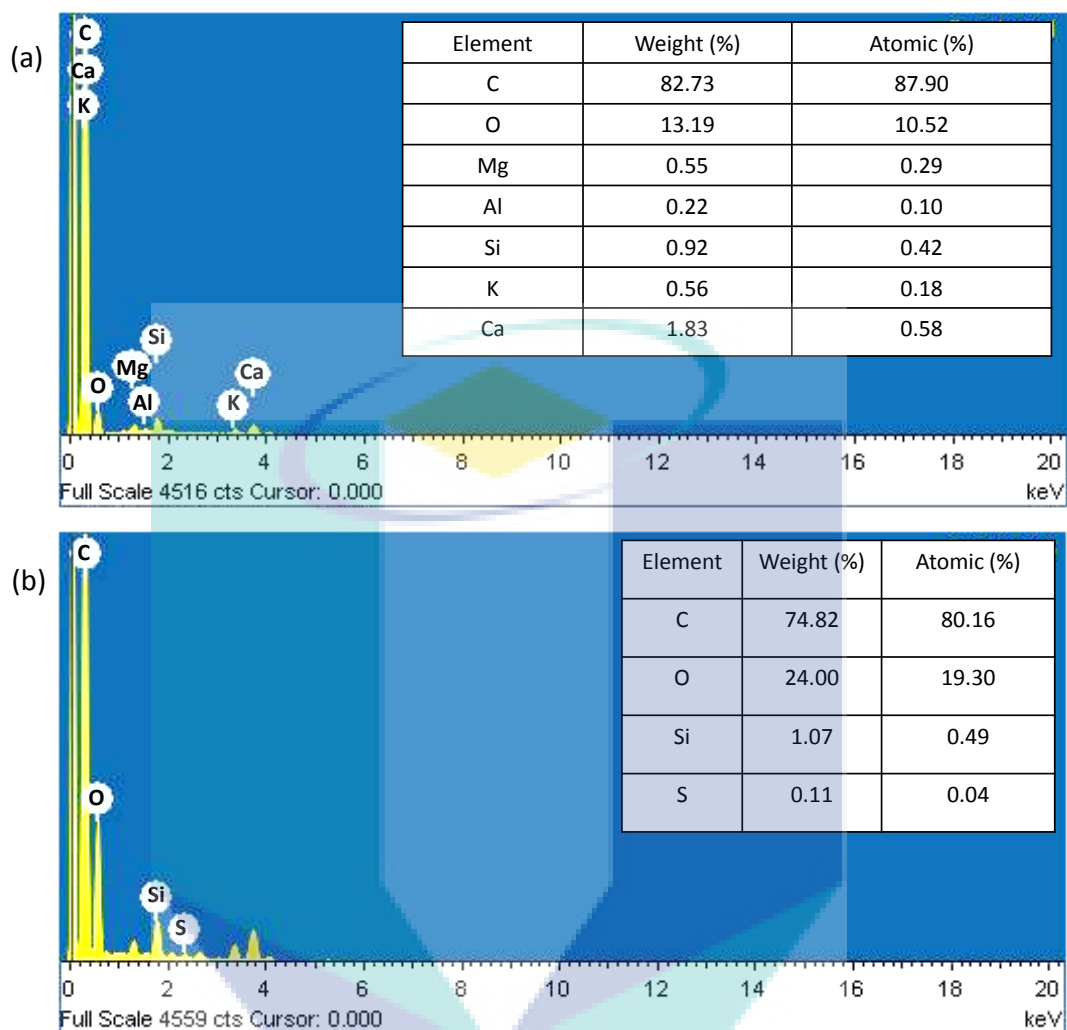
Figure 4.34: EDX analysis for (a) CNSs and (b) CNSs tagged with C-6.

4.6   CELL IMAGING STUDY ON CNSs FROM SAGO HAMPAS

Sago hampas pyrolyzed CNSs also had been studied further for cell imaging where the CNSs were tagged with same dyes of C-6. The tagged particles were mixed and measured by zeta potential instruments to observe the stability of tagged particles in suspension form. The CNSs obtained from sago hampas shows stable suspension behaviour as observed by the zeta potential values (Figure 4.35). CNSs pyrolyzed at 400 ºC exhibits zeta potential of –32.5 mV as shown in Figure 4.35 (b) whereas CNSs obtained at 600 ºC

shows –32.1 mV in aqueous solution (Figure 4.35 (a)). The negative surface charge for both CNSs may be linked to the surface functional groups as observed in the FTIR studies.
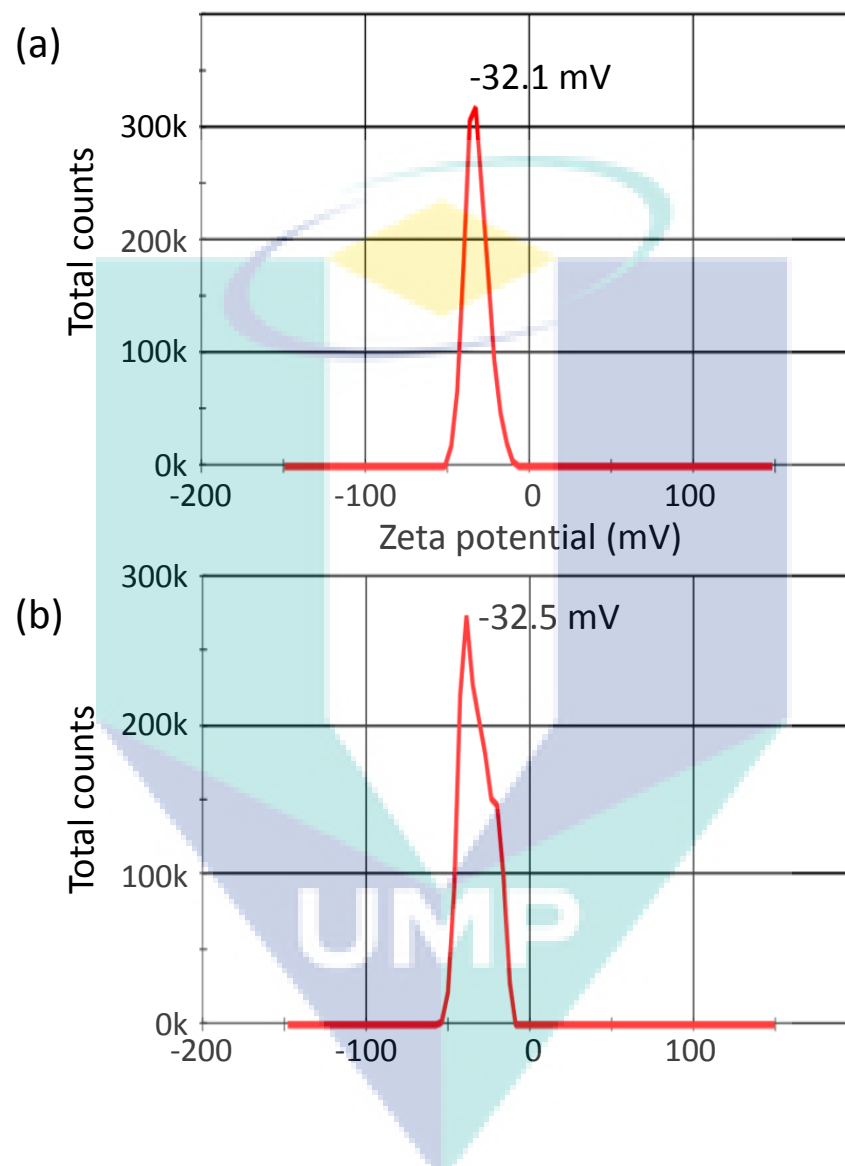
Figure 4.35: Zeta potential curves of an aqueous solution of CNSs prepared from sago hampas treated at (a) 600 °C and (b) 400 °C.

Presented CNSs with high zeta potential values indicates sufficient stability necessary for biological applications. Currently, CNSs are explored as interesting candidates for imaging applications for their size-guided cellular entry, low cytotoxicity profile and tunable emission properties (Bhunia et al., 2014). Synthesized CNSs from bio

waste with nano-scale particle size was expected to favour size related cellular entry. Owing to the particle size of CNSs pyrolyzed at 400 ºC, the tagging of CNSs with fluorescent dye C-6 was examined as it is in the size range favouring cellular uptake of nanoparticles (Alexis et al., 2008 and Yan et al., 2010). The FTIR spectrum of the C-6 tagged CNSs exhibited peak shifts.
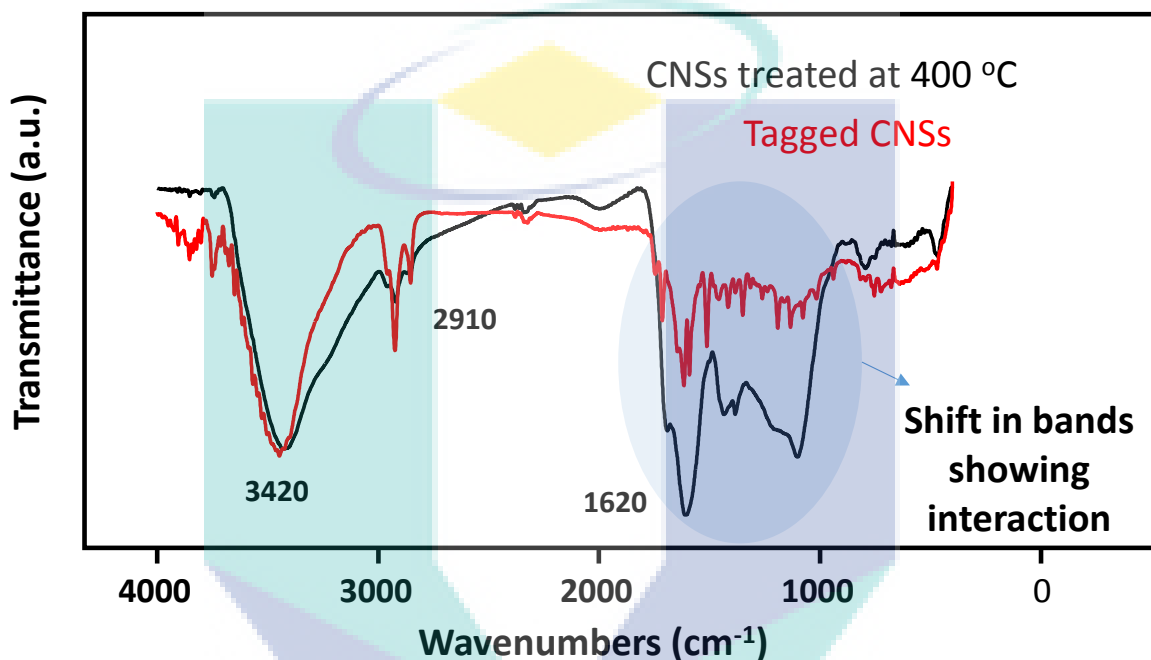
Figure 4.36: FTIR spectrum of CNSs treated at 400 ºC and tagged CNSs.

As shown in Figure 4.36 above, these peak shifts suggest the interaction of the fluorescent dye with the CNSs. The suspension of the CNSs in aqueous solution was shined with UV light source but does not exhibit any colours (Figure 4.37(a)) whereas the tagged CNSs exhibited the colour (Figure 4.37(b)), indicating the fluorescent nature after tagging. The CNSs also mixed well with the fluorescent dyes as shown in the figure. This gives a preliminary idea about the suitability of the present CNSs for cell imaging application
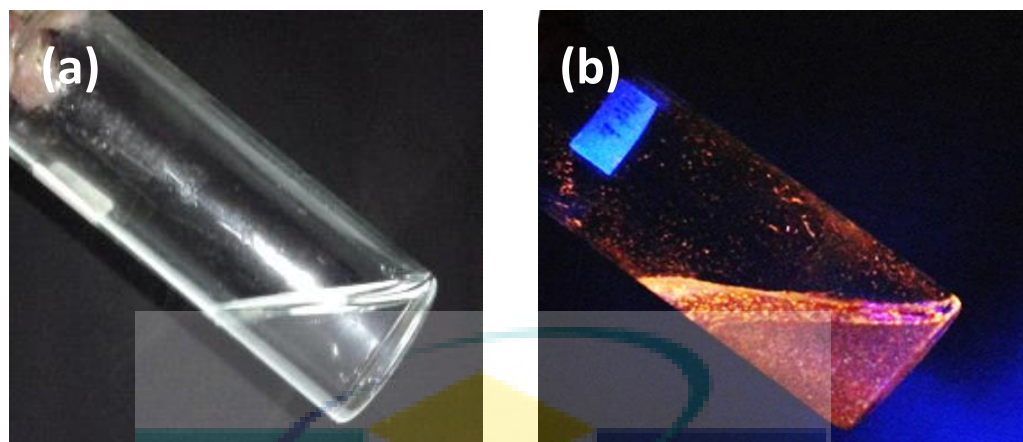
Figure 4.37: Images of an aqueous solution of CNSs treated at 400 ºC (a) before and (b) after tagging.

Additionally, the FESEM also had been used to compare the structures and images of CNSs before and after tagging process as shown in Figure 4.38 (a) and (b). The differences between the CNSs alone and after being tagged with dyes was obviously observed where the CNSs that exhibits single particles distribution turns to formation of particles aggregation due to the addition of C-6. The aggregation of particles shows that the two materials was tagged to each other. Furthermore, the tagged samples were then analysed by EDX to check the elements present. Figure 4.39 (a) shows the CNSs element whereas Figure 4.39 (b) belongs to tagged CNSs that shows extra elements present including sulphur (S) that come from C-6 in the tagged CNSs.
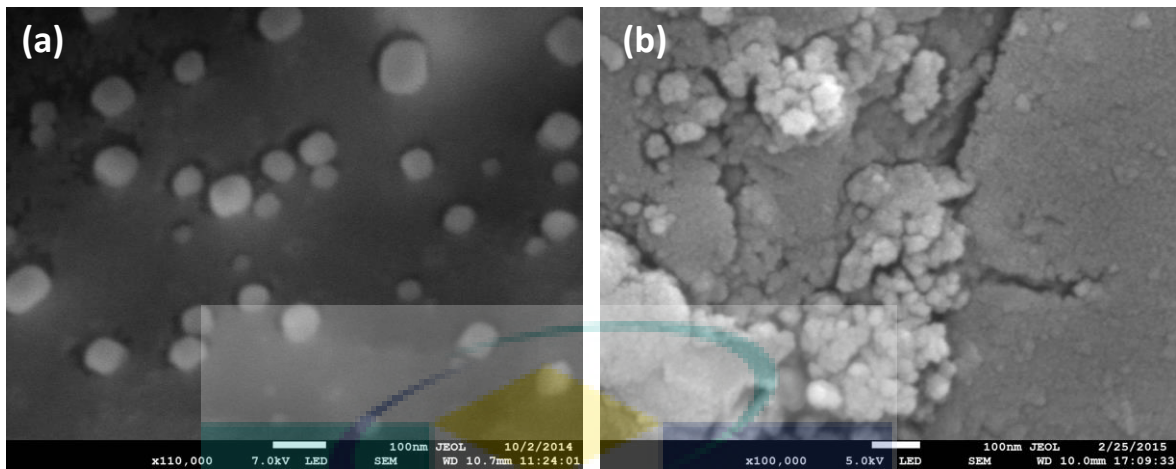
Figure 4.38: FESEM images of (a) CNSs and (b) tagged CNSs with C-6.

(a)

Element	Weight (%)	Atomic (%)
C	76.22	83.79
O	15.34	12.66
Si	4.20	1.97
Cl	4.24	1.58

(b)

Element	Weight (%)	Atomic (%)
C	73.69	79.32
O	24.68	19.94
Si	1.50	0.69
S	0.12	0.05
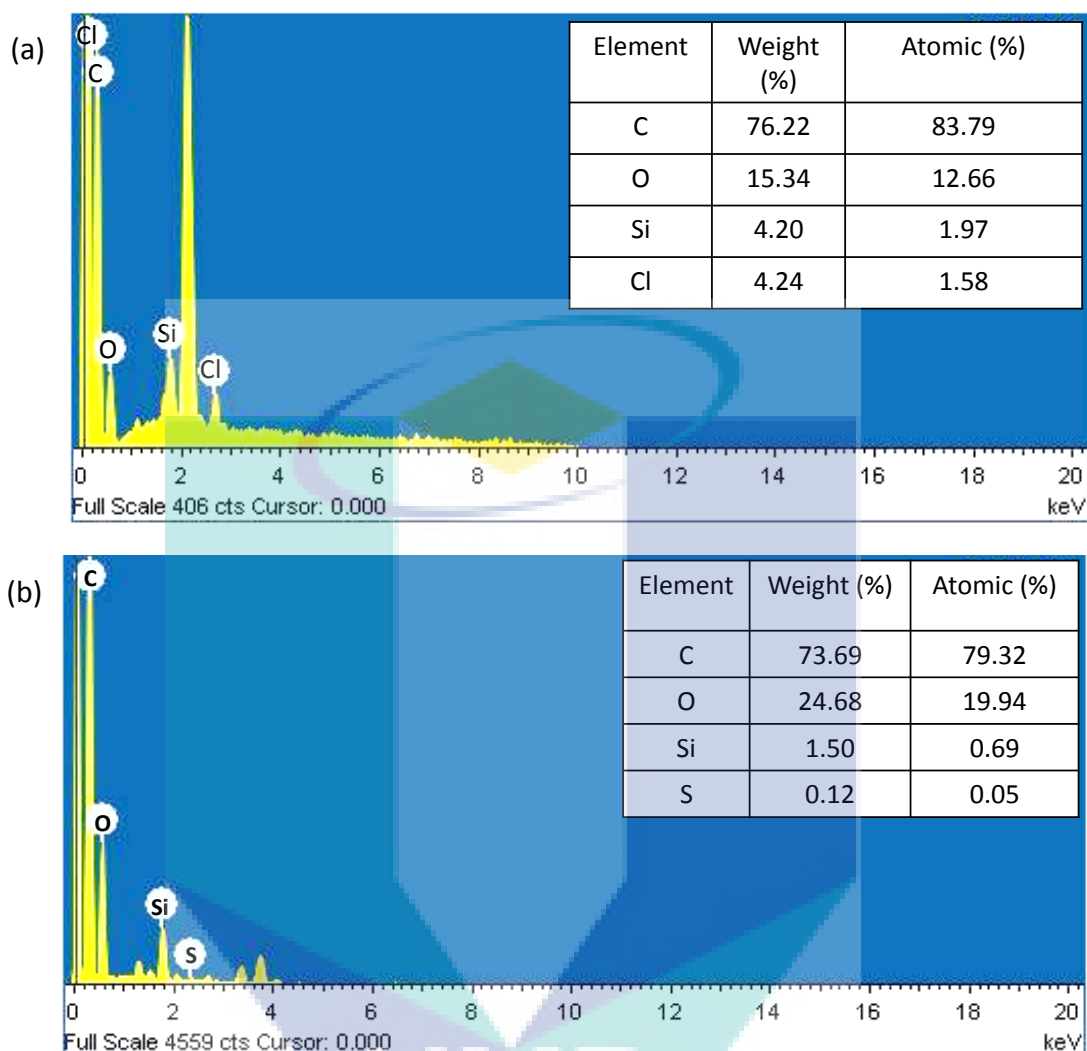
Figure 4.39: EDX analysis of (a) CNSs and (b) tagged CNSs with C-6.

So, bio waste materials are having very high potential to produce carbon nanospheres with wide potential areas especially in biotechnology field and this method helps to reduce the environmental problems associated with oil palm leaves and sago hampas. Further detail investigation might help us to understand more on their cellular uptake, which can be studied in the future.

.

CHAPTER 5

CONCLUSION AND RECOMMENDATIONS

5.1   SUMMARY OF THE RESULTS

Based on the findings and analysis on the data collected, bio waste can be utilized for valuable nanomaterials namely carbon nanospheres that have high potential for biotechnology. Bio waste used, which are oil palm leaves and sago hampas have successfully produced high value materials with single step pyrolysis method. The pyrolysis method is based on the templating approach, which originally come from the precursor itself. The natural template found in the precursor of oil palm leaves is silica that has been confirmed by FTIR, XRD and EDX analysis. On the other hand, the lignocellulosic material content in the precursor also plays important role in the fabrication of the carbon nanospheres as a carbon source. This method does not involved catalyst and using low cost precursor.

The obtained materials were characterized using several analyses, which are XRD, FTIR, TGA, BET, Raman, FESEM-EDX and TEM. From the characterizations, the obtained materials are carbon nanospheres where it appeared in nanoscale size with spherical shape and having porous nature. The pyrolysis temperature is different depending on the type of precursor.

.

As for oil palm leaves, the optimum pyrolysis temperature is at 600 °C. At this temperature, it shows high content of carbon that reaches 87 % of atomic percentage and exhibit the smallest particle size which is ~20 nm with uniform particle distribution. Besides that, XRD shows the high crystalline of carbon, which was again confirmed by the Raman analysis. Although the particle is in nano size, the BET results show quite low surface area. This phenomenon happen due to the aggregation of the carbon nanospheres that creates intact and exhibit smooth surfaces thus making low surface area compared to the previous report. The FESEM and TEM images show the nano size and also the spherical shape that is clearly visible.

Sago hampas is pyrolyzed at two different temperature which is 400 °C and 600 °C where it shows CNSs treated at 600 °C giving better performance compared to the CNSs treated at 400 °C. The particle size shows that CNSs exhibit 50-70 nm with regular spherical shape and having high carbon content which is 83.79 %. In addition, it shows that as the pyrolysis temperature increases, the size of obtained CNSs also decreases. Besides that, the micropore ratio of CNSs treated at 600 °C is much higher which is 59.4 %. Furthermore, in the XRD results shows the high graphitic structure appears in the CNSs treated at 600 °C and this values was confirmed by the Raman data.

Among of these two bio waste used, the oil palm leaves was preferable based on the smallest sizes and the higher carbon percentage. But carbon nanospheres obtained from different precursor have their own characteristic that can be applied to various type of applications. The summary of the obtained carbon nanospheres is shown in the Table 5.1.

Carbon nanospheres with these unique properties play important key factors to be used for wide areas of applications especially in biotechnology field. As mentioned in the previous chapter, carbon nanospheres can be used for biotechnology application, which is cell imaging in drug delivery applications. The zeta potential values of the carbon nanospheres are in the range of -20 mV to -30 mV and those values are important key for cell imaging applications. Therefore, the utilization of bio waste is beneficial to reduce and control the amount of bio-waste produced every year. In the same time, using bio waste as a

starting material or precursor is an alternative way to cut the production cost hence can be economical to the consumer.

Table 5.1: Summary of carbon nanospheres results.

Analysis	Bio waste precursor				
	Oil palm leaves (OPL)			Sago hampas (SH)	
	500 °C	600 °C	700 °C	400 °C	600 °C
Particle size (FESEM)	20-40 nm	20 nm	20-22 nm	80-90 nm	60-70 nm
Particle size (TEM)	80 nm	30 nm	40 nm	65 nm	50 nm
Carbon content (EDX)	80.74 %	87.90 %	44.87 %	80.15 %	83.79 %
I_D/I_G ratio (XRD)	0.69	0.73	0.78	0.87	0.84
Micropore ratio (BET)	~47 %	75 %	56.4 %	46 %	59.4 %
Zeta potential	-32 mV	-22.7 mV	-26.8 mV	-32.5 mV	-32.1 mV

5.2   LIMITATIONS OF STUDY

Although this research had achieved its goal, yet few limitations were present. First, a difficulty for sieving method since the sieving shaker is not available. Preparation of raw materials by manual method is tedious and time consuming. Secondly, the available tube furnace is not in a complete set up so the experiment should be monitored continuously and also higher temperature cannot be applied. Furthermore, the available tube furnace is in small size therefore the production of materials has to be done for few times to obtained large quantity. Thirdly, some of the instrument used was not in good conditions producing unsatisfied result. So, some of the analysis needed to be repeated few times.

5.3   FUTURE RECOMMENDATIONS

After completing this research, it has provided few insights that can be used for future works. First of all, the activation of carbon material can be done by using different type of approach either by chemical or physical activation. The activation by using KOH as solvents is commonly used by many researchers to activate the carbon. This activation also depends on many parameters such as mass ratio between the carbon material and KOH, activation temperature and also time. By activating the carbon, it may increase the surface area of the carbon nanospheres hence it can have great potential and suitable materials for many applications such as cell imaging, water treatment and energy storage capacity.

Secondly, more study can be done for temperature behaviour where it is the important steps to achieve graphitization. The temperature used should be varies and increase hence the carbonization effect of the CNSs can be studied depending on the temperature as the main parameters. The behaviour of the CNSs also may differ as the temperature increase and finally it may become graphite. In addition, low cost graphite from bio waste may attract much attention since it has wide application.

Besides that, the product from the investigation of graphitization with respect to different pyrolysis temperature can be applied in the cell imaging studies. In this case, the obtained materials pyrolyzed at different temperatures may affect the cell imaging studies and give different findings since the carbonization effect may change the size, structure and also the porosity of the CNSs. Last but not least, as mentioned earlier, CNSs that have high potential for cell imaging studies as in further work, different type of cell can be used to observe reaction of the cell with the CNSs. Other than that, it can also observe the compatibility and toxicity of CNSs in the cell.

REFERENCES

Abdullah, N. and Sulaiman, F. 2013. The Oil Palm Wastes in Malaysia. *Biomass Now - Sustainable Growth and Use*. (76-100). Dr. Miodrag Darko Matovic (Ed.). ISBN: 978-953-51-1105-4. InTech. doi: 10.5772/55302.

Alexis, F., Pridgen, E., Molnar, L.K. and Farokhzad, O.C. 2008. Factors affecting the clearance and biodistribution of polymeric nanoparticles. *Molecular Pharmaceutics*. **5**(4): 505-515.

Ali, G.A.M., Abdul Manaf, S.A.B., Kumar, A., Chong, K.F. and Hegde, G. 2014. High performance supercapacitor using catalysis free porous carbon nanoparticles. *Journal of Physics D: Applied Physics*. **47**(49): 495307.

Alyamani, A. and Lemine, O. M. 2012. FE-SEM Characterization of Some Nanomaterial. *INTECH Open Access Publisher*.

Anwar, Z., Gulfraz, M. and Irshad, M. 2014. Agro-industrial lignocellulosic biomass a key to unlock the future bio energy: A brief review. *Journal of Radiation Research and Applied Sciences*. **7**: 163-173.

Awg-Adeni, D.S., Abd-Aziz, S., Bujang, K. and Hassan, M.A. 2010. Bioconversion of sago residue into value added products. *African Journal of Biotechnology*. **9**(14): 2016-2021.

Baravkar, A.A., Kale, R.N. and Sawant, S. 2011. Ft-Ir Spectroscopy: Principle, Technique and Mathematics.

Bénard, J., Raguénez, G., Kauffmann, A., Valent, A., Ripoche, H., Joulin, V., ... and Valteau-Couanet, D. 2008. MYCN-non-amplified metastatic neuroblastoma with good prognosis and spontaneous regression: a molecular portrait of stage 4S. *Molecular Oncology*. **2**(3): 261-271.

Bhunia, S. K., Pradhan, N. and Jana, N. R. 2014. Vitamin B1 derived blue and green fluorescent carbon nanoparticles for cell imaging application. *ACS Applied Materials & Interfaces*. **6**(10): 7672−7679.

Blackman, E. 1968. The pattern and sequence of opaline silica deposition in rye (Secale cereale L.). *Annals of Botany*. **32**(1): 207-218.

Bumbrah, G.S. and Sharma, R.M. 2015. Raman spectroscopy–Basic principle, instrumentation and selected applications for the characterization of drugs of abuse. *Egyptian Journal of Forensic Sciences*.

Cançado, L.G., Pimenta, M.A., Neves, R.A., Medeiros- Ribeiro, G., Enoki, T., Kobayashi, Y., Takai, K., Fukui, K., Dresselhaus, M.S., Saito, R. and Jorio, A. 2004. Anisotropy of the Raman spectra of nanographite ribbons. *Physical Review Letters*. **93**(4): 047403.

Caputo, E., Maiorana, L., Vasta, V., Pezzino, F.M., Sunkara, S., Wynne, K., Elia, G., Marincola, F.M., McCubrey, J.A., Libra, M., Travali, S. and Kane, M. 2011. Characterization of human melanoma cell lines and melanocytes by proteome analysis. *Cell Cycle*. **10**(17): 2924-2936.

Chen, G.X., Hong, M.H. and Chong, T.C. 2004. Preparation of carbon nanoparticles with strong optical limiting properties by laser ablation in water. *Journal of Applied Physics*. **95**(3): 1455- 1459.

Chen, J., Li, L., Su, J., Li, B., Chen, T. and Wong, Y.S. 2014. Synergistic Apoptosis-Inducing Effects on A375 Human Melanoma Cells of Natural Borneol and Curcumin. *PloS One*. **9**(6): e101277.

Cheng, C.H., Lehmann, J., Thies, J.E., Burton, S.D. and Engelhard, M.H. 2006. Oxidation of black carbon by biotic and abiotic processes. *Organic Geochemistry*. **37**(11): 1477-1488.

Chodurek, E., Orchel, A., Gawlik, N., Kulczycka, A., Gruchlik, A. and Dzierøewicz, Z. 2010. Proliferation and cellular death of A375 cell line in the presence of HDACs inhibitors. *Acta Poloniae Pharmaceutica*. **67**: 686-689.

Chu, C., Lugovtsev, V., Golding, H., Betenbaugh, M. and Shiloach, J. 2009. Conversion of MDCK cell line to suspension culture by transfecting with human siat7e gene and its application for influenza virus production. *Proceedings of the National Academy of Sciences*. **106**(35): 14802-14807.

Currie, H.A. and Perry, C.C. 2007. Silica in plants: biological, biochemical and chemical studies. *Annals of Botany*. **100**(7): 1383-1389.

Das, S. and Saha, M. 2012. Preparation of carbon nanosphere from bamboo and its use in water purification. *Current Trends in Technology and Sciences*. **2**(1): 174-177.

Dawood, M.O. and Hassan, MAM. 2014. Carbon nanosphere black, soot synthesis by chemical vapor deposition for multi gas sensor. *International Journal of Nanoscience and Nanoengineering*. **1**(1): 1-17.

Dayanandan, P. 1983. Localization of silica and calcium carbonate in plants. *Scanning Electron Microscopy*. **3**: 1519-24.

Dikpati, A., Madgulkar, A.R., Kshirsagar, S.J., Bhalekar, M.R. and Chalal, A.S. 2012. Targeted drug delivery to CNS using nanoparticles. *Journal of Applied Pharmaceutical Science*. **2**(1): 179-191.

Doolaanea, A.A., Mansor, N.I., Nor, N.H.M. and Mohamed, F. 2014. Cellular uptake of *Nigella sativa* oil-PLGA microparticles by PC-12 cell line. *Journal of Microencapsulation*. **31**(6): 600-608.

Egerton, R. 2006. Physical principles of electron microscopy: an introduction to TEM, SEM, and AEM. *Springer Science & Business Media*.

Fagerlund, G. 1973. Determination of specific surface by the BET method. *Matériaux et Construction*. **6**(3): 239-245.

Faix, O. 1992. Fourier transforms infrared spectroscopy. In Methods in lignin chemistry (pp. 83-109). *Springer Berlin Heidelberg.*

Fang, Y., Gu, D., Zou, Y., Wu, Z., Li, F., Che, R., Deng, Y., Tu, B. and Zhao, D. 2010. A low-concentration hydrothermal synthesis of biocompatible ordered mesoporous carbon nanospheres with tunable and uniform size. *Angewandte Chemie International Edition.* **49**: 7987-7991.

Foo, K.Y. and Hameed, B.H. 2010. Insights into the modelling adsorption isotherm system. *Chemical Engineering Journal.* **156**(1): 2-10.

Frackowiak, E. and Beguin, F. 2001. Carbon materials for the electrochemical storage of energy in capacitors. *Carbon.* **39**: 937-950.

Fultz, B. and Howe, J. 2013. Diffraction and the X-ray powder diffractometer. InTransmission Electron Microscopy and Diffractometry of Materials (pp. 1-57). *Springer Berlin Heidelberg.*

Galeener, F.L. 1979. Band limits and the vibrational spectra of tetrahedral glasses. *Physical Review B: Condensed Matter and Material Physics.* **19**(8): 4292.

Galeener, F.L. and Sen, P.N. 1978. Theory for the first order vibrational spectra of disordered solids. *Physical Review B.* **17**(4): 1928.

Gao, L., Lu, N.P., Liao, L.G., Ji, A.L. and Cao, Z.X. 2012. Nanocrystalline Si:H thin films grown at room temperature with plasma-enhanced chemical vapour deposition at a very high pressure. *Journal of Physics D: Applied Physics.* **45**(33): 335104.

Gelb, L. D., & Gubbins, K. E. 1999. Pore size distributions in porous glasses: a computer simulation study. *Langmuir.* **15**(2): 305-308.

Han, F.D., Bai, Y.J., Liu, R., Yao, B., Qi, Y.X., Lun, N. and Zhang, J.X. 2011. Template free synthesis of interconnected hollow carbon nanospheres for high performance anode material in lithium ion batteries. *Advances Energy Materials.* **1**(5): 798-801.

Han, Y., Jung, H.W. and Park, Y.K. 2012. The roots of Atractylodes japonica Koidzumi promote adipogenic differentiation via activation of the insulin signaling pathway in 3T3-L1 cells. *BMC Complementary and Alternative Medicine.* **12**(1): 154.

Hans, M.H. and Lowman, A.M. 2002. Biodegradable nanoparticles for drug delivery and targeting. *Current Opinion in Solid State and Materials Science.* **6**: 319-327.

Hashim, R., Wan Nadhari, W.N.A., Sulaiman, O., Kawamura, F., Hiziroglu, S., Sato, M., Sugimoto, T., Seng, T.G. and Tanaka, R. 2011. Characterization of raw materials and manufactured binderless particleboard from oil palm biomass. *Materials and Design.* **32**(1): 246-254.

Honary, S. and Zahir, F. 2013. Effect of zeta potential on the properties of nano drug delivery systems – a review (part 1). *Tropical Journal of Pharmaceutical Research*. **12**(2): 255-264.

Hooi, K.K., Alauddin, Z.A.Z and Ong, L.K. 2009. Laboratory scale pyrolysis of oil palm pressed fruit fibres. *Journal of Oil Palm Research*. **21** (June): 577-587.

Hossain, M.A. and Islam, S. 2013. Synthesis of carbon nanoparticles from kerosene and their characterization by SEM/EDX, XRD and FTIR. *American Journal of Nanoscience and Nanotechnology*. **1**(2): 52-56.

Im, J.E., Lee, H.N., Li, J. and Kim, R.K. 2014. A novel method for the fabrication of monodispersed carbon nanospheres and their crosslinked forms. *Bulletin of Korean Chemical Society*. **35**(3): 871-874.

Irvine, J.D., Takahashi, L., Lockhart, K., Cheong, J., Tolan, J.W., Selick, H.E. and Grove, J.R. 1999. MDCK (Madin–Darby canine kidney) cells: a tool for membrane permeability screening. *Journal of Pharmaceutical Sciences*. **88**(1): 28-33.

Jones, L.H.P. and Handreck, K.A. 1967. Silica in soils, plants and animals. *Advances in Agronomy*. **19**(1): 107-149.

Joo, J.B., Kim, P., Kim, W., Kim, J., Kim, N.D. and Yi, J. 2008. Simple Preparation of Hollow Carbon Sphere via Templating Method. *Current Appied. Physics*. **8**: 814–817.

Joyner, L.G., Weinberger, E.B. and Montgomery, C.W. 1945. Surface area measurements of activated carbons, silica gel and other adsorbents. *Journal of the American Chemical Society*. **67**(12): 2182-2188.

Kacurakova, M., Capek, P., Sasinkova, V., Wellner, N. and Ebringerova, A. 2000. FT-IR study of plant cell wall model compounds: pectic polysaccharides and hemicelluloses. *Carbohydrate Polymer*. **43**(2): 195-203.

Kim, T.W., Chung, P.W., Slowing, I.I., Tsunoda, M., Yeung, E.S. and Lin, V.S.Y. 2008. Structurally ordered mesoporous carbon nanoparticles as transmembrane delivery vehicle in human cancer cells. *Nano letters*. **8**(11): 3724-3727.

Klemm, D., Heublein, B., Fink, H.P. and Bohn, A. 2005. Cellulose: fascinating biopolymer and sustainable raw material. *Angewandte Chemie International Edition.* **44**(22): 3358–3393.

Knights, J.C., Lucovsky, G. and Nemanich, R.J. 1979. Defects in plasma-deposited a-Si-H. *Journal of Non-Crystalline Solids*. **32**(1): 393-403

Krishnamurthy, G. and Namitha R. 2013. Synthesis of structurally novel carbon micro/nanospheres by low temperature-hydrothermal process. *Journal of the Chilean Chemical Society*. **58**(3): 1930-1933.

Kuga, S., Kim, D.Y., Nishiyama, Y. and Brown, R.M. 2002. Nanofibrillar carbon from native cellulose. *Molecular Crystals and Liquid Crystals.* **387**(1): 13–19.

Kumar, A., Hegde, G., Abdul Manaf, S.A.B., Ngaini, Z. and Sharma, K.V. 2014. Catalyst free silica templated porous carbon nanoparticles from bio-waste materials. *Chemical Communication.* **50**(84): 12702-12705.

Kumar, V., Toffoli, G. and Rizzolio, F. 2013. Fluorescent carbon nanoparticles in medicine for cancer therapy. *ACS Medical Chemistry Letters*. **4**: 1012-1013.

Kuroda, K., Ozawa T. and Ueno T. 2001. Characterization of sago palm (Metroxylon sagu) lignin by analytical pyrolysis. *Journal of Agricultural and Food Chemistry*. **49**(4): 1840-1847.

Lai, L.W. and Idris, A. 2013. Disruption of oil palm trunks and fronds by microwave alkali pretreatment. *BioResources*. **8**(2): 2792-2804.

Lang, F. and Paulmichl, M. 1995. Properties and regulation of ion channels in MDCK cells. *Kidney International*. **48**(4): 1200-1205.

Lee, W.H. and Moon, J.H. 2014. Monodispersed N-doped carbon nanospheres for supercapacitor applications. *ACS Applied Materials & Interfaces*. **6**(16): 13968-13976.

Lespade, P., Al-Jishi, R. and Dresselhaus, M.S. 1982. Model for Raman scattering from incompletely graphitized carbons. *Carbon*. **20**(5): 427-431

Li, G., Guo, C., Sun, C., Ju, Z., Yang, L., Xu, L. and Qian, Y. 2008. A facile approach for the synthesis of uniform hollow carbon nanospheres. *Journal of Physical Chemistry C*. **112**: 1896-1900.

Li, M., Wu, Q., Wen, M. and Shi, J. 2009. A novel route for preparation of hollow carbon nanospheres without introducing templates. *Nanoscale Research Letters*. **4**(11): 1365-1370.

Li, Y., Chen, J., Xu, Q., He, L. and Chen, Z. 2009. Controllable route to solid and hollow monodisperse carbon nanospheres. *The Journal of Physical Chemistry C*. **113**(23): 10085-10089.

Li, Z. H., Wu, D.C., Liang, Y.R., Xu, F. and Fu, R.W. 2013. Facile fabrication of novel highly microporous carbons with superior size-selection adsorption and supercapacitance properties. *Nanoscale.* **5**(22): 10824-10828.

Lin, Y.H., Chi, Y.C. and Lin, G.R. 2013. Nanoscale charcoal powder induced saturable absorption and mode-locking of a low-gain erbium-doped fiber-ring laser. *Laser Physics Letters*. **10**(5): 055105.

Looi, C.Y., Moharram, B., Paydar, M., Wong, Y.L., Leong, K.H., Mohamad, K., ... and Mustafa, M.R. 2013. Induction of apoptosis in melanoma A375 cells by a chloroform fraction of Centratherum anthelminticum (L.) seeds involves NF-kappaB, p53 and Bcl-2-controlled mitochondrial signaling pathways. *BMC Complementary and Alternative Medicine*. **13**(1): 166.

Lou, Z., Huang, H., Li, M., Shang, T. and Chen, C. 2014. Controlled synthesis of carbon nanoparticles in a supercritical carbon disulfide system. *Materials*. **7**(1): 97-105.

Mathew, A.P., Oksman, K. and Sain, M. 2005. Mechanical properties of biodegradable composites from poly lactic acid (PLA) and microcrystalline cellulose (MCC). *Journal of Applied Polymer Science.* **97**(5): 2014-2025.

McMahon, G. 2008. Analytical instrumentation: a guide to laboratory, portable and miniaturized instruments. *John Wiley & Sons.*

Miao, J.Y., Hwang, D.W., Narasimhulu, K.V., Lin, P.I., Chen, Y.T., Lin, S.H. and Hwang, L.P. 2004. Synthesis and properties of carbon nanospheres grown by CVD using Kaolin supported transition metal catalysts. *Carbon.* **42**: 813-822.

Mitani, N. and Ma, J.F. 2005. Uptake system of silicon in different plant species. *Journal of Experimental Botany.* **56**(414): 1255-1261.

Mohammed, M.I., Ibrahim, R. I., Mahmoud, L. H., Zablouk, M. A., Manweel, N. and Mahmoud, A. 2013. Characteristics of carbon nanospheres prepared from locally deoiled asphalt. *Advances in Materials Science and Engineering.* **2013***:*1-5. doi:10.1155/2013/356769.

Mohan, A.N. and Manoj, B. 2012. Synthesis and characterization of carbon nanospheres from hydrocarbon soot. *International Journal of Electrochemical Science*. **7**: 9537-9549.

Mura, S., Hillaireau, H., Nicolas, J., Droumaguet, B.L., Gueutin, C., Zanna, S., Tsapis, N. and Fattal, E. 2011. Influence of surface charge on the potential toxicity of PLGA nanoparticles towards Calu-3 cells. *International Journal of Nanomedicine*. **6**: 2591-2605.

Mustapa K.S.M., Mahmud, S.N., Hussain, S.A. and Ahmadun, F.R. 2007. Improvement on sago flour processing. *International Journal of Engineering and Technology*. **4**(1): 8-14.

Nieto-Marquez, A., Romero, R., Romero, A. and Valverde, J.L. 2011. Carbon nanospheres: synthesis, physicochemical properties and applications. *Journal of Materials Chemistry*. **21**(6): 1664.

Nishiyama, Y., Sugiyama, J., Chanzy, H. and Langan, P. 2003. Crystal Structure and Hydrogen Bonding System in Cellulose Iα from Synchrotron X-ray and Neutron Fiber Diffraction. *Journal of American Chemical. Society.* **125**(47): 14300–14306.

Pan, W.P., Xu, W. and Li, S. 2005. Fundamentals of TGA and SDT. InThermal analysis. Fundamentals and applications to material characterization (pp. 1-7). *Servicio de Publicaciones.*

Peng, F., Ren, J. L., Xu, F., Bian, J. and Sun, R.C. 2009. Comparative study of hemicelluloses obtained by graded ethanol precipitation from sugarcane bagasse. *Journal of Agricultural and Food Chemistry.* **57**(14): 6305-6317.

Perrault, S.D., Walkey, C., Jennings, T., Fischer, H.C. and Chan, W.C. 2009. Mediating tumor targeting efficiency of nanoparticles through design. *Nano Letters.* **9**(5): 1909-1915.

Poinern, G.E.J., Brundavanam, S., Shah, M., Laava, I. and Fawcett, D. 2012. Photothermal response of CVD synthesized carbon (nano) spheres/aqueous nanofluids for potential application in

direct solar absorption collectors: a preliminary investigation. *Nanotechnology, Science and Applications*. **5**: 49-59.

Prychid, C.J., Rudall, P.J. and Gregory, M. 2003. Systematics and biology of silica bodies in monocotyledons. *The Botanical Review*. **69**(4): 377-440.

Pushpamalar, V., Langford, S.J., Ahmad, M. and Lim, Y.Y. 2006. Optimization of reaction conditions for preparing carboxymethyl cellulose from sago waste. *Carbohydrate Polymers*. **64**(2): 312-318.

Qian, H.S., Han, F.M., Zhang, B., Guo, Y.C., Yue, J. and Peng, B.X. 2004. Non-catalytic CVD preparation of carbon spheres with a specific size. *Carbon*. **42**(4): 761-766.

Qian, J., Chen, J., Ruan, S., Shen, S., He, Q., Jiang, X., Zhu, J. and Gao, H. 2014. Preparation and biological evaluation of photoluminescent carbonaceous nanospheres. *Journal of Colloid and Interface Science*. **429**: 77-82.

Ray, S.C., Saha, A., Jana, N.R. and Sarkar, R. 2009. Fluorescent carbon nanoparticles: synthesis, characterization and bioimaging applications. *Journal of Physical Chemistry C*. **113**(43): 18546-18551.

Reimer, L. 2013. Transmission electron microscopy: physics of image formation and microanalysis (Vol. 36). *Springer*.

Roslan, A.M., Zahari, M.A.K.M., Hassan, M.A and Shirai, Y. 2014. Investigation of oil palm frond properties for use as biomaterials and biofuels. *Tropical Agriculture and Development*. **58**(1): 26-29.

Ruan, S., Zhu, B., Zhang, H., Chen, J., Shen, S., Qian, J., He, Q. and Gao, H. 2014. A simple one step method for preparation of fluorescent carbon nanospheres and the potential application in cell organelles imaging. *Journal of Colloid and Interface Science*. **422**: 25-29.

Saceda, J.J.F., de Leon, R.L., Rintramee, K., Prayoonpokarach, S. and Wittayakun, J. 2011. Properties of Silica from Rice Husk and Rice Husk Ash and Their Utilization for Zeolite Y Synthesis. *Quimica Nova*. **34**(8): 1394-1397.

Salman, J.M. 2013. Optimization of preparation conditions for activated carbon from palm oil fronds using response surface methodology on removal pesticides from aqueous solution. *Arabian Journal of Chemistry*. **7**(1): 101-108.

Seitz, C., Frensing, T., Höper, D., Kochs, G. and Reichl, U. 2010. High yields of influenza A virus in Madin–Darby canine kidney cells are promoted by an insufficient interferon-induced antiviral state. *Journal of General Virology*. **91**(7): 1754-1763.

Selvi, B.R., Jagadeesan, D., Suma, B.S., Nagashankar, G., Arif, M., Balasubramanyam, K., Eswaramoorthy, M. and Kundu, T.K. 2008. Intrinsically fluorescent carbon nanospheres as a nuclear targeting vector: delivery of membrane impermeable molecule to modulate gene expression in vivo. *Nano Letters*. **8**(10): 3182-3188.

Selvi, R.B., Chatterjee, S., Jagadeesan, D., Chaturbedy, P., Suma, B.S., Eswaramoorthy, M. and Kundu, T.K. 2012. ATP driven c;athrin dependent entry of carbon nanospheres prefer cells with glucose receptors. *Journal of Nanobiotechnology*. **10**(1): 1-9.

Sengupta, A. and Sarkar, C. K. (Eds.). 2015. Introduction to Nano: Basics to Nanoscience and Nanotechnology. *Springer*.

Sharma, R., Bisen, D.P., Shukla, U. and Sharma, B.G. 2012. X-ray diffraction: a powerful method of characterizing nanomaterials. *Recent Research in Science and Technology*. **4**(8).

Sim, S.F., Mohamed, M., Lu, N.A.L.M.I., Sarman, N. S. P. and Samsudin, S.N.S. 2012. Computer-assisted analysis of fourier transform infrared (FTIR) spectra for characterization of various treated and untreated agriculture biomass. *Bioresources*. **7**(4): 5367-5380.

Sing, K. 2001. The use of nitrogen adsorption for the characterization of porous material. *Colloids and Surfaces A: Physicochemical and Engineering Aspects*. **187**: 3-9.

Sing, K.S. 1998. Adsorption methods for the charactrization of porous materials. *Advances in colloids and interface science.* **76**: 3-11.

Smith, E. and Dent, G. 2013. Modern Raman spectroscopy: a practical approach. *John Wiley & Sons.*

Su, D.M., Zhang, Q., Wang, X., He, P., Zhu, Y.J., Zhao, J., ... and Su, Y.A. 2009. Two types of human malignant melanoma cell lines revealed by expression patterns of mitochondrial and survival-apoptosis genes: implications for malignant melanoma therapy. *Molecular Cancer Therapeutics*. **8**(5): 1292-1304.

Sukiran, M.A., Loh, S.K., Abu Bakar, N. and Choo, Y.M. 2011. Production and characterization of bio-char from the pyrolysis of empty fruit bunches. *American Journal of Applied Sciences.* **8**(10): 984-988.

Tan, X.W., Romainor, A.N.B., Chin, S.F. and Ng, S.M. 2014. Carbon dots production via pyrolysis of sago waste as potential probe for metal ions sensing. *Journal of Analytical and Applied Pyrolysis*. **105**: 157-165.

Tan, Y.H., Davis, J.A., Fujikawa, K., Ganesh, N.V., Demchenko, A.V. and Stine, K.J. 2012. Surface area and pore size characteristics of nanoporous gold subjected to thermal, mechanical, or surface modification studied using gas adsorption isotherms, cyclic voltammetry, thermogravimetric analysis, and scanning electron microscopy. *Journal of Materials Chemistry.* **22**(14): 6733-6745.

Tremblay, R.G., Sikorska, M., Sandhu, J.K., Lanthier, P., Ribecco-Lutkiewicz, M. and Bani-Yaghoub, M. 2010. Differentiation of mouse Neuro 2A cells into dopamine neurons. *Journal of Neuroscience Methods*. **186**(1): 60-67.

Tripathi, S., Sharon, M., Maldar, N.N., Shukla, J. and Sharon, M. 2012. Carbon nano spheres and nano tubes synthesized from castor oil as precursor: for removal of arsenic dissolved in water. *Archives of Applied Science Research.* **4**(4): 1788-1795.

Trogadas, P., Fuller, T.F. and Strasser, P. 2014. Carbon as catalyst and support for electrochemical energy conversion. *Carbon* .**75**: 5-42.

Tuinstra, F. and Koenig, J.L. 1970. Raman spectrum of graphite. *The Journal of Chemical Physics*. **53**(3): 1126-1130.

Vakili, M., Rafatullah, M., Ibrahim, M.H., Salamatinia, B., Gholami, Z. and Zwain, H.M. 2014. A review on composting of oil palm biomass. *Environment, Development and Sustainability*. 1-19. doi: 10.1007/s10668-014-9581-2

Varghese, S., Kuriakose, S. and Jose, S. 2013. Antimicrobial activity of carbon nanoparticles isolated from natural sources against pathogenic gram-negative and gram positive bacteria. *Journal of Nanoscience*. **2013**: 1-5.

Walker, Jr, P.L., Rakszawski, J.F. and Amington, A.F. 1954. Determination of graphitic and amorphous carbon. *Chemistry*. **46**(7): 1620-1624.

Wang, C., Wang, Y., Graser, J., Zhao, R., Gao, F. and O'Connell, M.J. 2013. Solution-based carbohydrate synthesis of individual solid, hollow and porous carbon nanospheres using spray pyrolysis. *ACS Nano*. **7**(12): 11156-11165.

Wang, J.T., Chen, C., Wang, E. and Kawazoe, Y. 2014. A new carbon allotrope with six-fold helical chain in all sp^2 bonding networks. *Scientific Reports*. **4**: 4339.

Wang, Y., Su, F., Wood, C.D., Lee, J.Y and Zhao, X.S. 2008. Preparation and characterization of carbon nanospheres as anode materials in lithium-ion secondary batteries. *Industrial & Engineering Chemistry Research*. **47**(7): 2294-2300.

Wang, Z.L. 2000. Transmission electron microscopy of shape-controlled nanocrystals and their assemblies. *The Journal of Physical Chemistry B*. **104**(6): 1153-1175.

Weinstein, J.L., Katzenstein, H.M. and Cohn, S.L. 2003. Advances in the diagnosis and treatment of neuroblastoma. *The Oncologist*. **8**(3): 278-292.

Wu, Z.Y., Li, C., Liang, H.W., Chen, J.F. and Yu, S.H. 2013. Ultralight, flexible and fire-resistant carbon nanofiber aerogels from bacterial cellulose. *Angewandte Chemie International Edition*. **52**(10): 2925–2929.

Xu, S., Yan, X.B., Wang, X.L., Yang, S.R. and Xue, Q.J. 2010. Synthesis of carbon nanospheres from carbon-based network polymers. *Journal of Materials Science*. **45**(10): 2619-2624.

Xu, X., Zhang, K., Zhao, L., Wang, D., Bu, W., Zheng, C. and Sun, H. 2014. Characteristics of three sizes of silica nanoparticles in the osteoblastic cell line, MC3T3-E1. *RSC Advances*. **4**(87): 46481-46487.

Xu, Z.P., Zeng, Q.H., Lu, G.Q. and Yu, A.B. 2006. Inorganic nanoparticles as carriers for efficient cellular delivery. *Chemical Engineering Science*. **61**: 1027-1040.

Yan, F., Zhang, C., Zheng, Y., Mei, L., Tang, L., Song, C., … and Huang, L. 2010. The effect of poloxamer 188 on nanoparticle morphology, size, cancer cell uptake and cytotoxicity. *Nanomedicine: Nanotechnology, Biology and Medicine*. **6**(1): 170–178.

Yang, H., Yan, R., Chin, T., Liang, D.T., Chen, H. and Zheng, C. 2004. Thermogravimetric analysis- Fourier transforms infrared analysis of palm oil waste pyrolysis. *Energy & Fuels*. **18**(6): 1814-1821.

Yuan, D., Chen, J., Zeng, J. and Tan, S. 2008. Preparation of monodisperse carbon nanospheres for electrochemical capacitors. *Electrochemistry Communications*. **10**(7): 1067-1070.

Yuliansyah, A.T. and Hirajima, T. 2012. Efficacy of Hydrothermal Treatment for Production of Solid Fuel from Oil Palm Wastes. *Resource Management for Sustainable Agriculture*. (pp 4-20). Dr. Vikas Abrol (Ed.). ISBN: 978-953-51-0808-5. InTech. doi: 10.5772/50581.

Zeng, X., Tao, W., Mei, L., Huang, L., Tan, C. and Feng, S.S. 2013. Cholic acid-functionalized nanoparticles of star-shaped PLGA-vitamin E TPGS copolymer for docetaxel delivery to cervical cancer. *Biomaterials*. **34**(25): 6058-6067.

Zeta potential analysis of nanoparticles guidelines. *NanoComposix*. September 2012, v 1.1.

Zhang, C., Hatzell, K.B., Boota, M., Dyatkin, B., Beidaghi, M., Long, D., Qiao, W., Kumbur, E.C. and Gogotsi, Y. 2014. Highly porous carbon spheres for electrochemical capacitors and capacitive flowable suspension electrodes. *Carbon*. **77**: 155-164.

Zhang, Y., Yang, M., Park, J.H., Singelyn, J., Ma, H., Sailor, M.J., Ruoslahti, E., Ozkan, M. and Ozkan, C. 2009. A surface-charge study on cellular-uptake behavior of F3-peptide-conjugated iron oxide nanoparticles. *Small*. **5**(17): 1990-1996.

Zhang, Y., Yang, M., Portney, N.G., Cui, D., Budak, G., Ozbay, E., Ozkan, M. and Ozkan, C.S. 2008. Zeta potential: a surface electrical characteristic to probe the interaction of nanoparticles with normal and cancer human breast epithelial cells. *Biomed Microdevices*. **10**: 321-328.

ACHIEVEMENTS

1. **PUBLICATIONS**

(a) **Included in this thesis**

1. Gurumurthy Hegde, Shoriya Aruni Abdul Manaf, Anuj Kumar, KV Sharma, Zainab Ngaini. (2014). Catalysts free silica template porous carbon nanoparticles from bio waste materials. Chem Comm. 50(84), 12702-12705. (IMPACT FACTOR: 6.718)

2. Shoriya Aruni Abdul Manaf, Zainab Ngaini, K.V. Sharma, Partha Roy, Yusuke Yamauchi and Gurumurthy Hegde. (2014). Catalyst free green synthesis of carbon nanospheres for potential biomedical applications: waste to wealth approach. RSC Advances. 5(31), 24528-24533. (IMPACT FACTOR: 3.708)

(b) **Not included in this thesis**

1. Gurumurthy Hegde and Shoriya Aruni Abdul Manaf. (2014).Synthesis and characterization of composite nanomaterials for photonic application, ELSEVIER Proceedings, ICPVS-2014, 271-274.

2. Gomaa AM Ali, Shoriya Aruni Abdul Manaf, Anuj Kumar, Kwok Feng Chong, Gurumurthy Hegde. (2014). High performance supercapacitor using catalysis free porous carbon nanoparticles. Journal of Physics: Applied Physics D. 47(49), 495307. (IMPACT FACTOR: 2.521)

3. Shoriya Aruni Abdul Manaf, Gomaa A.M. Ali, Anuj Kumar, Kwok Feng Chong, K.V. Sharma, Zainab Ngaini, Partha Roy and Gurumurthy Hegde. (2014) High quality catalyst free carbon nanospheres from bio waste sago bark: synthesis, characterization and super capacitor applications: waste to wealth approach. (Submitted to Materials Science and Engineering B, 2015)

4. Shoriya Aruni Abdul Manaf, Anuj Kumar and Gurumurthy Hegde. (2014). Synthesis, characterizations and applications of carbon nanospheres from bio waste: Green technology approach. (Submitted to Carbon)

2.   **PATENTS**

1. Preparation method of low cost carbon nanospheres from oil palm materials (PI 2014701113)
2. A process for producing carbon nanospheres. (UI 2014702858).

3.   **AWARDS AND MEDALS**

1. **Gold Medal, Best Award and Green Technology Awards**, Malaysian Technology Expo **(MTE)** 2014, Putra World Trade Centre (PWTC), Kuala Lumpur.
2. **Gold Medal**, Creation, Innovation, Technology and Research Exposition **(CITREX)** 2014, Universiti Malaysia Pahang, Kuantan.
3. **Gold Medal**, Innovation and Invention Competition through Exhibition **(Icompex)** 2014, POLIMAS, Kedah.
4. **Gold Medal**. International Invention, Innovation and Technology Exhibition **(ITEX)** 2014, Kuala Lumpur Convention Centre (KLCC).
5. **Gold Medal,** Best Invention Award. International Product Exhibition **(INPEX)** 2014, Pittsburgh, USA.

4.   **CONFERENCES**

Poster presentation at Regional Conference Solid State Science Technology (**RCSSST**) 2014, on Conversion of bio waste into composite nanomaterials for photonic applications.